Drell-Yan transverse-momentum spectra at N³LL′ and approximate N⁴LL with SCETlib

Georgios Billis [iD],[a] **Johannes K.L. Michel** [iD][b,c,d] **and Frank J. Tackmann** [iD][e]

[a]*Università degli Studi di Milano-Bicocca & INFN,*
 Piazza della Scienza 3, Milano 20126, Italy

[b]*Center for Theoretical Physics, Massachusetts Institute of Technology,*
 77 Massachusetts Ave, 6-307, Cambridge, MA 02139, U.S.A.

[c]*Institute for Theoretical Physics Amsterdam and Delta Institute for Theoretical Physics,*
 University of Amsterdam,
 Science Park 904, 1098 XH Amsterdam, The Netherlands

[d]*Nikhef, Theory Group,*
 Science Park 105, 1098 XG, Amsterdam, The Netherlands

[e]*Deutsches Elektronen-Synchrotron DESY,*
 Notkestr. 85, 22607 Hamburg, Germany

 E-mail: georgios.billis@unimib.it, jklmich@mit.edu,
 frank.tackmann@desy.de

ABSTRACT: We provide state-of-the-art precision QCD predictions for the fiducial W and Z boson transverse momentum spectra at the LHC at N³LL′ and approximate N⁴LL in resummed perturbation theory, matched to available $\mathcal{O}(\alpha_s^3)$ fixed-order results. Our predictions consistently combine all information from across the spectrum in a unified way, ranging from the nonperturbative region of small transverse momenta to the fixed-order tail, with an emphasis on estimating the magnitude of residual perturbative uncertainties, and in particular of those related to the matching. Parametric uncertainties related to the strong coupling, the collinear PDFs, and the nonperturbative transverse momentum-dependent (TMD) dynamics are studied in detail. To assess the latter, we explicitly demonstrate how the full complexity of flavor and Bjorken x-dependent TMD dynamics can be captured by a single, effective nonperturbative function for the resonant production of any given vector boson at a given collider. We point out that the cumulative p_T^Z cross section at the level of precision enabled by our predictions provides strong constraining power for PDF determinations at full N³LO.

KEYWORDS: Effective Field Theories of QCD, Higher-Order Perturbative Calculations, Resummation

Contents

1 Introduction

The transverse momentum spectra of electroweak bosons produced in hadronic collisions are flagship observables of the LHC precision program, and have been measured to astonishing accuracy by the ATLAS [1–6], CMS [7–11], and LHCb collaborations [12, 13]. The p_T spectrum of the Z boson, measured in the experimentally pristine Drell-Yan dilepton channel, is of particular importance as an irreducible background to many searches for physics beyond the Standard Model, see e.g. ref. [14], and likewise features great sensitivity to key Standard Model parameters like the strong coupling [15, 16]. On the other hand, the p_T spectrum of the W boson, while much harder to access experimentally, is a critical input to measurements of the W boson mass [17–21] that rely on Jacobian peaks — smeared out by the p_T^W spectrum

— to achieve sensitivity. Lastly, recent progress in understanding the complex interplay of fiducial experimental selection cuts and QCD perturbation theory has revealed that even seemingly inclusive quantities like (fiducial) rapidity spectra can feature sensitivity to small-p_T physics, requiring a precise understanding of the underlying p_T spectrum as well [22–26]. In turn, a thorough understanding of these percent-level effects on fiducial rapidity spectra is required e.g. to deliver constraining power on collinear parton distribution functions (PDFs), whose determination has advanced to approximate N^3LO accuracy [27–31].

The phenomenological importance of the p_T^Z and p_T^W spectra has motivated a large-scale effort by the theory community to provide precision predictions for them, in turn making them crucial tests of our understanding of QCD and the electroweak sector of the Standard Model. Fixed-order predictions in QCD perturbation theory at finite $p_T^{Z,W}$ have reached an impressive $\mathcal{O}(\alpha_s^3)$ accuracy [32–40], i.e., $NNLO_1$ relative to the tree-level LO_1 process where one hard parton is radiated into the final state. On the other hand, at small transverse momenta $p_T^V \ll m_V$, where the vector boson V recoils against soft and collinear radiation, the infrared singularities of gauge theory enhance the contribution to the cross section at each perturbative order by large double logarithms $\alpha_s^n \ln^{2n}(p_T^V/m_V)$, upsetting the convergence and validity of the fixed-order series. The all-order resummation of these dominant singular terms, which is based on factorization theorems and the renormalization group, has in the meantime been achieved at N^3LL' [15, 23, 41–43] and approximate N^4LL order [40, 44–46] by several groups. The analytic resummation at this order also provides an important ingredient to extend the combination of high-order calculations with parton showers to N^3LO+PS using the methods of refs. [47, 48]. (Another ingredient is the $NNLL'$ or N^3LL resummation for the $V + 1$ jet process [49].) The region of even smaller transverse momenta $p_T^V \lesssim \Lambda_{QCD}$ close to the QCD confinement scale is of particular interest because it provides access to the nonperturbative transverse momentum-dependent (TMD) dynamics of partons within the proton, see e.g. refs. [45, 50, 51]. Beyond (non)perturbative QCD, mixed strong and weak or electromagnetic corrections have been studied both at fixed order [52–58] and to all orders in the limit of small transverse momentum [59–62].

In this paper, we present predictions for the resummed and matched $q_T \equiv p_T^{W,Z}$ spectrum as implemented in SCETlib [63], a C++ library for numerical calculations in QCD and Soft-Collinear effective theory (SCET). Our emphasis lies on consistently combining all information from across the spectrum, ranging from nonperturbative to fixed-order scales, where we in particular go beyond the status of the literature by including a thorough assessment of the associated matching uncertainties. This is part of an overall, careful estimate of the magnitude of residual perturbative uncertainties, which we supplement with detailed studies of the parametric strong coupling, PDF, and nonperturbative TMD uncertainties. We further present a novel way of rigorously defining effective nonperturbative TMD functions for resonant p_T^V and multi-differential spectra, which has served as an important ingredient of the theoretical model underlying the recent CMS measurement of the W boson mass [21]. As another application of our predictions, we consider the possibility of constraining collinear PDFs at complete three-loop accuracy using the cumulative p_T^Z distribution.

The paper is structured as follows: in section 2, we review the factorization theorem underlying the resummation, give an overview of the perturbative ingredients entering

our predictions, and introduce our matching formalism that unifies the nonperturbative limit, the perturbative resummation, and the fixed-order tail. In section 3, we review the nonperturbative structure of the factorization theorem, and develop our framework of effective nonperturbative functions. In section 4 we present our predictions for the p_T^Z spectrum, discussing the perturbative uncertainty, the impact of nonperturbative physics the parametric α_s, and the parametric PDF uncertainties in turn, before showcasing the impact of approximate N³LO PDFs and N⁴LL Sudakov ingredients on the predicted p_T^Z spectrum. In section 5, we discuss the cumulative fiducial cross section and its sensitivity to PDFs as an immediate application. In section 6, we present our results for the p_T^W spectrum. We conclude and summarize our results in section 7.

2 Factorization, perturbative ingredients, and matching

2.1 Review of factorization

We consider the production of a dilepton pair through Z/γ^* or of a lepton-neutrino final state through a W boson at the LHC. At leading order in the electromagnetic interaction, the fiducial cross section differential in the total transverse momentum q_T of the respective vector boson, $q_T = p_T^Z = p_T^{\ell\ell}$ or $q_T = p_T^W = p_T^{\ell\nu}$, is given by [22]

$$\frac{1}{\pi q_T}\frac{\mathrm{d}\sigma(\Theta)}{\mathrm{d}q_T} = \frac{1}{4E_{\mathrm{cm}}^2}\int \mathrm{d}Q^2\,\mathrm{d}Y \sum_{i=-1}^{7}\sum_{V,V'} L_{i\,VV'}(q,\Theta)\,W_{i\,VV'}(q,P_a,P_b)\,, \qquad (2.1)$$

where q is the momentum carried by the (generally off-shell) vector boson with invariant mass $Q^2 \equiv q^2$ and rapidity Y. Here we have decomposed the hadronic tensor into nine scalar hadronic structure functions $W_{i\,VV'}(q,P_a,P_b)$, with $i = -1,0,\ldots,7$, and summed over the possible vector bosons V,V' interfering with each other. The $W_{i\,VV'}$ encode the hadronic production dynamics. They depend on the vector boson momentum q^μ and the incoming proton momenta $P_{a,b}$, and can be interpreted as entries in the 3×3 spin density matrix for the polarization of the vector boson. By contrast, the leptonic tensor projections $L_{i\,VV'}(q,\Theta)$ that describe the propagation and decay of the vector boson only depend on the intermediate momentum q and the set of fiducial acceptance cuts applied on the dilepton or lepton-neutrino final state, which we collectively denote by Θ. Explicitly, the leptonic tensor projections are given by

$$L_{i\,VV'}(q,\Theta) = \frac{3}{16\pi}\int_{-1}^{1}\mathrm{d}\cos\theta\int_0^{2\pi}\mathrm{d}\varphi\,\hat{\Theta}(q,\theta,\varphi)\,L_{\pm(i)\,VV'}(q,\theta,\varphi)\,g_i(\theta,\varphi)\,, \qquad (2.2)$$

where $\cos\theta$ and φ are spherical coordinates parametrizing the momentum of the matter particle (i.e., the negatively charged lepton, or the neutrino) in a suitable vector boson rest frame, which we take to be the Collins-Soper frame [64]. The prefactors $L_{\pm(i)\,VV'}$ contain the vector-boson propagator and leptonic couplings and depend on whether the hadronic structure function is parity even, $\pm(i) = +$ for $i = -1,0,1,2,5,6$, or parity-odd, $\pm(i) = -$ for $i = 3,4,7$. It is convenient to also define the so-called helicity cross sections

$$\frac{\mathrm{d}\sigma_i}{\mathrm{d}^4q} \equiv \frac{1}{2E_{\mathrm{cm}}^2}\sum_{V,V'} L_{\pm(i)\,VV'}(q^2)\,W_{i\,VV'}(q,P_a,P_b) \qquad (2.3)$$

– 3 –

multiplying the spherical harmonics g_i at the level of the six-fold differential cross section

$$\frac{\mathrm{d}\sigma}{\mathrm{d}^4 q\,\mathrm{d}\cos\theta\,\mathrm{d}\phi} = \frac{3}{16\pi}\sum_i \frac{\mathrm{d}\sigma_i}{\mathrm{d}^4 q}\,g_i(\theta,\varphi)\,. \tag{2.4}$$

Only the parity-even structure functions contribute to the p_T^Z spectrum as long as fiducial cuts are applied independent of lepton charges, while all structure functions in general contribute to the p_T^W spectrum due to the cuts generically being asymmetric under $\ell \leftrightarrow \nu$. The $g_i(\theta,\varphi)$ are real spherical harmonics that describe the distribution of decay products for a given intermediate polarization state. Finally, $\hat{\Theta}(q,\theta,\varphi)$ encodes the action of the fiducial cuts on a dilepton phase-space point parametrized by the two rest-frame angles θ and φ, and an additional total boost by q from the lab frame.[1] One notable special case is $\hat{\Theta} = 1$, which corresponds to the inclusive q_T spectrum proportional to the linear combination $W_{\mathrm{incl}} \equiv W_{-1} + W_0/2$, where $g_{-1,0} = 1 \pm \cos^2\theta$. Another important special case is $\hat{\Theta} = \mathrm{sgn}(Y)\big[\Theta(\cos\theta) - \Theta(-\cos\theta)\big]$, which projects out $g_4 = \cos\theta$, i.e., the forward-backward asymmetry $A_{\mathrm{FB}}(q) \propto \mathrm{sgn}(Y)\,W_4/W_{\mathrm{incl}}$ differential in the vector boson kinematics (but applying no additional fiducial cuts). We stress that while it is convenient to parametrize the decay kinematics in a definite frame, the corresponding projectors acting on the hadronic tensor can in fact be defined in a fully covariant way [22], such that the $W_{i\,VV'}$ are genuine Lorentz scalars.

We are interested in the region of small transverse momentum, $q_T \ll Q$. In this limit, the hadronic structure functions corresponding to the inclusive q_T spectrum and the q_T-dependent forward-backward asymmetry satisfy the following factorization theorem [65–76], which is valid for $i = -1$ and $i = 4$,

$$\begin{aligned}
W_{iVV'} &= W_{iVV'}^{\mathrm{LP}}(q, P_a, P_b)\left[1 + \mathcal{O}\left(\frac{q_T^2}{Q^2}, \frac{\Lambda_{\mathrm{QCD}}^2}{Q^2}\right)\right] \\
&= \sum_{a,b} H_{iVV'\,ab}(Q^2,\mu)\,[B_a B_b S](Q^2, x_a, x_b, \vec{q}_T, \mu)\left[1 + \mathcal{O}\left(\frac{q_T^2}{Q^2}, \frac{\Lambda_{\mathrm{QCD}}^2}{Q^2}\right)\right],
\end{aligned} \tag{2.5}$$

where $x_{a,b} \equiv Q/E_{\mathrm{cm}}\,e^{\pm Y}$. As indicated, the factorization receives power corrections in $(q_T/Q)^2$ and $(\Lambda_{\mathrm{QCD}}/Q)^2$, but remains valid in the nonperturbative regime $q_T \sim \Lambda_{\mathrm{QCD}}$. We will exploit this in section 3 by explicitly parametrizing the leading nonperturbative corrections $\mathcal{O}(\Lambda_{\mathrm{QCD}}^2/q_T^2)$ at small q_T in a way consistent with the field-theoretic structure of the factorization theorem, and by capturing yet higher corrections through model functions.

In ref. [22], it was shown that all linear power corrections $\mathcal{O}(q_T/Q)$ to the fiducial q_T spectrum can be predicted from factorization and resummed to all orders by retaining the exact dependence of the leptonic tensor projections $L_i(q,\Theta)$ on q_T, which naively would

---

[1]Note that this specifies the vector boson rest frame only up to Wigner rotations. The Collins-Soper frame specifically is defined by first performing a longitudinal boost along the beam axis into the frame where the vector boson has vanishing rapidity, followed by a transverse boost by q_T. In the limit of massless protons (and only in this limit [22]), this definition is equivalent to demanding that the incoming protons lie in the plane spanned by the x and z axis of the rest frame, and that they have equal and opposite angles to the z axis.

be power suppressed,

$$\frac{1}{\pi q_T}\frac{\mathrm{d}\sigma(\Theta)}{\mathrm{d}q_T} = \frac{1}{2E_{\mathrm{cm}}^2}\int \mathrm{d}Q^2\,\mathrm{d}Y\sum_{i=-1,4}\sum_{V,V'}L_{iVV'}(q,\Theta)\,W_{iVV'}^{\mathrm{LP}}(q,P_a,P_b)$$
$$\times\left[1+\mathcal{O}\left(\frac{q_T^2}{Q^2},\frac{\Lambda_{\mathrm{QCD}}^2}{Q^2}\right)+\mathcal{O}\left(\frac{\Lambda_{\mathrm{QCD}}^2}{q_T Q}\right)_{\mathrm{DBM}}\right],\tag{2.6}$$

where the $W_{iVV'}^{\mathrm{LP}}$ for $i=-1,4$ are given in eq. (2.5). As discussed in ref. [22], this in fact holds for a broader class of observables that are azimuthally symmetric at leading power, and also generalizes to so-called leptonic power corrections that arise for leptonic observables sensitive to the edge of Born phase space.

The first set of power corrections in eq. (2.6) arises from the quadratic power corrections to the $i=-1,4$ structure functions, whose leptonic coefficient functions scale as $L_{-1,4VV'}\sim(q_T/Q)^0$, as well as from the hadronic structure functions for $i=0,1,3,5,6,7$ that start at most at linear order in q_T/Q, but whose leptonic coefficients are all in addition suppressed by (q_T/Q). The second set of power corrections, indicated by the subscript "DBM" for Double Boer-Mulders effect, arises from the two structure functions $W_{2,5VV'}$. These have a linearly suppressed leptonic coefficient $L_{2,5VV'}\sim q_T/Q$, but only receive a contribution at leading power in q_T/Q from the product of two Boer-Mulders functions, which in turn are suppressed by one power of $\Lambda_{\mathrm{QCD}}/q_T$ each in the case of massless $n_f=5$ QCD [77], and by at least two powers of α_s each for massive quarks [78]. The region where both expansion parameters $\Lambda_{\mathrm{QCD}}/q_T$ and q_T/Q are not small is negligible for resonant Z or W production at the LHC, and we therefore ignore this contribution.[2]

We now return to the individual ingredients in eq. (2.5). Here $H_{iVV'ab}$ denotes the hard function, which encodes virtual corrections to the production amplitudes $ab\to V,V'$ in the underlying hard interaction. The $\overline{\mathrm{MS}}$ result for $H_{iVV'ab}$ can, for instance, be obtained as the IR-finite part of the corresponding quark form factors squared, using dimensional regularization to regulate IR divergences. Explicit expressions for the leptonic prefactors $L_{\pm VV'}$ and the hard functions in terms of IR-finite parts of quark form factors (i.e., SCET Wilson coefficients) can be found in the appendices of ref. [22]. At our working order in this paper, we require the complete three-loop results for the hard function. This involves the three-loop results for the quark nonsinglet form factor [79, 80]. In addition, starting at two loops, there are contributions to the quark singlet axial and vector form factors from closed fermion loops [81–85], which we discuss in more detail in section 2.3.

---

[2]This is further supported by the observation in section 4.2 that the dominant estimated nonperturbative contribution arises from the Collins-Soper (or rapidity) evolution, which is common to both $i=-1,4$ and $i=2,5$. See also footnote 12 for the case of leptonic observables directly sensitive to low scales, such as ϕ_η^* or the p_T^ℓ spectrum near the Jacobian peak.

The second term in eq. (2.5) encodes physics at the low scale $\mu \sim q_T$, and can be written in two prototypical forms,

$$
\begin{aligned}
&[B_a B_b S](Q^2, x_a, x_b, \vec{q}_T, \mu) \\
&\equiv \frac{1}{2\pi} \int_0^\infty \mathrm{d}b_T \, b_T \, J_0(b_T q_T) \, \tilde{B}_a(x_a, b_T, \mu, \nu/\omega_a) \, \tilde{B}_b(x_b, b_T, \mu, \nu/\omega_b) \, \tilde{S}(b_T, \mu, \nu) \quad (2.7\text{a}) \\
&= \frac{1}{2\pi} \int_0^\infty \mathrm{d}b_T \, b_T \, J_0(b_T q_T) \, \tilde{f}_a(x_a, b_T, \mu, Q^2) \, \tilde{f}_b(x_b, b_T, \mu, Q^2) \,. \quad (2.7\text{b})
\end{aligned}
$$

In eq. (2.7a), the beam functions $B_i(x, \vec{k}_T, \mu, \nu/\omega)$ describe the extraction of an unpolarized parton i with longitudinal momentum fraction x and transverse momentum $\vec{k}_T$ from an unpolarized proton, where we have taken a Fourier transform from momentum ($\vec{k}_T$) to position ($\vec{b}_T$) space. Similarly, the soft function $S(\vec{k}_T, \mu, \nu)$ encodes wide-angle soft radiation with total transverse momentum $\vec{k}_T$, which is again Fourier conjugate to $\vec{b}_T$. Evaluating the two beam functions and the soft function at a common argument $\vec{b}_T$ and taking the inverse Fourier transform as above implements momentum conservation in position space. We have also used the fact that the quark beam and soft functions (TMD PDFs) only depend on the magnitude of $\vec{b}_T$ to freely integrate the Fourier phase $e^{\mathrm{i}\vec{b}_T \cdot \vec{q}_T}$ over the azimuth of $\vec{b}_T$ in eq. (2.7), yielding a zeroth-order Bessel function $J_0(b_T q_T)$ of the first kind.

Equivalently, one can write this as shown in eq. (2.7b), where the transverse-momentum dependent beam and soft functions have been combined into transverse-momentum dependent PDFs (TMD PDFs)

$$
\tilde{f}_i(x, b_T, \mu, \zeta) = \tilde{B}_i\left(x, b_T, \mu, \frac{\nu}{\sqrt{\zeta}}\right) \sqrt{\tilde{S}(b_T, \mu, \nu)} \,. \quad (2.8)
$$

A key feature of transverse-momentum dependent factorization is the explicit dependence of the low-energy matrix elements on the energy of the colliding parton, encoded either in its lightcone momentum ω or in the Collins-Soper scale ζ, where

$$
x_{a,b} = \frac{\omega_{a,b}}{E_{\mathrm{cm}}} e^{\pm Y} \,, \qquad \omega_{a,b} = Q \,, \qquad \zeta_{a,b} \propto \omega_{a,b}^2 \,, \qquad (\omega_a \omega_b)^2 = \zeta_a \zeta_b = Q^4 \,, \quad (2.9)
$$

and E_{cm} is the total hadronic center-of-mass energy. This explicit energy dependence sets the TMD PDF apart from the usual collinear PDFs, which only depend on the momentum fraction x, and is a remnant of so-called rapidity divergences [65, 73–75, 86–88]. Regulating and renormalizing them separately in the individual beam and soft functions in eq. (2.7a) introduces an additional scale ν, which is analogous to the $\overline{\mathrm{MS}}$ scale μ from renormalizing UV divergences. The dependence on ν (or equivalently, the rapidity divergences in the bare objects) cancels between the beam and soft function in the TMD PDF, leaving behind the explicit dependence on ω (or ζ). Since both ways of writing eq. (2.7) are frequently encountered in the literature, we will continue to present e.g. the construction of our central profile scale functions in both notations for the benefit of the reader.

The beam and soft functions (and thus the TMD PDFs) are defined as proton and vacuum matrix elements of renormalized operators without making reference to perturbation theory, and thus allow for a rigorous field-theoretic treatment of the $\vec{q}_T$ spectrum in the nonperturbative regime $q_T \sim \Lambda_{\mathrm{QCD}}$. For perturbative $|\vec{k}_T| \sim 1/b_T \gg \Lambda_{\mathrm{QCD}}$, they can

be matched onto collinear PDFs and soft vacuum condensates by performing an operator product expansion [67, 89],

$$\tilde{B}_i\left(x, b_T, \mu, \frac{\nu}{\omega}\right) = \sum_j \int \frac{\mathrm{d}z}{z} \tilde{\mathcal{I}}_{ij}\left(z, b_T, \mu, \frac{\nu}{\omega}\right) f_j\left(\frac{x}{z}, \mu\right) + \mathcal{O}(\Lambda_{\mathrm{QCD}}^2 b_T^2),$$

$$\tilde{S}(b_T, \mu, \nu) = \tilde{S}_{\mathrm{pert}}(b_T, \mu, \nu) + \mathcal{O}\left(\Lambda_{\mathrm{QCD}}^2 b_T^2\right),$$

$$\tilde{f}_i(x, b_T, \mu, \zeta) = \sum_j \int \frac{\mathrm{d}z}{z} \tilde{C}_{ij}(z, b_T, \mu, \zeta)\, f_j\left(\frac{x}{z}, \mu\right) + \mathcal{O}(\Lambda_{\mathrm{QCD}}^2 b_T^2), \qquad (2.10)$$

where the perturbatively calculable matching coefficients are related by

$$\tilde{C}_{ij}(z, b_T, \mu, \zeta) = \tilde{\mathcal{I}}_{ij}\left(z, b_T, \mu, \frac{\nu}{\sqrt{\zeta}}\right) \sqrt{\tilde{S}_{\mathrm{pert}}(b_T, \mu, \nu)}. \qquad (2.11)$$

The perturbative soft, beam functions and TMD PDF matching coefficients are all known to three loops [90–96, 96–100], as required at our perturbative working order in this paper. Our treatment of the nonperturbative corrections to eq. (2.10) is described in section 3.

In practice, we find it important to be able to evaluate the PDFs in eq. (2.10) at a scale that is potentially different from (but still parametrically similar to) the overall scale of the beam function or TMD PDF. In this case we have

$$\tilde{B}_i(x, b_T, \mu, \nu/\omega) = \sum_j \int \frac{\mathrm{d}z}{z} \tilde{\mathcal{I}}_{ij}\left(z, b_T, \mu, \frac{\mu_f}{\mu}, \frac{\nu}{\omega}\right) f_j\left(\frac{x}{z}, \mu_f\right) + \mathcal{O}(\Lambda_{\mathrm{QCD}}^2 b_T^2), \qquad (2.12)$$

where we analytically evaluate the Mellin convolution

$$\tilde{\mathcal{I}}_{ij}\left(z, b_T, \mu, \frac{\mu_f}{\mu}, \frac{\nu}{\omega}\right) \equiv \sum_k \int \frac{\mathrm{d}z'}{z'} \tilde{\mathcal{I}}_{ik}\left(\frac{z}{z'}, b_T, \mu, \frac{\nu}{\omega}\right) U_{kj}\left(z', \mu, \frac{\mu_f}{\mu}\right), \qquad (2.13)$$

consistently reexpanding and truncating in $\alpha_s(\mu)$, and $U_{kj}(z', \mu, \mu_f/\mu)$ is the DGLAP evolution operator that evolves the PDF from μ_f to μ, likewise expanded in terms of powers of $\alpha_s(\mu)$.

2.2 Renormalization group evolution

For observables like q_T that are sensitive to soft and collinear radiation, higher-order perturbative corrections induce double-logarithmic terms $\alpha_s^n \ln^m q_T/Q$, $m \le 2n$ in the hadronic structure functions $W_{i\,VV'}$. In the singular limit, $q_T \to 0$, these logarithms grow arbitrarily large and invalidate its perturbative convergence. The factorization theorem in eq. (2.7a), effectively splits these logarithms according to their dominant contribution from the respective physical modes, resulting in single-scale functions. By solving the renormalization group equations (RGEs), each function is evaluated at its intrinsic (canonical) μ or ν scale and evolved to a common overall μ and ν, resumming the logarithically enhanced terms to all orders in perturbation theory. A standard way to obtain the solutions of the RGEs is to make use of the b_T-space form of the cross section in eq. (2.7a), where the RGEs assume a simple multiplicative form and the boundary scales that eliminate all large logarithms have the canonical scaling

$$\mu_B^{\mathrm{can}} = \mu_S^{\mathrm{can}} = \nu_S^{\mathrm{can}} = \mu_0^{\mathrm{can}} = \mu_f^{\mathrm{can}} = \frac{b_0}{b_T}, \qquad \nu_B^{\mathrm{can}} = \mu_H^{\mathrm{can}} = Q, \qquad (2.14)$$

where μ_0 is the scale at which the boundary condition of the resummed rapidity anomalous dimension or Collins-Soper kernel is evaluated (see below), and the factor of $b_0 = 2e^{-\gamma_E} \approx 1.12292$ is conventional. In practice, this amounts to setting the scales in position space, performing the evolution, and finally transforming back to (momentum) q_T-space by numerically integrating over b_T. An exactly equivalent way of obtaining the same resummed result is by setting the boundary scales for the TMD PDFs in eq. (2.7b) as

$$\mu_0^{\rm can} = \mu_{\rm init}^{\rm can} = \mu_f^{\rm can} = \sqrt{\zeta_{\rm init}^{\rm can}} = \frac{b_0}{b_T}\,, \qquad (2.15)$$

and evolve them to the overall $\mu_{\rm final} = \sqrt{\zeta_{\rm final}} = Q$. This approach bypasses unphysical singularities [101] that arise when naively setting scales or counting logarithms in momentum space, although approaches to momentum-space resummation exist [102, 103]; the formal momentum-space RG solutions of ref. [103] are equivalent to the b_T-space approach up to differences in the fixed-order boundary conditions. Recently, similar unphysical singularities were pointed out for the first time in the resummation of an observable not involving transverse momentum [104] (the heavy-jet mass distribution near the Sudakov shoulder), and a successful resolution using position-space scale setting was demonstrated in ref. [105].

To implement the resummation of rapidity logarithms in the individual beam and soft functions in eq. (2.7a), we employ the exponential regulator [76] together with the rapidity renormalization group framework [75]. In b_T space, the quark beam and soft functions satisfy the virtuality RGEs,

$$\mu\frac{\mathrm{d}}{\mathrm{d}\mu}\ln\tilde{B}_q(x,b_T,\mu,\nu/\omega) = \tilde{\gamma}_B^q(\mu,\nu/\omega) = 2\Gamma_{\rm cusp}^q[\alpha_s(\mu)]\ln\frac{\nu}{\omega} + \tilde{\gamma}_B^q[\alpha_s(\mu)]\,,$$

$$\mu\frac{\mathrm{d}}{\mathrm{d}\mu}\ln\tilde{S}_q(b_T,\mu,\nu) = \tilde{\gamma}_S^q(\mu,\nu) = 4\Gamma_{\rm cusp}^q[\alpha_s(\mu)]\ln\frac{\mu}{\nu} + \tilde{\gamma}_S^q[\alpha_s(\mu)]\,. \qquad (2.16)$$

Here the cusp anomalous dimension $\Gamma_{\rm cusp}^q[\alpha_s(\mu)]$ is in the fundamental representation. Its coefficients are known analytically to four loops [106–115] (see ref. [113] for a complete list of earlier references), which are necessary for the N^{3}LL and N^{3}LL$'$ Sudakov evolution together with the four-loop QCD beta function [116–119]. At N^{4}LL, we in addition require the five-loop beta [120] and cusp coefficient, where the latter is currently known only approximately [121]. The soft noncusp anomalous dimension $\tilde{\gamma}_S^q[\alpha_s(\mu)]$ in the exponential regulator scheme is directly related to the soft threshold noncusp anomalous dimension, which is known to four loops [110, 122–125]. The beam noncusp anomalous dimension $\tilde{\gamma}_B^q[\alpha_s(\mu)]$ then follows from consistency, since the $\overline{\rm MS}$ hard anomalous dimension is likewise known to four loops [115, 126]. In turn, these noncusp anomalous dimensions are also related through consistency relations [127] to those of the inclusive jet function (or the 0-jettiness beam function) and the thrust and 0-jettiness soft functions, which have been independently obtained by direct calculations up to three loops [128, 129].

The rapidity RGEs that the soft and beam functions satisfy are given by

$$-2\nu\frac{\mathrm{d}}{\mathrm{d}\nu}\ln\tilde{B}_q(x,b_T,\mu,\nu/\omega) = \nu\frac{\mathrm{d}}{\mathrm{d}\nu}\ln\tilde{S}_q(b_T,\mu,\nu) = \tilde{\gamma}_\nu^q(b_T,\mu)\,, \qquad (2.17)$$

where the μ and ν anomalous dimensions satisfy an all-order integrability condition,

$$\mu\frac{\mathrm{d}}{\mathrm{d}\mu}\tilde{\gamma}_\nu^q(b_T,\mu) = -4\Gamma_{\rm cusp}^q[\alpha_s(\mu)] = \nu\frac{\mathrm{d}}{\mathrm{d}\nu}\tilde{\gamma}_S^q(\mu,\nu)\,. \qquad (2.18)$$

Eq. (2.18) predicts the all-order logarithmic (b_T) structure of the rapidity anomalous dimension in perturbation theory,

$$\tilde{\gamma}_\nu^q(b_T, \mu) = -4\eta_\Gamma^q(\mu_0, \mu) + \tilde{\gamma}_\nu^q(b_T, \mu_0) + \mathcal{O}(b_T^2),$$

$$\eta_\Gamma^q(\mu_0, \mu) \equiv \int_{\mu_0}^{\mu} \frac{d\mu'}{\mu'} \, \Gamma_{\text{cusp}}^q[\alpha_s(\mu')], \tag{2.19}$$

up to the fixed-order boundary term $\tilde{\gamma}_\nu^q(b_T, \mu_0)$ that necessitates an explicit calculation and is currently known to four loops [93, 96, 130–132]. The four-loop result has been obtained in refs. [131, 132] using an expansion around the critical number of dimensions where QCD is conformal [130], such that the four-loop rapidity anomalous dimension can be evaluated in terms of the four-loop soft threshold noncusp anomalous dimension [110, 122–125] and a correction term that involves explicit calculations of the three-loop threshold soft function to subleading order in the dimensional regulator [131–133]. In addition, the above expression, which holds for $\mu \gtrsim \mu_0 \sim 1/b_T$, receives nonperturbative power corrections of $\mathcal{O}(\Lambda_{\text{QCD}}^2 b_T^2)$ to which we return in section 3.

Solving the coupled system in eqs. (2.16) and (2.17) yields the resummed beam and soft functions,

$$\tilde{B}_q\left(x, b_T, \mu, \frac{\nu}{\omega}\right) = \tilde{B}_q\left(x, b_T, \mu_B, \frac{\nu_B}{\omega}\right) \exp\left[-\frac{1}{2}\ln\frac{\nu}{\nu_B}\tilde{\gamma}_\nu^q(b_T, \mu_B)\right] \exp\left[\int_{\mu_B}^{\mu}\frac{d\mu'}{\mu'}\tilde{\gamma}_B^q(\mu', \nu/\omega)\right],$$

$$\tilde{S}_q(b_T, \mu, \nu) = \tilde{S}_q(b_T, \mu_S, \nu_S)\exp\left[\ln\frac{\nu}{\nu_S}\tilde{\gamma}_\nu^q(b_T, \mu_S)\right]\exp\left[\int_{\mu_S}^{\mu}\frac{d\mu'}{\mu'}\tilde{\gamma}_S^q(\mu', \nu)\right], \tag{2.20}$$

where the exponentials correspond to the Sudakov evolution kernels via which resummation is achieved. Crucially, choosing appropriately the boundary scales $\mu_{H,B,S}$ and $\nu_{B,S}$, the hard, beam, and soft functions are free of large (double) logarithms which results in their well-behaved perturbative convergence, and allows for their evaluation at fixed-order. The beam and soft functions up to N^3LO have been obtained in refs. [96, 99, 100, 134, 135] and are collected in our notation in ref. [127]. The flavor nonsinglet contribution to the massless quark (vector or axial) form factor, which determines the hard function in eq. (2.5), is likewise known to N^3LO [79, 80, 136]. Explicit expressions for the hard functions and nonsinglet matching coefficients in our notation can be found in refs. [22, 134].

In eq. (2.20) we choose to perform the evolution first in ν and then in μ. We stress that any other resummation path in the two-dimensional (μ, ν) plane is equivalent as a result of the RG consistency relations that the anomalous dimensions satisfy.

It has been shown that the evaluation of the Sudakov evolution kernels in eqs. (2.19) and (2.20) based on approximate analytical methods can lead to a numerical discrepancy that can no longer be considered a higher-order effect [61], see also refs. [137, 138], and in addition upsets the so-called closure condition, i.e., the group property of the renormalization group evolution, and the exact path independence in the (μ, ν) plane. Recently, in ref. [139] an exact solution for the evolution kernels and for the running of the strong coupling was derived by recasting the original integrands in a form amenable to partial fractioning and the residue theorem. In our N^3LL' predictions we use these exact analytic solutions for the

β function and Sudakov kernels, which implies that all RGE running is exact and free of any of the usually employed approximations.[3]

2.3 Flavor-singlet hard matching coefficients

SCET Wilson coefficients are the building blocks of the hard function $H_{i\,VV'\,ab}$. They are obtained by matching the full-QCD quark form factors for the underlying hard process $ab \to V, V'$ onto SCET. Specifically, for the neutral current Drell-Yan process $(V, V' = Z/\gamma^*)$, the QCD corrections to the form factors are categorized differently depending on whether a, b directly couple to V, V' or if a quark loop of possibly different flavor couples to V, V'. The former contribution is referred to as the (flavor) nonsinglet matching coefficient, and the latter as the singlet matching coefficient. While the nonsinglet coefficient is the same for axial and vector terms due to chirality and the fact that the external quarks are massless at the hard scale, the axial and vector singlet coefficients differ from each other.

Using the notation of ref. [22], the axial singlet matching coefficient summed over all quark flavors in the Standard Model running in the loop is given by

$$\sum_f a_f \, C_{a\,f}(q^2, m_f^2, \mu) = a_t \, \Delta C_{a\,t,b}(q^2, m_t^2, \mu) + \mathcal{O}\left(\frac{m_b^2}{q^2}\right), \tag{2.21}$$

where the contributions from the other (approximately massless) generations cancel exactly. The two-loop coefficient $\Delta C_{a\,t,b}^{(2)}(q^2, m_t^2)$ is well known [81, 82], including its exact dependence on m_t [83, 85]. We extract the three-loop expression for $\Delta C_{a\,t,b}^{(3)}(q^2, m_t^2, \mu)$ from the recent calculation of all three-loop singlet contributions to the quark form factors in refs. [84, 85]. Our notation relates to that of ref. [85] as $\Delta C_{a\,t,b} = \mathcal{F}_{s,t}'^A - \mathcal{F}_{s,b}'^A$, where $\mathcal{F}_{s,q}'^A$ is the axial singlet contribution to the quark form factor computed in pure dimensional regularization and with infrared poles subtracted in $\overline{\mathrm{MS}}$. We account for the one-loop decoupling relation between $\alpha_s^{(6)}(\mu)$ and $\alpha_s^{(5)}(\mu)$ to extract the individual coefficients $\Delta C_{a\,t,b}^{(2,3)}$ in a truncated expansion in the five-flavor running coupling $\alpha_s^{(5)}(\mu)$. We have checked that the result satisfies the renormalization group running expected from consistency with an effective quark-antiquark operator in SCET with $n_f = 5$ massless quark flavors. We stress the necessity of using the three-loop massless axial vector coefficient [84] together with the corresponding massive piece [85] to ensure that their μ dependence properly cancels. The vector singlet coefficient starts at $\mathcal{O}(\alpha_s^3)$ and receives contributions from all massless quark flavors, which can readily be extracted from the term multiplying the $N_{F,V}$ coefficient in ref. [79]. In addition, there are contributions from closed top-quark loops at $\mathcal{O}(\alpha_s^3 Q^2/(4m_t^2))$, which were likewise calculated in ref. [85]. Here the m_t dependence is purely power suppressed and not logarithmically enhanced since it results from the matching of the conserved vector current. However, based on the observed, negligible numerical effect of the corresponding $\mathcal{O}(Q^2/(4m_t^2))$ corrections

---

[3]An exception are the predictions in figure 11, 12 and 13. There, we consistently employ the approximate unexpanded analytic evolution kernels (or "iterative" solutions) [61] extended to this order for simplicity, see appendix A, although in principle, the method for obtaining their exact solution [139] should also be applicable at N⁴LL. In this case we also consistently use the iterative solutions at lower orders to ensure that comparisons to lower orders are one to one.
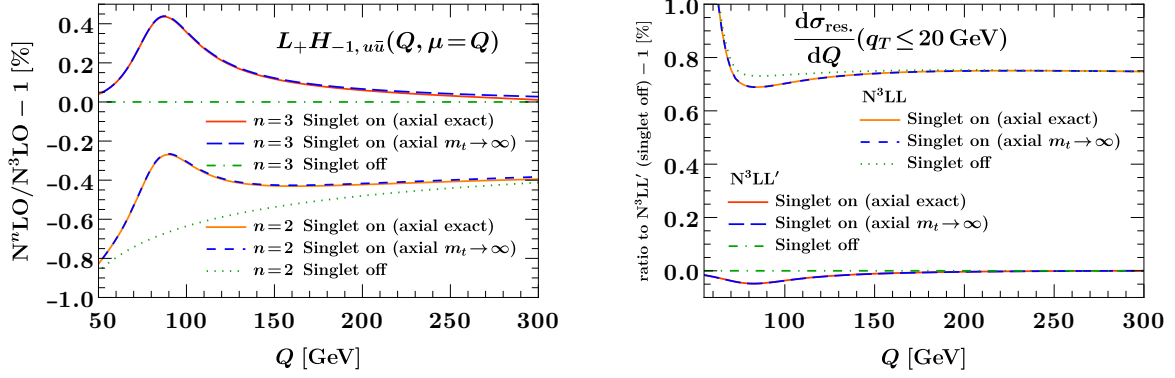
Figure 1. Relative impact of the singlet contributions to the combined inclusive hard function and leptonic coefficient $L_+ H_{-1,u\bar{u}} \equiv \sum_{VV'} L_{+VV'} H_{iVV'u\bar{u}}$ (left) and the resummed cross section (right) for neutral-current Drell-Yan as a function of the dilepton invariant mass Q.

in the axial coefficient (discussed below), we choose to ignore the latter contribution for simplicity and work to leading power in $Q/(2m_t)$.

In the left panel of figure 1 we illustrate the numerical impact of the singlet contributions to the hard function for the $i = -1$ (unpolarized) helicity channel in the $u\bar{u}$ flavor channel at NNLO and at N³LO. Excluding the vector and axial vector singlet terms at both orders results in a $\sim 0.5\%$ deviation from the exact result, especially in the region $Q \sim m_Z$ where the relative impact of the latter terms is enhanced due to the Z resonance. On the other hand, it is evident that the power corrections to the axial coefficient between the exact and the LP $Q \ll m_t$ result are negligible in the range of Q of interest. This justifies using the LP expressions for both the axial and vector singlet contributions. In the right panel of figure 1 we perform the same comparison at the level of the resummed cross section at NNLL′ and N³LL′. The contributions of the axial singlet coefficient to the hard function for up-type and down-type quarks have opposite sign because the axial singlet coefficient is interfered with the nonsinglet one weighted with the respective opposite weak charges. This leads to a large degree of cancellation at the level of the cross section that leaves behind a relative effect of 0.1%. Despite the small size we nevertheless include the full set of singlet coefficients (to leading power in $Q \ll 2m_t$) in our nominal predictions, since (a) they are a part of the nominal NNLL′ and N³LL′ accuracy, respectively, and (b) the degree of cancellation between flavor channels is contingent on the underlying collinear PDF set, and also in general different for the $i = 4$ helicity cross section, i.e., the forward-backward asymmetry.

We stress that keeping these virtual terms to improve the resummed singular cross section is not inconsistent with dropping the corresponding real contributions in fixed-order predictions used to extract the nonsingular cross section as long as one restricts to a range in q_T where the latter is still power-suppressed and numerically small (see the next section). In general, these contributions arise from heavy-quark pair production or from hard gluon radiation out of heavy-quark loops. To leading power in $Q, q_T \ll 2m_t$ the only contribution of this kind, starting at $\mathcal{O}(\alpha_s^3)$, comes from the three-parton real-emission amplitudes involving the effective operator from integrating out the axial contribution of the top quark.
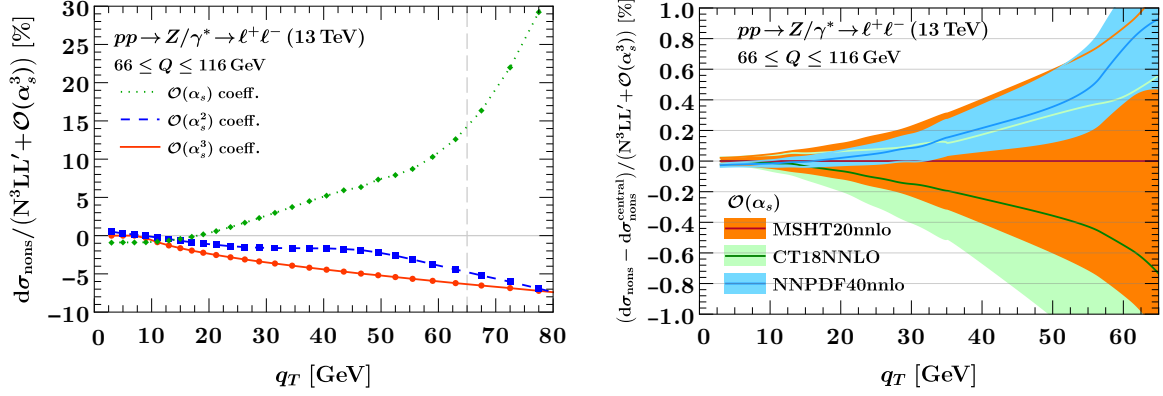
Figure 2. Left: relative contributions from the nonsingular cross section coefficients at different fixed orders to the total fiducial q_T spectrum at $\mathrm{N^3LL'} + \mathcal{O}(\alpha_s^3)$. We use the ATLAS 13 TeV fiducial cuts for definiteness, see eq. (4.1). Right: impact of parametric PDF variations and alternate PDF sets on the $\mathcal{O}(\alpha_s)$ nonsingular cross section with the central `MSHT20nnlo` result as baseline, likewise normalized to the total fiducial q_T spectrum at $\mathrm{N^3LL'} + \mathcal{O}(\alpha_s^3)$. The PDF variations around the solid red line on the right, which give an upper estimate of the corresponding effect on the nonsingular cross section coefficient at $\mathcal{O}(\alpha_s^2)$ and $\mathcal{O}(\alpha_s^3)$, can be thought of as dressing the lines in the plot on the left in the same units (but note the difference in vertical scale).

2.4 Nonsingular cross section

While the singular cross section in eq. (2.6) dominates the spectrum as $q_T \to 0$ and captures all singularities $\delta(q_T)$ and $\alpha_s^n \ln^m(q_T/Q)/q_T$, it corresponds only to the leading term in the expansion of the full cross section in this limit. To include the remaining tower of power-suppressed contributions of $\mathcal{O}(q_T^2/Q^2)$ and higher, usually referred to as the nonsingular cross section, and extend the prediction into the fixed-order (FO) region, we perform an additive matching. In practice, the nonsingular cross section (or "the nonsingular", for short) is obtained by a differential q_T subtraction [140, 141],

$$\frac{\mathrm{d}\sigma_{\mathrm{nons}}}{\mathrm{d}q_T} = \left[\frac{\mathrm{d}\sigma_{\mathrm{FO}}}{\mathrm{d}q_T} - \frac{\mathrm{d}\sigma_{\mathrm{sing}}}{\mathrm{d}q_T} \right]_{q_T > 0}, \tag{2.22}$$

where $\mathrm{d}\sigma_{\mathrm{FO}}/\mathrm{d}q_T$ is the FO cross section for the $Z/W^{\pm} + 1$ parton configuration, and $\mathrm{d}\sigma_{\mathrm{sing}}/\mathrm{d}q_T$ is the singular cross section at the appropriate perturbative order. Both are, in practice, calculated using strict twist-2 collinear factorization, i.e., in terms of standard leading-twist collinear PDFs. Since the outcome of the subtraction in eq. (2.22) is suppressed by q_T^2/Q^2, i.e. numerically significantly smaller in the resummation region $q_T \ll Q$, it typically is sufficient to evaluate it at a fixed scale $\mu \sim \mu_{\mathrm{FO}} \sim Q$ and ignore the shape effect due to its (unknown) all-order resummation. We will further restrict most of our predictions in this paper to a range of $q_T \leq 60 - 65\,\mathrm{GeV}$, on which we empirically find that the nonsingular cross section — extracted as described in the next paragraphs — only amounts to a few-percent contribution to the total q_T spectrum, see the left panel of figure 2. This has the substantial benefit that the nonsingular cross section, e.g. when evaluating parametric PDF uncertainties, may simply be kept at the central member of the PDF set in question (or may even use another, fixed PDF set), since propagating these changes into the nonsingular amounts only to a few-percent

change on top of a few-percent contribution. This substantially reduces the numerical effort involved in obtaining the nonsingular cross section. To make this approximation quantitative, the right panel of figure 2 shows the impact of PDF variations and alternate PDF sets on the $\mathcal{O}(\alpha_s)$ nonsingular cross section, where we normalize the difference to the central $\mathcal{O}(\alpha_s)$ MSHT20nnlo nonsingular cross section to our best prediction for the total q_T spectrum. The impact of these variations, which are computed as described in section 4.3, amounts to less than two permille for $q_T \leq 30\,\text{GeV}$, and less than a percent for $q_T \leq 65\,\text{GeV}$. This effect on the leading $\mathcal{O}(\alpha_s)$ nonsingular cross section (where PDF variations are computationally cheap to perform, and fully retained in all our predictions later on) can serve as an upper estimate of the error one makes when neglecting PDF variations in the smaller contributions from the $\mathcal{O}(\alpha_s^2)$ and $\mathcal{O}(\alpha_s^3)$ nonsingular coefficients, and thus fully justifies this approximation, e.g. when comparing to our final estimate of the total perturbative uncertainty in figure 6, which reaches 1% in the range $5 \leq q_T \leq 30\,\text{GeV}$. Several additional approximations to the nonsingular cross section, which we describe in the following, can be performed by a similar argument without affecting the overall accuracy. We note that these manipulations are not justified when extending the prediction into the far tail where the complete FO prediction must be recovered, and in particular parametric variations must consistently be propagated everywhere. (In appendix B we present such predictions valid for all q_T for a fixed reference PDF set.)

At $\mathcal{O}(\alpha_s)$ we obtain the full cross section for $q_T > 0$, including arbitrary cuts or measurements on the leptonic decay products, from an in-house implementation of the analytic LO_1 structure functions [142–144]. The $\mathcal{O}(\alpha_s^2)$ coefficient is obtained from dedicated, high-precision runs of the publicly available Monte-Carlo program MCFM [145, 146]. For the evaluation of both coefficients we employ the MSHT20nnlo PDF set [147], which we will also use as our default PDF set in final predictions.

For Z + jet production with the ATLAS 13 TeV cuts at $\mathcal{O}(\alpha_s^3)$, we use publicly available, high-precision FO data from the NNLOjet collaboration [43]. In these, we observe that the NNLO_1 K-factor, $K = \text{d}\sigma_{\text{NNLO}_1}/\text{d}\sigma_{\text{NLO}_1}$, is quite small for $q_T \gtrsim 20\,\text{GeV}$ and follows an almost constant trend with $K \approx 0.08$. We furthermore find that the model function

$$f_{\text{nons}}(q_T) = \Theta(q_T - q_T^*)\left(c_1 \ln\frac{q_T}{q_T^*} + c_2 \ln^2\frac{q_T}{q_T^*}\right), \tag{2.23}$$

captures reasonably well the q_T dependence of the ratio

$$\frac{\text{d}\sigma_{\text{nons}}^{(3)}/\text{d}q_T}{\text{d}\sigma_{\text{NLO}_1}/\text{d}q_T}, \tag{2.24}$$

which we use to perform a fit of the coefficients $c_{1,2}$. By multiplying the fitted f_{nons} with $\text{d}\sigma_{\text{NLO}_1}/\text{d}q_T$, we obtain an approximate $\mathcal{O}(\alpha_s^3)$ nonsingular coefficient that in particular is free of the bin-to-bin statistical fluctuations visible in the raw nonsingular result. Note that we use NNLOjet data [43] that employ the NNPDF40nnlo set [148] for the estimation of the model function, which we then multiply with $\text{d}\sigma_{\text{NNLO}}/\text{d}q_T$ evaluated using the MSHT20nnlo PDF set to obtain an approximate nonsingular for the latter (default) set.

The specific choice for the parametrization of $f_{\text{nons}}(q_T)$ is motivated by the expected functional form of the nonsingular cross section. Specifically, the q_T spectrum receives Sudakov

double logarithms at each order in α_s at any order in the power expansion. At N^{3}LO, there are at most two extra powers of the logarithm when dividing out the NNLO full cross section, which we expect to dominate the shape of the ratio. Another notable feature of the model function in eq. (2.23) is that we set the $\mathcal{O}(\alpha_s^3)$ nonsingular coefficient to zero at $q_T \leq q_T^*$ to avoid biasing the shape of the spectrum through the unresummed logarithms of q_T/Q in the nonsingular at very small values of q_T. A priori, such a modification is not compatible with maintaining (even approximate) N^{3}LO accuracy on the normalization of the spectrum, since it effectively amounts to performing a q_T subtraction with an unreasonably high technical cutoff, which in turn is known to substantially bias the total integral. In the present case, however, we rely on a remarkable feature of the available fixed-order data [43], which indicate that the $\mathcal{O}(\alpha_s^3)$ nonsingular coefficient undergoes a sign change around $q_T = 2\,\mathrm{GeV}$ such that its integral up to $q_T^* = 8\,\mathrm{GeV}$ is in fact compatible with zero within the quoted numerical uncertainty. Specifically, we find that the integral of the $\mathcal{O}(\alpha_s^3)$ nonsingular coefficient between the actual technical cutoff of ref. [43] at $q_T^{\mathrm{cut}} = 0.447\,\mathrm{GeV}$ and $q_T^* = 8\,\mathrm{GeV}$ amounts to only

$$\int_0^{q_T^*} \mathrm{d}q_T\, \frac{\mathrm{d}\sigma_{\mathrm{nons}}^{(3)}}{\mathrm{d}q_T} \approx \int_{q_T^{\mathrm{cut}}}^{q_T^*} \mathrm{d}q_T\, \frac{\mathrm{d}\sigma_{\mathrm{nons}}^{(3)}}{\mathrm{d}q_T} = (-0.34 \pm 0.76)\,\mathrm{pb}\,, \tag{2.25}$$

which should be compared to the integral of the prediction at N^{3}LL$'$+$\mathcal{O}(\alpha_s^3)$ over the reference range $q_T \in [0, 65]\,\mathrm{GeV}$, for which we find $673.4\,\mathrm{pb}$, see table 2. Conveniently, this choice of q_T^* therefore lets us preserve both an unbiased shape of the matched spectrum at small $q_T < q_T^*$ as well as the approximate N^{3}LO accuracy of its normalization up to $q_T \approx 70\,\mathrm{GeV}$, i.e., within the approximations in the choice of model function, and accounting for the fact that we use f_{nons} to port the nonsingular from one PDF set to another.

For the extraction of $c_{1,2}$ in eq. (2.23) we perform a two-parameter fit at fixed $q_T^* = 8\,\mathrm{GeV}$ to the data for the $\mathcal{O}(\alpha_s^3)$ nonsingular coefficient at $q_T > q_T^*$. While the lower end of the fit window in q_T is thus fixed, it is still important to assess the impact of the choice of upper endpoint in the fitting procedure. This is because the FO data, and hence also the corresponding nonsingular, are more precise for larger values of q_T since they carry smaller relative statistical uncertainties. On the other hand, increasing the range to q_T values that are too large carries the risk of overfitting and exceeding the physical validity range of the model. To address this, we perform multiple fits of $c_{1,2}$ by gradually extending the q_T fit window while inspecting the values of the R^2 statistic, which provides a convenient goodness-of-fit measure. We find that the optimal fitting range is $8\,\mathrm{GeV} \leq q_T \leq 77.5\,\mathrm{GeV}$, resulting in

$$c_1 = -0.02097 \pm 0.00149\,, \quad c_2 = -0.005737 \pm 0.000804\,, \quad R^2 = 0.994\,. \tag{2.26}$$

The best-fit model function and the original data are shown in the top left panel of figure 3, where we also indicate the perturbative uncertainty on the nonsingular cross section at NLO$_1$ (estimated as described in section 4.1) for comparison.

We stress that the fit we perform here does not meet the level of rigor found in state-of-the-art nonsingular fits that can actually *guarantee* a given fixed-order accuracy on the total cross section in the context of q_T or $\mathcal{T}_N$ subtractions. These fits in particular allow one to thoroughly assess the uncertainty from extrapolating the nonsingular down to $q_T \to 0$, see refs. [23, 43, 149, 150], but necessarily involve a fit function whose functional form contains
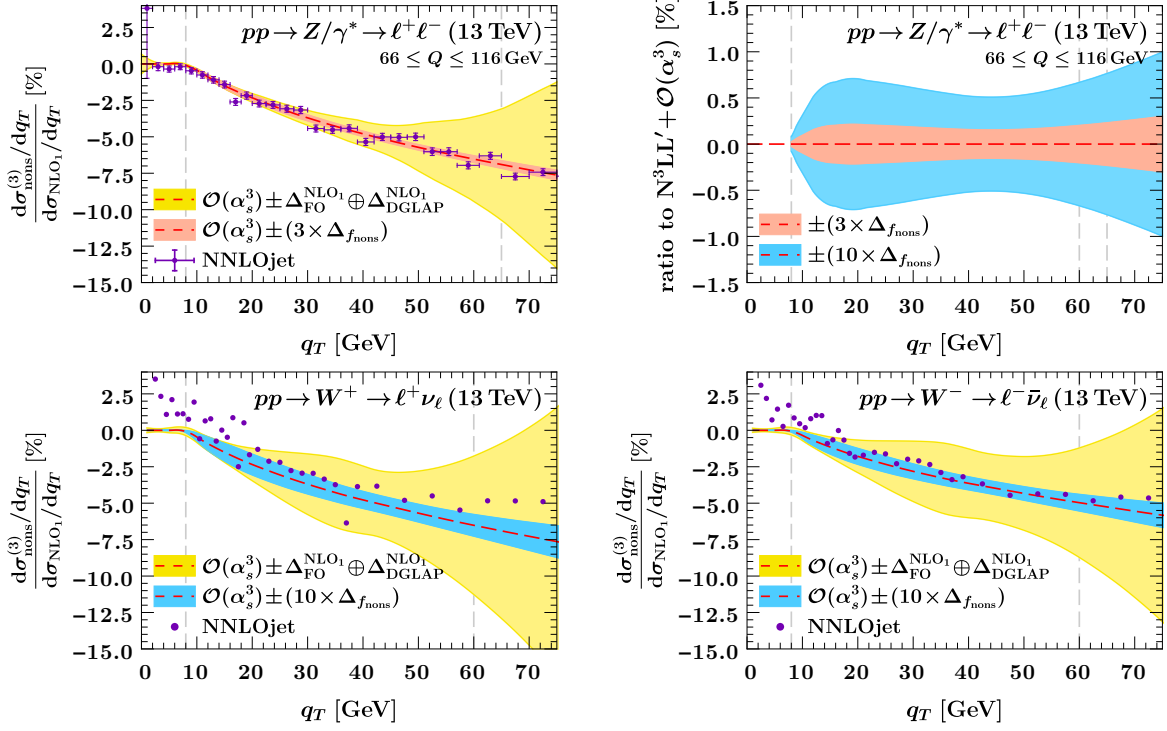
Figure 3. Comparison of the fitted approximate $\mathcal{O}(\alpha_s^3)$ nonsingular coefficient against `NNLOjet` data [43] for the neutral (top left) and the charged-current (bottom) Drell-Yan process. We normalize to the total $\mathcal{O}(\alpha_s^2)$ (NLO$_1$) fixed-order q_T spectrum, as also done in the fit functional form in eq. (2.24). The red and blue bands indicate the error due to our approximate treatment of the $\mathcal{O}(\alpha_s^3)$ nonsingular coefficient, which is estimated by conservatively scaling up the error obtained from fitting to the nonsingular model function for the Z case, as described in the text. As a point of reference, the yellow bands indicate the total perturbative uncertainty on the NLO$_1$ nonsingular cross section, see section 4.1. The top right panel shows the same estimated approximation error as the red and blue bands in the other plots, respectively, but normalized to show the relative impact of the error on the final matched prediction at N^{3}LL$'$ + $\mathcal{O}(\alpha_s^3)$. Vertical dashed gray lines indicate $q_T^* = 8\,\text{GeV}$ and the upper edge 65 GeV (60 GeV) of the range on which we provide predictions for the Z (the $W^\pm$).

all logarithmic terms present in the $\mathcal{O}(q_T^2/Q^2)$ and $\mathcal{O}(q_T^4/Q^4)$ terms of the nonsingular at a given order, possibly using analytic knowledge of the highest logarithms to reduce the number of free parameters. Instead, our goal here is to obtain an approximate form of the nonsingular that is convenient to use, appropriately captures the physical few-percent effect for $q_T = 20$-$60\,\text{GeV}$, and smoothens out statistical fluctuations at the level of the finely-binned q_T spectrum, while still roughly maintaining the fixed-order accuracy of the total integral.

Ready-to-use fixed-order data at $\mathcal{O}(\alpha_s^3)$ of similar quality are not yet available for $W^\pm$ production, inclusive Z production, or fiducial Z production with CMS 13 TeV cuts.[4] With the same goal for the nonsingular in mind as above, and in line with the overall focus of this paper on the state-of-the-art resummed physics, we continue to make use of our model function in eq. (2.23) to obtain an approximate $\mathcal{O}(\alpha_s^3)$ nonsingular cross sections also for these

---

[4]We note that a public implementation of Z + jet production at $\mathcal{O}(\alpha_s^3)$ has in the meantime become available [40], but requires substantial computing resources.

processes. Specifically, in these cases we apply $f_{\rm nons}(q_T)$, which we take to be universal, to the $\rm NLO_1$ full cross section for the respective process obtained from our in-house implementation at $\mathcal{O}(\alpha_s)$ and from MCFM at $\mathcal{O}(\alpha_s^2)$. For $W^{\pm}$ production, we are able to qualitatively compare our approximate $\mathcal{O}(\alpha_s^3)$ nonsingular coefficient to the data provided in the ancillary files of ref. [151] as a cross check, using the fiducial cuts given in that reference.[5] The comparison is shown in the bottom two panels figure 3. We observe reasonable agreement on the shape, sign, and magnitude of the nonsingular cross section, in particular at $q_T > 20\,{\rm GeV}$, giving us confidence that the dominant physics of the nonsingular cross section for $V + {\rm jet}$ production are indeed captured by eq. (2.24).

To conclude this section, we estimate the error associated with this approximate treatment of the $\mathcal{O}(\alpha_s^3)$ nonsingular cross section coefficient, specifically the error affecting the shape of the spectrum at $q_T \geq q_T^*$, and propagate it into our final predictions. To do so, we propagate the fit uncertainty on the parameters c_1 and c_2 of the nonsingular model function $f_{\rm nons}$ into an uncertainty $\Delta_{f_{\rm nons}}$ on the $\mathcal{O}(\alpha_s^3)$ nonsingular cross section coefficient. We then conservatively scale this uncertainty up by a factor of 3 in the case of the Z boson to reflect the fact that the functional form of the model only captures the nonsingular coefficient in a simplified way. The result is shown as a red band in the top left panel of figure 3. In the case of the $W^{\pm}$, we scale $\Delta_{f_{\rm nons}}$ up by a factor of 10 to in addition reflect the fact that it was ported from one (related) process to another. The result is shown as a blue band in the bottom two panels of figure 3. We find that with these scaling factors, our estimate of the approximation error covers both the scatter of the nonsingular data and its residual deviations from our approximate model for the $W^{\pm}$ to a reasonable degree on the range of $20 < q_T < 60\,{\rm GeV}$, where both the data and the model can be considered reliable. The top right panel shows the same two bands, but instead normalized to our final prediction at $\rm N^3LL' + \mathcal{O}(\alpha_s^3)$. It is instructive to already at this point compare the estimated approximation error to the final perturbative uncertainty $\Delta_{\rm pert}$, see figure 5, 6 and 17. Focussing on the range of $10 < q_T < 20\,{\rm GeV}$, where $\Delta_{\rm pert}$ reaches the level of 1%, we find that the approximation is fully justified for the Z boson, with the relative approximation error (red) reaching at most a level of 0.2%, and indeed mainly serves to smoothen out the nonsingular data. For the $W^{\pm}$, the estimated approximation error of $\approx 0.6\%$ (blue) does not constitute a bottleneck at the present time, but dedicated high-statistics Monte-Carlo campaigns for the nonsingular cross section, or more efficient techniques to evaluate it, would certainly be desirable in the future.

2.5 Matching and profile scale choices

The final matched prediction is obtained as

$$\frac{{\rm d}\sigma_{\rm match}}{{\rm d}q_T} = \frac{{\rm d}\sigma_{\rm res}}{{\rm d}q_T} + \frac{{\rm d}\sigma_{\rm nons}}{{\rm d}q_T} = \frac{{\rm d}\sigma_{\rm res}}{{\rm d}q_T} + \frac{{\rm d}\sigma_{\rm FO}}{{\rm d}q_T} - \frac{{\rm d}\sigma_{\rm sing}}{{\rm d}q_T} \,, \qquad (2.27)$$

where ${\rm d}\sigma_{\rm res}$ is the differential resummed cross section obtained from a numerical Bessel transform, as given by the first line of the right-hand side of eq. (2.6), and ${\rm d}\sigma_{\rm nons}$ is the

---

[5]We did not attempt a dedicated fit to these data for $W^{\pm}$ production because no statistical uncertainties were provided with ref. [151]. Note that to produce the bottom two panels of figure 3, we also extracted the overall normalization of the full fixed-order data in ref. [151] by adjusting it to recover the expected power suppression of the nonsingular as $q_T \to 0$.
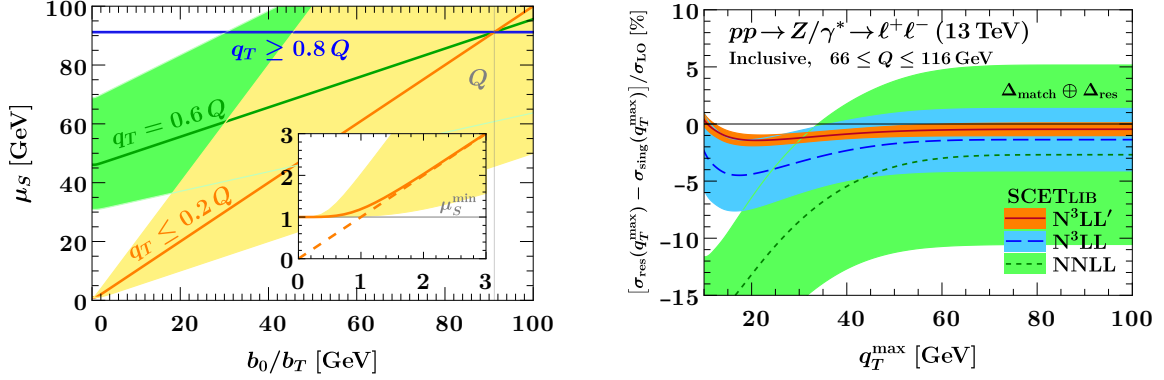
Figure 4. Left: illustration of the hybrid profile scales and the Landau pole treatment, using the soft virtuality scale μ_S as an example. The bands indicate μ_S variations entering the resummation uncertainty estimate as described in section 4.1. Right: difference of the resummed and the fixed-order singular cumulative inclusive cross section (i.e., without fiducial cuts) at various orders. The difference is compatible with zero as $q_T^{\max} \to Q$ within the relevant combined resummation and matching uncertainty $\Delta_{\mathrm{res}} \oplus \Delta_{\mathrm{match}}$, which is estimated as described in section 4.1.

nonsingular cross section evaluated at fixed order, as defined in eq. (2.22). At large q_T, the resummation in $d\sigma_{\mathrm{res}}$ must be turned off to ensure that it cancels the fixed-order singular cross section $d\sigma_{\mathrm{sing}}$ and the total fixed-order prediction is recovered.[6,7] Thus in practice, the scales in eqs. (2.14) and (2.15) need to be modified to perform the fixed-order matching at large q_T. We achieve this using hybrid profile scales [153],

$$
\begin{aligned}
\mu_B &= \mu_{\mathrm{FO}}\, f_{\mathrm{run}}\!\left(\frac{q_T}{Q}, \frac{1}{Q}\mu_*\!\left(\frac{b_0}{b_T}, \mu_B^{\min}\right)\right), & \nu_B &= \mu_{\mathrm{FO}}\,, \\
\mu_S &= \mu_{\mathrm{FO}}\, f_{\mathrm{run}}\!\left(\frac{q_T}{Q}, \frac{1}{Q}\mu_*\!\left(\frac{b_0}{b_T}, \mu_S^{\min}\right)\right), & \nu_S &= \mu_{\mathrm{FO}}\, f_{\mathrm{run}}\!\left(\frac{q_T}{Q}, \frac{1}{Q}\mu_*\!\left(\frac{b_0}{b_T}, \nu_S^{\min}\right)\right), \\
\mu_0 &= \mu_*\!\left(\frac{b_0}{b_T}, \mu_0^{\min}\right), & \mu_f &= \mu_F\, f_{\mathrm{run}}\!\left(\frac{q_T}{Q}, \frac{1}{Q}\mu_*\!\left(\frac{b_0}{b_T}, \mu_f^{\min}\right)\right) \quad (2.28)
\end{aligned}
$$

---

[6]On a practical note, recovering the fixed-order spectrum exactly also requires expanding the different fixed-order boundary conditions in the resummed cross section against each other, and truncating in the overall number of powers of α_s (also at different scales).

[7]Note that the resummed cross section also contains all leading nonperturbative effects of $\mathcal{O}[\Lambda_{\mathrm{QCD}}^{n+m}/(q_T^n Q^m)]$ with $m = 0, 1$, as discussed in section 3. These corrections are absent in the nonsingular cross section, which is calculated using strict leading-twist collinear factorization, and could thus potentially also upset the cancellation between the resummed and singular cross sections at large q_T. However, the scaling of even the most severe $\mathcal{O}(\Lambda_{\mathrm{QCD}}^2/q_T^2)$ correction, which is maintained by the Bessel transform [152], is such that their numerical effect already at $q_T \sim 30\,\mathrm{GeV}$ is negligible. For performance reasons we in practice stop using the numerical Bessel transform altogether when the resummation is fully turned off for all scale and matching parameter variations and for all points in the considered Q intervals, which amounts to $q_T \geq 125\,\mathrm{GeV}$ for the numerical results presented in this paper.

where $\mu_{\rm FO} = \mu_F = \mu_H = Q$ is the central fixed-order scale used in our predictions, and

$$f_{\rm run}(x, y) = 1 + g_{\rm run}(x)(y - 1), \qquad (2.29)$$

$$g_{\rm run}(x) = \begin{cases} 1, & 0 < x \leq x_1, \\ 1 - \frac{(x-x_1)^2}{(x_2-x_1)(x_3-x_1)}, & x_1 < x \leq x_2, \\ \frac{(x-x_3)^2}{(x_3-x_1)(x_3-x_2)}, & x_2 < x \leq x_3, \\ 0, & x_3 \leq x, \end{cases}$$

ensures that the scales evaluate to the canonical b_T-space scales for $x = q_T/Q < x_1$, and smoothly transition to constant fixed values $\mu_{\rm FO}$ as $x \to x_3$, as illustrated in the left panel of figure 4.[8] Based on the observed size of the nonsingular cross section, we choose

$$(x_1, x_2, x_3) = (0.3, 0.6, 0.9) \qquad (2.30)$$

for our central predictions. This choice of matching points has the important property that the integral of the resummed and matched inclusive spectrum indeed recovers the fixed-order result, as it must because fiducial resummation effects [22] are absent in that case. We verify this property in the right panel of figure 4, where we show the difference

$$\int^{q_T^{\rm max}} {\rm d}q_T \frac{{\rm d}\sigma_{\rm match}^{\rm incl}}{{\rm d}q_T} - \int^{q_T^{\rm max}} {\rm d}q_T \frac{{\rm d}\sigma_{\rm FO}^{\rm incl}}{{\rm d}q_T}$$

$$= \int^{q_T^{\rm max}} {\rm d}q_T \frac{{\rm d}\sigma_{\rm res}^{\rm incl}}{{\rm d}q_T} - \int^{q_T^{\rm max}} {\rm d}q_T \frac{{\rm d}\sigma_{\rm sing}^{\rm incl}}{{\rm d}q_T} \equiv \sigma_{\rm res}(q_T^{\rm max}) - \sigma_{\rm sing}(q_T^{\rm max}) \qquad (2.31)$$

of the resummed and the fixed-order singular cumulative inclusive cross section as a function of the upper integral cutoff $q_T^{\rm max}$ at different orders. To give a sense of the effect size, we normalize the difference to the leading-order inclusive Drell-Yan cross section, which evaluates to $\sigma_{\rm LO}^{\rm incl} = 1182.8\,{\rm pb}$ for our settings. (The nonsingular cross section exactly drops out in the difference, and therefore need not be included.) We find that within the relevant combined resummation and matching uncertainty $\Delta_{\rm res} \oplus \Delta_{\rm match}$ estimated as described in section 4.1, the integral of the resummed cross section indeed recovers the fixed-order result. While more complicated implementations of the matching such as cumulant scales or the so-called Bolzano algorithm [154] exist that would make the agreement exact, we conclude that the hybrid (spectrum) scales we use here already ensure the fixed-order integral property to a sufficient degree. This behavior of spectrum scales strongly differs e.g. from that of the thrust observable considered in ref. [154], and is due to the fact that for the bulk of the cross section in the peak, the b_T-space scales are in fact canonical and independent of q_T in our construction, such that up to fiducial resummation effects, the cumulant integral can directly be taken at the level of the Bessel integral kernel in eq. (2.7) without having to integrate the scales by parts.

---

[8]An alternative way of implementing the transition is by raising y to a power as $f_{\rm run}^{\rm alt}(x, y) = y^{g_{\rm run}(x)}$, which directly translates to controlling the size of the resummed logarithms since y ultimately appears as a ratio of scales in the resummed cross section. We have verified that this alternative choice leads to predictions that show quantitatively similar behavior in the transition region and are completely compatible with the above within the matching uncertainty defined in section 4.1. All numerical predictions given in this paper are obtained using eq. (2.29).

The central profile scales in eq. (2.28) serve the additional purpose of freezing out the scales at which the perturbative components in eq. (2.28) are evaluated before b_0/b_T reaches the Landau pole of QCD. This is implemented through the function μ_* appearing in the second argument of $f_{\rm run}$ in eq. (2.28) and controlled by, in general, four additional parameters $\mu_B^{\min}, \mu_S^{\min}, \nu_S^{\min}, \mu_f^{\min} \sim 1\,{\rm GeV}$. The function $\mu_*(a,b)$ must be a monotonic function of a and in addition have the following asymptotic behavior,

$$a \gg b: \qquad \mu_*(a,b) = a\left[1 + \mathcal{O}\left(\frac{b^p}{a^p}\right)\right],$$

$$a \ll b: \qquad \mu_*(a,b) = b\left[1 + \mathcal{O}\left(\frac{a^q}{b^q}\right)\right], \tag{2.32}$$

where $p, q > 0$ are positive powers. This ensures that at perturbative $b_0/b_T \gg \Lambda_{\rm QCD}$ (and $q_T \ll Q$, specifically $q_T \leq x_1 Q$), the profile scales in eq. (2.28) indeed evaluate to the canonical scales in eq. (2.14) up to power corrections of $(\Lambda_{\rm QCD}b_T)^p$. In the opposite limit $b_0/b_T \lesssim \Lambda_{\rm QCD}$ it ensures that the profile scales remain bounded from below by the respective minimum scale.

Various choices for μ_* have been considered in the literature. One common choice going back to Collins and Soper [66] is to use

$$\mu_*^{\rm CS}(a,b) = \sqrt{a^2 + b^2}, \tag{2.33}$$

which results in $p = q = 2$. Here, $p \geq 2$ is desirable because it ensures that the Landau pole prescription does not introduce spurious power corrections with stronger scaling than the genuine $\Lambda_{\rm QCD}^2 b_T^2$ power corrections to the leading term of the OPEs in eq. (2.10). As discussed in ref. [152], this scheme may be extended to ensure that also higher powers in the OPE are not contaminated by the Landau pole prescription. Two simple options are

$$\mu_*^{\rm CS4}(a,b) = (a^4 + b^4)^{\frac{1}{4}}, \tag{2.34a}$$

$$\mu_*^{\exp}(a,b) = \begin{cases} a\left[1 - \exp\left(-\frac{2}{2b/a-1}\right)\right]^{-1}, & a < 2b, \\ a, & a \geq 2b. \end{cases} \tag{2.34b}$$

leading to $p = q = 4$ and $p = q = \infty$, respectively. The emphasis of our analysis is on the treatment of the $\mathcal{O}(\Lambda_{\rm QCD}^2 b_T^2)$ power corrections, so the $\mu_*^{\rm CS4}$ prescription that guarantees their direct field-theoretic interpretation in terms of higher-twist matrix elements is sufficient for our purposes, and we thus adopt it throughout our numerical results.[9] We pick the minimum scales as

$$\mu_B^{\min} = \mu_S^{\min} = \mu_0^{\min} = 1\,{\rm GeV}, \qquad \nu_S^{\min} = 0. \tag{2.35}$$

For $\mu_f^{\min}$ we pick the maximum of the Q_0 value of the respective PDF set, i.e., down to which value of $Q_0 \leq \mu$ the LHAPDF interpolation grid is provided, and the value of the charm quark mass as quoted in the PDF set. This avoids both extrapolation outside of the LHAPDF grid and large effects from the charm threshold, which is effectively screened by this prescription.

---

[9]We note that the Pavia prescription $\mu_*^{\rm Pavia}(a,b) = b\left[1 - \exp\left(-b^4/a^4\right)\right]^{-\frac{1}{4}}$ introduced in ref. [155] also has $p = 4 > 2$ (and $q = \infty$).

At the same time, it allows us to resum Sudakov logarithms to the largest extent possible by letting the scales relevant for it (μ_B, μ_S, ν_S) decrease further until $1\,\mathrm{GeV}$.

Following this prescription in practice, we set $\mu_f^{\min} = 1.65\,\mathrm{GeV}$ (Q_0) for the NNLO PDF sets by the NNPDF collaboration [148, 156], whereas for the aN³LO [28] set we use $\mu_f^{\min} = 1.51\,\mathrm{GeV}$ (charm mass). For all sets produced by the MSHT collaboration [27, 147] we set $\mu_f^{\min} = 1.40\,\mathrm{GeV}$ (charm mass), and for sets by the CTEQ collaboration [157] $\mu_f^{\min} = 1.30\,\mathrm{GeV}$ (charm mass).

For the convenience of the reader, we again present the equivalent profile scales in terms of TMD boundary scales, which are a ready-to-use implementation of large-q_T fixed-order matching for general TMD studies (suitably adjusting the μ_* function to recover existing scale choices at small q_T). The explicit relations for the central scale choices are

$$\mu_{\mathrm{init}} = \mu_{\mathrm{FO}}\, f_{\mathrm{run}}\left(\frac{q_T}{Q}, \frac{1}{Q}\mu_*\left(\frac{b_0}{b_T}, \mu_{\mathrm{init}}^{\min}\right)\right),$$

$$\sqrt{\zeta_{\mathrm{init}}} = \mu_{\mathrm{FO}}\, f_{\mathrm{run}}\left(\frac{q_T}{Q}, \frac{1}{Q}\mu_*\left(\frac{b_0}{b_T}, \sqrt{\zeta_{\mathrm{init}}^{\min}}\right)\right),$$

$$\mu_{\mathrm{fin}} = \sqrt{\zeta_{\mathrm{fin}}} = \nu_B = \mu_{\mathrm{FO}}, \tag{2.36}$$

where μ_0 is common to both approaches, and identifying a combined TMD PDF requires setting $\nu_S^{\min} = \sqrt{\zeta_{\mathrm{init}}^{\min}}$ and $\mu_{\mathrm{init}}^{\min} = \mu_B^{\min} = \mu_S^{\min}$ such that $\nu_S = \sqrt{\zeta_{\mathrm{init}}}$ and $\mu_B = \mu_S$ for central scales. It is also instructive to discuss how the above prescription relates to standard, so-called b^* prescriptions. Assuming an identical functional form of μ_*, a "local" b^* prescription acting only on boundary scales is obtained by setting

$$\mu_B^{\min} = \mu_S^{\min} = \nu_S^{\min} = \mu_0 = \mu_f = \mu_{\mathrm{init}}^{\min} = \sqrt{\zeta_{\mathrm{init}}^{\min}} = \frac{b_0}{b_{\mathrm{max,local}}}. \tag{2.37}$$

Note that some implementations that only act on virtuality scales entering the strong coupling or the PDFs may instead require $\nu_S^{\min} = \zeta_{\mathrm{init}}^{\min} = 0$, corresponding to our earlier choice. By contrast, a "global" b^* prescription amounts to globally replacing b_T by a suitable function $b^*(b_T)$ of the form b_0/μ_* such that $b^*(b_T) \to b_{\mathrm{max,global}}$ as $b_T \to \infty$. Specifically, this replacement is performed everywhere under the Fourier integral in eq. (2.7) except for the integral kernel, including in particular the b_T arguments of the TMDs themselves, i.e.,

$$[B_a B_b S](Q^2, x_a, x_b, \vec{q}_T, \mu_{\mathrm{fin}})\big|_{\mathrm{global}}$$
$$= \frac{1}{2\pi}\int_0^\infty \mathrm{d}b_T\, b_T\, J_0(b_T q_T)\, \tilde{f}_a(x_a, b_*, \mu_{\mathrm{init}}(b^*), \zeta_{\mathrm{init}}(b^*))\, \tilde{f}_b(x_b, b_*, \mu_{\mathrm{init}}(b^*), \zeta_{\mathrm{init}}(b^*))$$
$$\times U^2(\mu_{\mathrm{init}}(b^*), \zeta_{\mathrm{init}}(b^*), \mu_{\mathrm{fin}}, \zeta_{\mathrm{fin}} = \mu_{\mathrm{fin}}^2), \tag{2.38}$$

where U is the combined quark TMD PDF evolution kernel. The scales $\mu_{\mathrm{init}}(b^*)$ and $\zeta_{\mathrm{init}}(b^*)$ may still be chosen as above to implement the fixed-order matching using hybrid profile scales (but without an additional Landau prescription at the level of the scales, which would be redundant in this case).

3 Nonperturbative TMD dynamics

3.1 Sources of nonperturbative contributions

The resummed unpolarized TMD PDFs entering the factorized cross section in eq. (2.6), including all possible nonperturbative effects allowed by the structure of TMD factorization, take the following form [158]:

$$\tilde{f}_i(x, b_T, \mu, \zeta) = \tilde{f}_i^{\text{pert}}(x, b_T, \mu_{\text{init}}, \zeta_{\text{init}}) \, U_i(\mu_{\text{init}}, \mu, \zeta_{\text{init}}) \, V_i(b_T, \mu, \zeta_{\text{init}}, \zeta) \, \tilde{f}_i^{\text{np}}(x, b_T) \quad (3.1)$$

Here $\tilde{f}_i^{\text{pert}}$ denotes the leading term in the OPE in eq. (2.10) evaluated at boundary scales μ_{init} and ζ_{init} using a Landau pole prescription such as in eq. (2.28),[10] U_i denotes the virtuality evolution of the TMD PDF at a fixed CS scale (which is purely perturbative by consistency with the hard function), and V_i denotes the CS evolution kernel at fixed μ, which contains a nonperturbative component discussed below. Finally, $\tilde{f}_i^{\text{np}}(x, b_T)$ denotes the nonperturbative contribution to the TMD PDF boundary condition, which can be interpreted as the intrinsic transverse momentum spectrum of partons within the proton.

The CS evolution factor V_i in eq. (3.1) is obtained by solving [158]

$$\gamma_\zeta^i(b_T, \mu) = 2 \frac{\mathrm{d}}{\mathrm{d}\ln\zeta} \ln \tilde{f}_i(x, b_T, \mu, \zeta)$$
$$= -\frac{\mathrm{d}}{\mathrm{d}\ln\nu} \ln \tilde{B}_i(b_T, \mu, \nu) = +\frac{1}{2} \frac{\mathrm{d}}{\mathrm{d}\ln\nu} \ln \tilde{S}_i(b_T, \mu, \nu) = \frac{1}{2} \tilde{\gamma}_\nu^i(b_T, \mu) \,, \quad (3.2)$$

where γ_ζ^i is known as the Collins-Soper kernel, and we have included its relation to the beam and soft rapidity anomalous dimensions in the rapidity renormalization group approach [75, 88] for reference. (Note that as in ref. [127], we reserve the symbol $\tilde{\gamma}_\nu^i$ for the *soft* rapidity anomalous dimension, in contrast to section 4.5 of ref. [158].) Similar to the TMD PDFs in eq. (3.1), the CS kernel contains an evolution term resumming logarithms of μb_T, a fixed-order boundary condition evaluated at $\mu_0 \sim b_T$ for $b_0/b_T \gg \Lambda_{\text{QCD}}$, and a nonperturbative contribution, which in this case are all additive [158],

$$\tilde{\gamma}_\zeta^i(b_T, \mu) = -2\eta_\Gamma^i(\mu_0, \mu) + \tilde{\gamma}_\zeta^i(b_T, \mu_0) + \tilde{\gamma}_\zeta^{i,\text{np}}(b_T) \,. \quad (3.3)$$

Expressions for the fixed-order boundary condition $\tilde{\gamma}_\zeta^i(b_T, \mu_0)$ and a recursive analytic solution for η_Γ^i to $\mathrm{N}^4\mathrm{LL}$ are given in appendix A, while the exact analytic solution for the latter to $\mathrm{N}^3\mathrm{LL}$ is given in ref. [139]. Following the split of perturbative and nonperturbative physics in $\tilde{\gamma}_\zeta^i$, we accordingly define their exponentials as

$$V_i(b_T, \mu, \zeta_{\text{init}}, \zeta) = \exp\left[\frac{1}{2}\tilde{\gamma}_\zeta(b_T, \mu) \ln\left(\frac{\zeta}{\zeta_{\text{init}}}\right)\right] \equiv V_i^{\text{pert}}(b_T, \mu, \zeta_{\text{init}}, \zeta) \, V_i^{\text{np}}(b_T, \zeta_{\text{init}}, \zeta) \,, \quad (3.4)$$

which together make up the total CS kernel. For later convenience we also define

$$\tilde{f}_i(x, b_T, \mu, \zeta) \equiv \tilde{f}_i^{\text{pert}}(x, b_T, \mu, \zeta) \, V_i^{\text{np}}(b_T, \zeta_{\text{init}}, \zeta) \, \tilde{f}_i^{\text{np}}(x, b_T)$$
$$\equiv \tilde{f}_i^{\text{pert+np}_\zeta}(x, b_T, \mu, \zeta) \, \tilde{f}_i^{\text{np}}(x, b_T) \,, \quad (3.5)$$

---

[10]The additional deformation of the scales to implement the fixed-order matching for $q_T \to Q$ is not relevant here, since it is of higher order in q_T/Q than the formal accuracy of the TMD factorization itself.

i.e., the purely perturbative TMD PDF $\tilde{f}_i^{\text{pert}}$ including the U_i evolution to μ and the perturbative component of the CS evolution from ζ_{init} to ζ, and the TMD PDF $\tilde{f}_i^{\text{pert+np}\zeta}$ including in addition the nonperturbative part of the CS evolution (but still excluding the nonperturbative TMD boundary condition).

We remind the reader of the well-known fact that $\tilde{f}_i^{\text{np}}(x, b_T)$, $\gamma_\zeta^{q,\text{np}}(b_T)$, and the entire notion of "splitting" perturbative and nonperturbative physics are defined with respect to a given choice of boundary scales (i.e. in particular, a given Landau pole prescription), for which many choices are available in the literature, see e.g. refs. [66, 155, 159]. Meaningful comparisons and conversions between them must therefore be performed at the level of the complete TMD PDF in eq. (3.1). Nevertheless, the interpretation of the nonperturbative functions can be made more straightforward if the Landau pole prescription in μ_{init} and μ_0 (and possibly ζ_{init}) is of $\mathcal{O}(\Lambda_{\text{QCD}}^p b_T^p)$ with $p > 2$ [152]. In this case the power expansions of the model functions are in direct correspondence to the first subleading terms in the OPEs of the TMD PDF and the CS kernel in eqs. (2.10) and (2.19). Combining them, they read as follows,

$$f_i(x, b_T, \mu, \zeta) = \left[\sum_j \int \frac{\mathrm{d}z}{z} \tilde{C}_{ij}(z, b_T, \mu, \zeta) f_j\left(\frac{x}{z}, \mu\right) \right]$$
$$\times \left[1 + b_T^2 \left(\Lambda_i^{(2)}(x) + \frac{1}{2} \gamma_{\zeta,i}^{(2)} \ln \frac{b_T^2 \zeta}{b_0} \right) + \mathcal{O}(\Lambda_{\text{QCD}}^4 b_T^4) \right], \qquad (3.6)$$

and relate to the nonperturbative functions introduced above as

$$\tilde{\gamma}_\zeta^{i,\text{np}}(b_T) = \gamma_{\zeta,i}^{(2)} b_T^2 + \mathcal{O}(\Lambda_{\text{QCD}}^4 b_T^4), \qquad \tilde{f}_i^{\text{np}}(x, b_T) = 1 + \Lambda_i^{(2)} b_T^2 + \mathcal{O}(\Lambda_{\text{QCD}}^4 b_T^4). \qquad (3.7)$$

Here $\gamma_{\zeta,i}^{(2)}$ is a single number given by a gluon vacuum condensate [160], and $\Lambda_i^{(2)}(x)$ is a function of x and the flavor i given by a normalized combination of twist-4 collinear matrix elements. If the Landau pole prescription instead starts at $p = 2$, the relation must include total derivatives of the perturbative piece with respect to b_T in addition, and analogously for higher terms in the OPE and Landau pole prescriptions of higher order. Here we ignore — as is common in the literature — the possible presence of anomalous powers of Λ_{QCD} from the RG evolution of the condensate and the higher-twist matrix elements that is not captured by that of the twist-2 ingredients. I.e., taking the nonperturbative function to be analytic at $b_T = 0$ appropriately captures the higher-twist contributions for $\Lambda_{\text{QCD}} b_T \ll 1$ when working to leading order for their Wilson coefficient and ignoring their running. Finally, we note that while the leading $\mathcal{O}(\Lambda_{\text{QCD}}^2 b_T^2)$ renormalons in the CS kernel and TMD PDFs are known to be nonzero [161], we do not include any renormalon subtractions, which is motivated *a posteriori* by the excellent convergence we observe in our predictions towards higher perturbative orders, see sections 4, 5 and 6.

We note that while we mostly choose to work in TMD notation in this section for definiteness and to make contact with the literature, one can indeed express all results in a completely equivalent way by introducing nonperturbative functions $\tilde{B}_i^{\text{np}}(x, b_T)$ and $\sqrt{S_i^{\text{np}}}(b_T)$ for the beam and soft functions at their respective boundary scales, where one may choose $S_i^{\text{np}} = 1$ and $\tilde{f}_i^{\text{np}}(x, b_T) = \tilde{B}_i^{\text{np}}(x, b_T)$ without loss of generality through a suitable rapidity renormalization scheme. In our final predictions based on eqs. (3.19) and (3.27)

(which in practice will use effective models, but the same could be done with a more detailed model for the underlying $\tilde{f}_i^{\mathrm{np}}$), we evaluate the evolved perturbative TMD PDF dressing the nonperturbative model functions in the more general form of the rapidity renormalization framework as in eq. (2.20), explicitly,

$$
\begin{aligned}
\tilde{f}_i^{\mathrm{pert+np}\zeta} &\left(x, b_T, \mu, \zeta\right) \\
&= \tilde{B}_i^{\mathrm{pert}}\left(x, b_T, \mu_B, \frac{\nu_B}{\sqrt{\zeta}}\right) \exp\left[-\frac{1}{2}\ln\frac{\nu}{\nu_B}\tilde{\gamma}_\nu^i(b_T, \mu_B)\right] \exp\left[\int_{\mu_B}^\mu \frac{\mathrm{d}\mu'}{\mu'}\tilde{\gamma}_B^i\left(\mu', \frac{\nu}{\sqrt{\zeta}}\right)\right] \\
&\quad \times \sqrt{\tilde{S}_i^{\mathrm{pert}}}(b_T, \mu_S, \nu_S) \exp\left[\frac{1}{2}\ln\frac{\nu}{\nu_S}\tilde{\gamma}_\nu^i(b_T, \mu_S)\right] \exp\left[\frac{1}{2}\int_{\mu_S}^\mu \frac{\mathrm{d}\mu'}{\mu'}\tilde{\gamma}_S^i(\mu', \nu)\right],
\end{aligned}
\tag{3.8}
$$

which in particular may involve independent $\mu_{B,S}$ and/or $\nu_{B,S}$ variations, as described in section 4.1. Here $\tilde{B}_i^{\mathrm{pert}}$ and $\tilde{S}_i^{\mathrm{pert}}$ are defined as the respective leading term of the OPEs in eq. (2.10), and the nonperturbative component of the resummed CS kernel at its (implicit) boundary scale μ_0 in eq. (3.3) is, of course, exactly equivalent to that of the rapidity anomalous dimension in eq. (3.8), see eq. (3.9) below.

3.2 Modeling the CS kernel

We consider the following simple nonperturbative model for the quark rapidity anomalous dimension, i.e., the CS kernel in the fundamental representation,

$$
\gamma_\zeta^{q,\mathrm{np}}(b_T) = \frac{1}{2}\gamma_{\nu\,\mathrm{np}}^q(b_T) = c_\nu^q \tanh\left(\frac{\omega_{\nu,q}^2}{|c_\nu|}b_T^2\right) = \mathrm{sgn}(c_\nu^q)\,\omega_{\nu,q}^2 b_T^2 + \mathcal{O}(\Lambda_{\mathrm{QCD}}^6 b_T^6), \tag{3.9}
$$

defined with respect to our preferred Landau-pole prescription in eqs. (2.34a) and (2.35). The above two-parameter model is useful for two reasons. First, it asymptotes to a constant c_ν as $b_T \to \infty$, so the total CS kernel also becomes flat (up to logarithmic terms) in the large-b_T limit, as suggested in ref. [162].[11] The absence of at least linear power-law growth has in the meantime also been confirmed by first-principles calculations on the lattice [163–167], and we will give an illustrative range over which our model parameters are varied based on the spread of these lattice results in section 4.2. In addition, the most recent global TMD fits [45, 50, 51, 168] also point to a functional form of this kind. (However, since these fits use LHC Drell-Yan data, we cannot include them in an a priori estimate of the nonperturbative impact.) Second, the sign of the whole model and the height of the plateau at large b_T are controlled through c_ν in a way independent of the ω_ν parameter that governs the strength of the quadratic term and thus the onset of nonperturbative physics. For ease of illustrating the impact of variations around it, we take

$$
(c_\nu^i, \omega_{\nu,q}) = (-0.05, 0.25\,\mathrm{GeV}) \tag{3.10}
$$

as our default values used in all our numerical results unless otherwise noted.

---

[11]We note that these potentially large logarithms of $\mu_0^{\min} b_T$ as $b_T \to \infty$ from having $\mu_0 \to \mu_0^{\min}$ in our "local" Landau-pole prescription, like the renormalons of the TMD ingredients, are another possible source of unstable behavior as the perturbative logarithmic order increases. While we find no drastic lack of convergence (again *a posteriori*) even at very small q_T, removing these terms explicitly provides one way of improving the stability of the fit between different orders when model parameters are extracted from data, which we plan to address in the future.

3.3 Effective rapidity-dependent models for multi-differential Drell-Yan

We first consider the impact of nonperturbative TMD physics on a generic multi-differential Drell-Yan measurement, which can be expressed in terms of their contributions to the helicity cross sections $i = -1, 4$ that factorize in terms of leading-power unpolarized TMD PDFs as in eq. (2.7). We may rewrite the latter as

$$\frac{\mathrm{d}\sigma_i}{\mathrm{d}^4 q} = \frac{1}{2\pi} \int_0^\infty \mathrm{d}b_T \, b_T \, J_0(b_T q_T) \sum_{a,b} \tilde{\sigma}_{i,ab}^{\mathrm{pert+np}\zeta}(Q,Y,b_T) \, \tilde{f}_a^{\mathrm{np}}(x_a, b_T) \, \tilde{f}_b^{\mathrm{np}}(x_b, b_T), \qquad (3.11)$$

where the nonperturbative TMD boundary conditions are weighted by a function

$$\tilde{\sigma}_{i,ab}^{\mathrm{pert+np}\zeta}(Q,Y,b_T) \equiv \frac{1}{2E_{\mathrm{cm}}^2} \sum_{V,V'} L_{\pm(i)VV'}(Q^2) \, H_{iVV'ab}(Q^2, \mu)$$
$$\times \tilde{f}_a^{\mathrm{pert+np}\zeta}(x_a, b_T, \mu, Q^2) \, \tilde{f}_b^{\mathrm{pert+np}\zeta}(x_b, b_T, \mu, Q^2) \qquad (3.12)$$

that contains the electroweak couplings, hard functions, and all other parts of the evolved TMD PDFs, i.e., all its perturbative components and the nonperturbative CS evolution as in eq. (3.5). Note that this weight function (like the definitions derived from it below) also depend on the collider beams and center-of-mass energy E_{cm} as well as the type of boson (Z/γ^*, W^+, or W^-), all of which we suppress in the following. We now simply let

$$\overline{F}_i^{\mathrm{np}}(Q,Y,b_T) \equiv \frac{\sum_{a,b} \tilde{\sigma}_{i,ab}^{\mathrm{pert+np}\zeta}(Q,Y,b_T) \, \tilde{f}_a^{\mathrm{np}}(x_a, b_T) \, \tilde{f}_b^{\mathrm{np}}(x_b, b_T)}{\sum_{a,b} \tilde{\sigma}_{i,ab}^{\mathrm{pert+np}\zeta}(Q,Y,b_T)} \qquad (3.13)$$

which satisfies $\overline{F}_i^{\mathrm{np}}(Q,Y,b_T) = 1 + \mathcal{O}(\Lambda_{\mathrm{QCD}}^2 b_T^2)$ by construction. Note that $i = -1, 4$ in this case labels helicity cross sections, not parton species $u, d, \bar{u}, \dots$ as in the TMD PDF nonperturbative function in eq. (3.1). Inserting eq. (3.13) into eq. (3.11), we have

$$\frac{\mathrm{d}\sigma_i}{\mathrm{d}^4 q} = \frac{1}{2\pi} \int_0^\infty \mathrm{d}b_T \, b_T \, J_0(b_T q_T) \left[\sum_{a,b} \tilde{\sigma}_{i,ab}^{\mathrm{pert+np}\zeta}(Q,Y,b_T) \right] \overline{F}_i^{\mathrm{np}}(Q,Y,b_T). \qquad (3.14)$$

This is precisely in the spirit of ref. [152], where an approach was proposed to extract effective, flavor-averaged nonperturbative parameters at $\mathcal{O}(\Lambda_{\mathrm{QCD}}^2 b_T^2)$, but generalized to all powers in Λ_{QCD}. Specifically, the — in general complicated — flavor and x dependence of the underlying TMD PDFs is transformed into effective, flavor-averaged model functions that are both minimal and sufficient to describe the nonperturbative TMD physics contained in a given process at a given collider, as relevant when using one process at a time to e.g. extract fundamental parameters like $\alpha_s(m_Z)$ or m_W.

The above result can be simplified further for resonant Drell-Yan (integrated over Q) by noting that the weight factor in eq. (3.14) is strongly dominated by $Q \sim m_V$, with $m_V = m_Z$ or m_W, whereas the resonant enhancement cancels in eq. (3.13), leaving behind only the slowly varying x and logarithmic Q dependence of the resummed perturbative TMD PDFs. It is then reasonable to approximate

$$\overline{F}_i^{\mathrm{np}}(Q,Y,b_T) \approx \overline{F}_i^{\mathrm{np}}(m_V, Y, b_T) \equiv \overline{F}_i^{\mathrm{np}}(Y, b_T) \qquad (3.15)$$

by a simpler, two-dimensional function of just Y and b_T. We stress that cross terms between the finite vector boson width and the nonperturbative TMD boundary conditions encoded in $\overline{F}_i^{\mathrm{np}}(Y, b_T)$ are in fact retained and treated exactly in our numerics, i.e., the width is kept exact in $\tilde{\sigma}_{i,ab}^{\mathrm{pert+np}_\zeta}$ in our final eq. (3.19). The above manipulations using the narrow width thus only limit the degree to which our model predictions *deviate from the most general form* of nonperturbative dynamics allowed by TMD factorization (similar to the impact of picking any given functional form for the model), with the residual model dependence starting at $\mathcal{O}[(\Lambda_{\mathrm{QCD}}^2 \Gamma_V)/(q_T^2 m_V)]$ in this case.

Fixing $Q = m_V$ also simplifies the averaging procedure, since in this case the perturbative μ evolution and the (non)perturbative CS evolution cancel exactly between numerator and denominator,

$$\overline{F}_i^{\mathrm{np}}(Y, b_T) = \frac{\sum_{a,b} \tilde{\sigma}_{i,ab}^{\mathrm{pert}}(m_Z, Y, b_T)\, \tilde{f}_a(x_a, b_T, \mu, Q^2)\, \tilde{f}_b(x_b, b_T, \mu, Q^2)}{\sum_{a,b} \tilde{\sigma}_{i,ab}^{\mathrm{pert}}(m_Z, Y, b_T)} \tag{3.16}$$

i.e., the nonperturbative model for γ_ζ^q decouples from the averaging procedure, allowing us to drop the superscript np_ζ. If we further ignore the numerically tiny effect of singlet hard Wilson coefficients, see section 2.3, the higher-order corrections to the hard function also cancel, leaving behind the simple formula

$$\overline{F}_i^{\mathrm{np}}(Y, b_T) = \frac{\sum_{a,b} \sigma_{i,ab}^B(m_Z)\, \tilde{f}_a^{\mathrm{pert}}\, \tilde{f}_b^{\mathrm{pert}}\, \tilde{f}_a^{\mathrm{np}}(x_a, b_T)\, \tilde{f}_b^{\mathrm{np}}(x_b, b_T)}{\sum_{a,b} \sigma_{i,ab}^B(m_Z)\, \tilde{f}_a^{\mathrm{pert}}\, \tilde{f}_b^{\mathrm{pert}}} \, , \tag{3.17}$$

where

$$\sigma_{i,ab}^B(Q) \equiv \frac{1}{2Q^2} \sum_{V,V'} L_{\pm(i)VV'}(Q^2)\, H_{iVV' ab}^{\mathrm{LO}} \tag{3.18}$$

is the Born cross section in the given helicity channel, containing the quark and lepton electroweak charges (see appendix A in ref. [22]), and the perturbative TMD PDFs are evaluated at $x_{a,b}, b_T, \mu_{\mathrm{init}}, \zeta_{\mathrm{init}}$ with $x_{a,b} = m_Z/E_{\mathrm{cm}}\, e^{\pm Y}$. To low perturbative accuracy one may even approximate $\tilde{f}_i(x, b_T, \mu_{\mathrm{init}}, \zeta_{\mathrm{init}})$ by a collinear PDF $f_i(x, \mu_{\mathrm{init}})$, yielding a very simple pocket formula that can be evaluated quickly to convert between effective and general nonperturbative models.

Based on the above discussion, our final, recommended nonperturbative TMD model for multi-differential resonant Drell-Yan studies reads

$$\frac{\mathrm{d}\sigma_i}{\mathrm{d}^4 q} = \frac{1}{2\pi} \int_0^\infty \mathrm{d}b_T\, b_T\, J_0(b_T q_T) \left[\sum_{a,b} \tilde{\sigma}_{i,ab}^{\mathrm{pert+np}_\zeta}(Q, Y, b_T) \right] \overline{F}_i^{\mathrm{np}}(Y, b_T) \, , \tag{3.19}$$

where $\tilde{\sigma}_{i,ab}^{\mathrm{pert+np}_\zeta}$ includes the contribution from the nonperturbative Collins-Soper kernel modeled e.g. as in eq. (3.9). We stress that for Z boson production, the $\overline{F}_i^{\mathrm{np}}(Y, b_T)$ for $i = -1, 4$ (i.e., the inclusive cross section and the forward-backward asymmetry) will in general differ from each other due to the different ways flavors are weighted with electroweak charges. Nevertheless, the two functions exactly coincide for W^+ and W^- production due to the $V - A$ structure of the weak current, leading to a large degree of universality. (Note

that the effective model functions for each of W^+ and W^- are not equal to each other in general due to e.g. a different u vs. d valence TMD PDF contributing to each). To predict their degree of correlation, or their correlation(s) across different colliders and bosons, one necessarily has to resort to a more complete model of the TMD PDF boundary condition and perform the conversion using eq. (3.17).[12]

On the other hand, based on the argument above, we find that one can make $\overline{F}_i^{\rm np}(Y, b_T)$ the primary target of the TMD nonperturbative modelling effort when considering multi-differential Drell-Yan distributions for one boson at a time, with the understanding that they are defined with respect to a definite choice of boundary scales, just like the underlying flavor and x-dependent model would be. For definiteness, one may pick the following flexible model,

$$\overline{F}_i^{\rm np}(Y, b_T) = \left[1 + \overline{\Lambda}_{i,2}(Y)\, b_T^2\right]^2 \exp\left[-2\overline{\Lambda}_{i,4}(Y)\, b_T^4\right] \tag{3.20}$$

with power expansion

$$\overline{F}_i^{\rm np}(Y, b_T) = 1 + \overline{\Lambda}_{i,2}(Y)\, b_T^2 + \left[\overline{\Lambda}_{i,2}^2(Y) - \overline{\Lambda}_{i,4}(Y)\right]b_T^4 + \mathcal{O}(\Lambda_{\rm QCD}^6 b_T^6)\,, \tag{3.21}$$

where the coefficient of the quadratic term $\overline{\Lambda}_{i,2}(Y) \sim \Lambda_{\rm QCD}^2$ may take either sign as long as $\overline{\Lambda}_{i,4}(Y) \sim \Lambda_{\rm QCD}^4$ is positive. The functions $\overline{\Lambda}_{i,n}(Y)$ must be even functions of Y for pp collisions and may, again for definiteness, be chosen as

$$\overline{\Lambda}_{i,n}(Y) = \Lambda_{i,n} + \Delta\Lambda_{i,n}\, Y^2\,. \tag{3.22}$$

We stress that the parameters of the model upon expansion have a direct field-theoretic interpretation in terms of (averaged and normalized) entries in the OPE of the TMD PDFs, accounting for the effect of the Landau-pole prescription starting at $\mathcal{O}(\Lambda_{\rm QCD}^4 b_T^4)$. Since the

---

[12]We note that in principle, the result in eq. (3.19) for the case of the $i = 2$ helicity cross section of the Z boson should be extended by another effective function of Y and b_T starting at $\mathcal{O}(\Lambda_{\rm QCD}^2 b_T^2)$ that encodes the flavor-weighted contribution from the product of two Boer-Mulders functions, possibly supplemented by their known twist-3 matching [169]. (The Double Boer-Mulders (DBM) contribution is suppressed by the width and/or the size of singlet contributions for $i = 5$ in the Z case, and vanishes altogether for $i = 2, 5$ in the case of $W^\pm$ due to the $V - A$ structure of the current [170, 171], such that none of this affects direct m_W measurements that do not rely on tuning to the Z.) As shown in ref. [22], this DBM contribution can in fact become leading in general multi-differential Drell-Yan studies when leptonic observables p_L approach $p_L \sim q_T \sim \Lambda_{\rm QCD}$. Examples with nonzero DBM contributions in this regime analyzed in ref. [22] are $p_L = \phi_\eta^* Q$ and, indeed, the distance $p_L = Q - 2p_T^\ell$ to the Jacobian peak in the p_T^ℓ spectrum as relevant for m_W-like m_Z measurements.

At this point we like to remark that our statements in this section about the *dimensionality* of the effective function space are actually unaffected by the presence of the DBM effect because the approximate leptonic tensors for $p_L \sim q_T \ll Q$ in ref. [22] can be recast as effective integral functionals acting directly on the b_T space integrand upon performing the q_T integral, following the approach of ref. [172], which in turn preserve the power counting of terms of $\mathcal{O}(\Lambda_{\rm QCD}^n b_T^n)$ as $\mathcal{O}(\Lambda_{\rm QCD}^n/p_L^n)$. Thus one still only requires one nonperturbative function of Y to describe the total net nonperturbative effect at each power in $\Lambda_{\rm QCD}^2/p_L^2$, and a single number if no rapidity-differential information (η_ℓ or Y) is retained. Details on this point will be given elsewhere.

Finally, we note that introducing an explicit DBM model function, just like decorrelating the nonperturbative models between $i = -1$ and $i = 4$ for the Z, is not easy to reconcile with the commonly chosen approach in m_W measurements, where the angular coefficients (as *ratios* of helicity cross sections) are evaluated at fixed order, and would first require introducing dedicated resummed components into the description of at least the leading-power helicity cross sections $i = -1, 2, 4$ (and $i = 5$ for full generality).

x dependence of the collinear twist-2 PDFs has been divided out, we generally expect a slowly varying Y dependence and thus no need to include terms of $\mathcal{O}(Y^4)$ or choose a more complicated functional form for the rapidity dependence.

3.4 Effective models for fiducial q_T spectra

We can take the averaging procedure further by also including the rapidity integral in it, as relevant for the single-differential fiducial q_T spectra that are the main focus of this paper. To do so, it is necessary to also consider the action of fiducial cuts Θ, since they shape the contributing rapidity region in this case. Up to corrections of $\mathcal{O}[\Lambda_{\mathrm{QCD}}^2/(q_T Q)]$, which are small for q_T spectra in resonant Drell-Yan production, we may simply ignore the q_T dependence of the leptonic tensors when acting on the nonperturbative model, i.e., we evaluate $L_{i\,VV'}(q,\Theta)$ in eq. (2.6) at $q_T = 0$. This results in a formula similar to eq. (3.19),

$$
\frac{1}{\pi q_T} \frac{\mathrm{d}\sigma^{\mathrm{LP}}(\Theta)}{\mathrm{d}q_T}
$$
$$
= \frac{1}{2\pi} \int_0^\infty \mathrm{d}b_T \, b_T \, J_0(b_T q_T) \left[\sum_{a,b} \int \mathrm{d}Q^2 \, \mathrm{d}Y \, \tilde{\sigma}_{ab}^{\mathrm{LP,pert+np}\zeta}(Q,Y,\Theta,b_T) \right] \overline{F}^{\mathrm{np}}(\Theta,b_T) \,, \tag{3.23}
$$

where the leading-power fiducial perturbative cross section in b_T space is defined as

$$
\tilde{\sigma}_{ab}^{\mathrm{LP,pert+np}\zeta}(Q,Y,\Theta,b_T) = \frac{3}{8} \sum_{i=-1,4} \tilde{\sigma}_{i,ab}^{\mathrm{pert+np}\zeta}(Q,Y,b_T) \int_{-1}^{1} \mathrm{d}\cos\theta \, g_i(\theta) \, \hat{\Theta}^{\mathrm{LP}}(Q,Y,\theta) \,, \tag{3.24}
$$

with $\hat{\Theta}^{\mathrm{LP}}(Q,Y,\theta)$ the acceptance function $\hat{\Theta}(q,\theta,\varphi)$ of the fiducial cuts Θ evaluated for $q_T = 0$, which implies that the φ dependence also drops out [22]. The corresponding averaged (effective) nonperturbative model is given by

$$
\overline{F}^{\mathrm{np}}(\Theta,b_T) = \frac{\sum_{a,b} \int \mathrm{d}Y \, \sigma_{ab}^B(m_V,Y,\Theta) \, \tilde{f}_a^{\mathrm{pert}} \, \tilde{f}_b^{\mathrm{pert}} \, \tilde{f}_a^{\mathrm{np}}(x_a,b_T) \, \tilde{f}_b^{\mathrm{np}}(x_b,b_T)}{\sum_{a,b} \int \mathrm{d}Y \, \sigma_{ab}^B(m_V,Y,\Theta) \, \tilde{f}_a^{\mathrm{pert}} \, \tilde{f}_b^{\mathrm{pert}}} \tag{3.25}
$$

where the fiducial Born cross section is defined in terms of eq. (3.18) as

$$
\sigma_{ab}^B(Q,Y,\Theta) = \frac{3}{8} \sum_{i=-1,4} \sigma_{i,ab}^B(Q) \int_{-1}^{1} \mathrm{d}\cos\theta \, g_i(\theta) \, \hat{\Theta}^{\mathrm{LP}}(Q,Y,\theta) \,, \tag{3.26}
$$

the perturbative TMD PDFs are again evaluated at $x_{a,b}, b_T, \mu_{\mathrm{init}}, \zeta_{\mathrm{init}}$, and we have made use of $Q \approx m_V$ as before such that the (non)perturbative CS evolution, hard functions, and μ evolution drop out.

Our final predictions for the resummed contribution to fiducial q_T spectra are then obtained by inserting this model back as an overall common factor to all factorized helicity cross sections into the factorization formula with exact leptonic kinematics,

$$
\frac{1}{\pi q_T} \frac{\mathrm{d}\sigma_{\mathrm{res}}(\Theta)}{\mathrm{d}q_T} = \frac{1}{4E_{\mathrm{cm}}^2} \int \mathrm{d}Q^2 \, \mathrm{d}Y \sum_{i=-1,4} \sum_{V,V'} L_{i\,VV'}(q,\Theta) \frac{1}{2\pi} \int_0^\infty \mathrm{d}b_T \, b_T J_0(b_T q_T)
$$
$$
\times \left[\sum_{a,b} H_{i\,VV'\,ab}(Q^2,\mu) \, \tilde{f}_a^{\mathrm{pert+np}\zeta}(x_a,b_T,\mu,Q^2) \, \tilde{f}_b^{\mathrm{pert+np}\zeta}(x_b,b_T,\mu,Q^2) \right]
$$
$$
\times \overline{F}^{\mathrm{np}}(\Theta,b_T) \,, \tag{3.27}
$$

which also follows e.g. from eqs. (3.19), (3.20) and (3.22) by setting $\Lambda_{-1,n} = \Lambda_{4,n}$ and $\Delta\Lambda_{-1,n} = 0$, i.e., dropping the Y dependence. We stress that as for the narrow-width approximation already used above, cross terms of $\mathcal{O}[\Lambda_{\rm QCD}^2/(q_T Q)]$ between nonperturbative and linear fiducial power corrections are indeed retained exactly in our final predictions through the exact kinematic dependence of $L_{iVV'}(q,\Theta)$, and it is only the degree of model (in)dependence that is qualified by the approximations we make. In particular, the final formula in eq. (3.27) still retains all the exact linear power corrections dressing the perturbative resummation.

In order to illustrate the effect of the nonperturbative TMD boundary condition on the predictions at the highest perturbative orders that we present in this paper, we make the following, simple Gaussian choice for the model function,

$$\overline{F}^{\rm np}(\Theta, b_T) = \exp(-2\Omega_V b_T) = 1 - 2\Omega_V^2 b_T^2 + 2\Omega_V^4 b_T^4 + \mathcal{O}(\Lambda_{\rm QCD}^6 b_T^6)\,, \qquad (3.28)$$

and we include a subscript $V = Z, W^+, W^-$ to remind the reader that the parameter is decorrelated between bosons (and their associated fiducial phase-space volumes Θ). We note that while this is numerically equivalent to assuming a common Gaussian width Ω_V for all quark and antiquark flavors, it is much more rigorously justified through our effective model approach, where the existence of the model is well-defined, minimal, and sufficient, and only in a second step does one pick a specific form for it. Again, in order to be able to easily showcase the impact of variations around it, we will take

$$\Omega_V = 0.5\,{\rm GeV} \qquad (3.29)$$

as our default central value.

Discussion. Eqs. (3.19) and (3.27) make precise the intuitive notion that a one-dimensional q_T (two-dimensional Y and q_T) spectrum contains only information about a single effective one-dimensional (two-dimensional) nonperturbative model function of b_T (Y and b_T), independent of the underlying complexity of the flavor and x-dependent TMD PDF nonperturbative boundary conditions. In particular, upon expansion in $\Lambda_{\rm QCD} b_T$ (or $\Lambda_{\rm QCD}/q_T$), the results imply that only a single number (or a single one-dimensional function of Y) is required in addition to the first correction to the CS kernel in order to completely describe the leading nonperturbative effect. Eq. (3.25) generalizes the formula derived in ref. [152] for the effective parameter $\overline{\Lambda}^{(2)}$ appearing in the $\mathcal{O}(\Lambda_{\rm QCD}^2/q_T^2)$ term in the fiducial spectrum to all powers in $\Lambda_{\rm QCD}$.[13] (As a downside of extending to all powers in $\Lambda_{\rm QCD}$, the manifestly linear impact of the leading nonperturbative term in ref. [152] is lost, and dedicated numerics like in this paper are required to obtain fit templates for each set of parameters describing $\overline{F}^{\rm np}$.) Conversely, no additional information about the underlying TMD nonperturbative structure beyond $\overline{F}_i^{\rm np}(Y, b_T)$ or $\overline{F}^{\rm np}(\Theta, b_T)$ can be extracted from resonant Drell-Yan spectra. This formally explains the observations of ref. [51], which found that the combination of Drell-Yan and semi-inclusive deep-inelastic scattering data for different hadron species was crucial to achieve flavor separation of the TMDs. Of course, in the context of a global, flavor-dependent TMD

---

[13]Note that eq. (4.11) in ref. [152] misses a factor of 2 in the denominator.
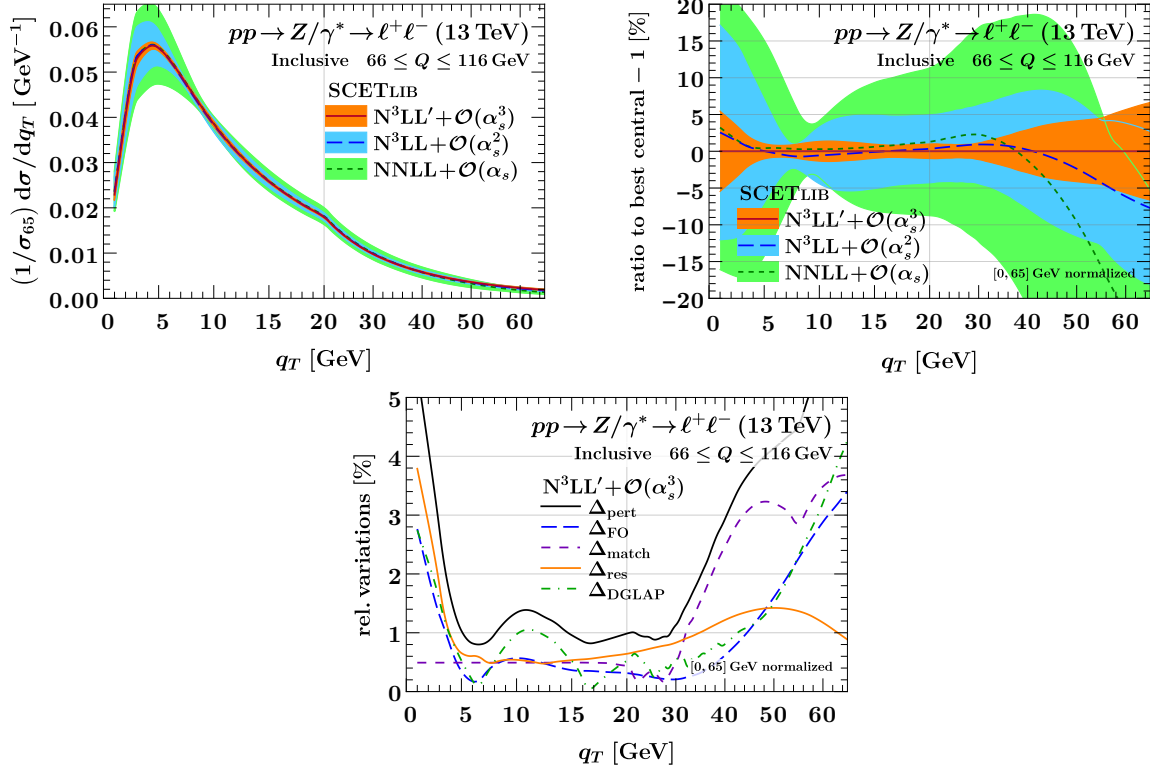
Figure 5. Predictions for the normalized inclusive p_T^Z spectrum at the 13 TeV LHC (top left), its relative difference to the highest-order prediction (top right), and the complete perturbative uncertainty breakdown of the $N^3LL' + \mathcal{O}(\alpha_s^3)$ result in terms of each contributing source (bottom).

	NNLL+$\mathcal{O}(\alpha_s)$	N^3LL+$\mathcal{O}(\alpha_s^2)$	N^3LL' + $\mathcal{O}(\alpha_s^3)$
σ_{65} [pb]	1813.5	1806.9	1787.3

Table 1. Normalization factors for the inclusive p_T^Z spectra with `MSHT20nnlo` shown in figure 5.

		NNLL+$\mathcal{O}(\alpha_s)$	N^3LL+$\mathcal{O}(\alpha_s^2)$	N^3LL' + $\mathcal{O}(\alpha_s^3)$
σ_{65} [pb]	ATLAS cuts [5]	682.1	682.6	673.4
	CMS cuts [11]	673.1	673.9	664.9

Table 2. Normalization factors for the fiducial p_T^Z spectra with `MSHT20nnlo` shown in figure 6.

fit or if a more granular model is desired and e.g. explicit flavor ratios are known from the lattice, one can always revert to instead using the product $\tilde{f}_a^{\mathrm{np}}(x_a, b_T)\, \tilde{f}_b^{\mathrm{np}}(x_b, b_T)$ on the last line of eq. (3.27) and pulling it back under the flavor sums and (Q, Y) integral.

4 Results for the inclusive and fiducial p_T^Z spectrum

In figure 5 and 6 we present our predictions for the inclusive and fiducial Z-boson transverse-momentum spectrum at different orders in resummed and matched perturbation theory up
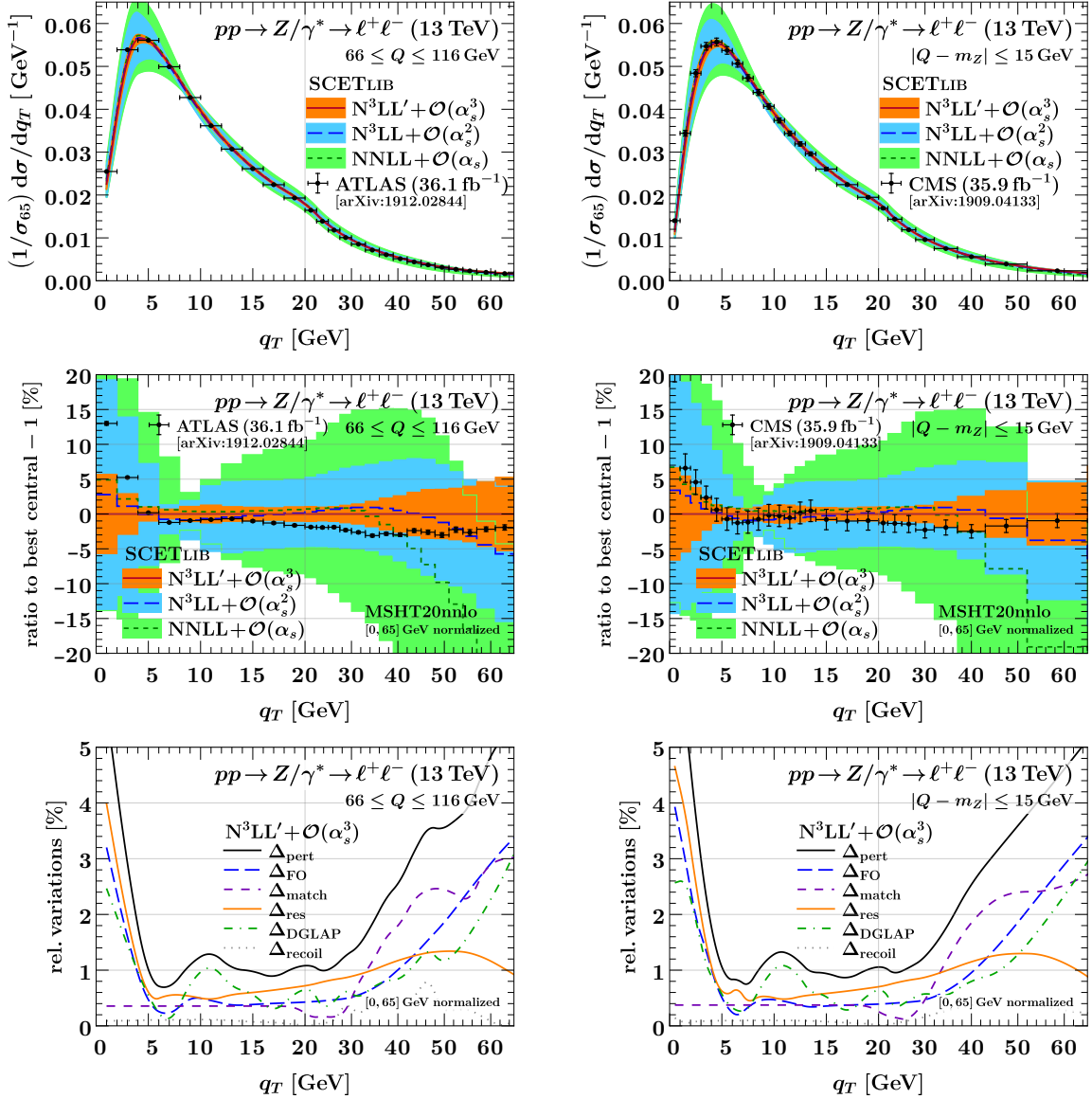
Figure 6. Predictions for the normalized fiducial p_T^Z spectrum at the 13 TeV LHC (top row), its relative difference to the highest-order prediction (middle row), and the complete perturbative uncertainty breakdown of the $N^3LL' + \mathcal{O}(\alpha_s^3)$ result in terms of each contributing source (bottom row). In the left (right) column, we compare to the ATLAS 13 TeV [5] (CMS 13 TeV [11]) measurement, using the respective set of fiducial cuts.

to $N^3LL' + \mathcal{O}(\alpha_s^3)$. We use the MSHT20nnlo PDF set [147] as our default with the attendant value of $\alpha_s(m_Z) = 0.118$. We consider two sets of fiducial cuts on the dilepton pair, as used in the ATLAS [5] and CMS [11] 13 TeV measurements, respectively,

$$
\begin{aligned}
\text{ATLAS cuts:} \qquad & p_T^\ell > 27\,\text{GeV}\,, \qquad |\eta_\ell| < 2.5 \\
\text{CMS cuts:} \qquad & p_T^\ell > 25\,\text{GeV}\,, \qquad |\eta_\ell| < 2.4\,,
\end{aligned}
\tag{4.1}
$$

which are applied to both the lepton and the antilepton. For ref. [5], we compare to the result obtained for Born leptons after combining the electron and muon channels. For ref. [11], we compare to the result obtained using dressed leptons, again from a combination of electron and muon channels.[14]

Our electroweak inputs are as follows, see ref. [22] for details,

$$
\begin{aligned}
m_Z &= 91.1535\,\text{GeV}\,, \qquad \Gamma_Z = 2.4943\,\text{GeV}\,, \\
m_W &= 80.3580\,\text{GeV}\,, \qquad \Gamma_W = 2.0843\,\text{GeV}\,, \\
G_F &= 1.1663787 \times 10^{-5}\,\text{GeV}^{-2}\,,
\end{aligned}
\tag{4.2}
$$

$$
V_{\text{CKM}} = \begin{pmatrix} V_{ud} & V_{us} & V_{ub} \\ V_{cd} & V_{cs} & V_{cb} \\ V_{td} & V_{ts} & V_{tb} \end{pmatrix} = \begin{pmatrix} 0.97446 & 0.22452 & 0.00365 \\ 0.22438 & 0.97359 & 0.04214 \\ 0.00896 & 0.04133 & 0.999105 \end{pmatrix}\,,
$$

$$
\sin^2\theta_w = 0.22284\,, \qquad \alpha_{\text{em}} = \frac{1}{132.357}\,.
\tag{4.3}
$$

The numerical treatment of the oscillatory Bessel integral and our semi-analytic evaluation of the leptonic phase-space integrals are also described in section (4.1) of ref. [22].

To easily study the uncertainties in the p_T^Z spectrum and compare to the (most often normalized) experimental data, we find it convenient to normalize the spectrum on the range $0 \leq q_T \leq 65\,\text{GeV}$,[15] where we empirically found that nonsingular contributions are small. For reference, the total integrals of our predictions as used for the normalization, which we denote by σ_{65}, are reported in tables 1 and 2. From the data comparisons in figure 6 we observe that our predictions with the default PDF set and default nonperturbative parameters closely track the fiducial ATLAS [5] and CMS [11] data over a wide range of q_T, but residual differences are well visible. In the following subsections, we assess the impact of various sources of uncertainties and different physical effects on our predictions.

4.1 Scale variations, convergence, and estimated matching uncertainties

Predictions in either fixed-order or resummation-improved perturbation theory are necessarily subject to an uncertainty from missing higher-order terms. A commonly used approach to assess these is to vary the scales at which various objects appearing in the prediction are renormalized. Since the dependence on any individual scale is beyond the working order in a factorized cross section, these variations can indicate the typical size of missing higher-order terms. While they do not offer any handle on the correlations between perturbative uncertainties e.g. between different bins, scale variations nevertheless can serve, and are heavily used, as a crude estimate of the truncation uncertainty based on the available lower-order data. For this reason, we do present estimates of the perturbative uncertainty within the scale variation paradigm in this section. (For an alternative that overcomes all

---

[14]We note that at least as of `version 2`, the `HEPData` entry for ref. [11] had an incorrect total integral ($\neq 1$) for the normalized p_T^Z spectrum, while relative uncertainties in each bin were correct. The correct result is obtained by dividing by the total integral once more. We thank Aram Apyan for help with this issue.

[15]Experimental data are re-normalized on this range by dividing by the central value of the norm and maintaining the relative uncertainties in each bin. We ignore possible correlations between individual bins and the norm that are negligible compared to the original relative uncertainties in each (narrow) bin.

the shortcomings, see refs. [173, 174].) To do so in the most reliable and granular fashion possible within the conventional paradigm, we refine the profile scale variation setup of ref. [22], which in turn was based on ref. [175]. We here give a self-contained description of the profile scale variations we perform, commenting on the improvements and differences to ref. [22] along the way. The profile scales and variations originally designed in the course of preparing the present manuscript have recently been applied already in ref. [176], where the ability to separately freeze out the PDF scale μ_f proved particularly useful for heavy flavor-induced processes like $b\bar{b} \to H$.

For the resummed cross section, the task is to vary the central boundary scales given in eq. (2.28) around their central values by (up to) the conventional factor of 2 in all possible ways such that the variations (a) do not induce undue sensitivity to the Landau pole and (b) smoothly transition into a set of conventional fixed-order scale variations in the tail at $q_T \sim Q$. We achieve this task by varying them as

$$\mu_H = \mu_{\mathrm{FO}}^{\mathrm{central}} \, 2^{w_{\mathrm{FO}}} \,,$$

$$\mu_B = \mu_{\mathrm{FO}}^{\mathrm{central}} \, 2^{w_{\mathrm{FO}}} \, f_{\mathrm{vary}}^{v_{\mu_B}} \, f_{\mathrm{run}}\left(\frac{q_T}{Q}, \frac{1}{Q} \mu_*\left(\frac{b_0}{b_T}, \frac{\mu_B^{\mathrm{min}}}{2^{w_{\mathrm{FO}}} \, f_{\mathrm{vary}}^{v_{\mu_B}}} \right) \right) \,,$$

$$\nu_B = \mu_{\mathrm{FO}}^{\mathrm{central}} \, 2^{w_{\mathrm{FO}}} \, f_{\mathrm{vary}}^{v_{\nu_B}} \,,$$

$$\mu_S = \mu_{\mathrm{FO}}^{\mathrm{central}} \, 2^{w_{\mathrm{FO}}} \, f_{\mathrm{vary}}^{v_{\mu_S}} \, f_{\mathrm{run}}\left(\frac{q_T}{Q}, \frac{1}{Q} \mu_*\left(\frac{b_0}{b_T}, \frac{\mu_S^{\mathrm{min}}}{2^{w_{\mathrm{FO}}} \, f_{\mathrm{vary}}^{v_{\mu_S}}} \right) \right) \,,$$

$$\nu_S = \mu_{\mathrm{FO}}^{\mathrm{central}} \, 2^{w_{\mathrm{FO}}} \, f_{\mathrm{vary}}^{v_{\nu_S}} \, f_{\mathrm{run}}\left(\frac{q_T}{Q}, \frac{1}{Q} \mu_*\left(\frac{b_0}{b_T}, \frac{\nu_S^{\mathrm{min}}}{2^{w_{\mathrm{FO}}} \, f_{\mathrm{vary}}^{v_{\nu_S}}} \right) \right) \,,$$

$$\mu_f = \mu_F^{\mathrm{central}} \, 2^{v_{\mu_f}} \, f_{\mathrm{run}}\left(\frac{q_T}{Q}, \frac{1}{Q} \mu_*\left(\frac{b_0}{b_T}, \frac{\mu_f^{\mathrm{min}}}{2^{v_{\mu_f}}} \right) \right) \,, \tag{4.4}$$

where $\mu_{\mathrm{FO}}^{\mathrm{central}} = \mu_F^{\mathrm{central}} = Q$ are the central fixed-order renormalization and factorization scales. The central scales are recovered for

$$v_{\mu_B} = v_{\nu_B} = v_{\mu_S} = v_{\nu_S} = w_{\mathrm{FO}} = v_{\mu_f} = 0 \,. \tag{4.5}$$

The boundary scale μ_0 of the rapidity anomalous dimension is held fixed at its central value since its variations would be double counted with the explicit $\nu_{B,S}$ variations [175]. Here $f_{\mathrm{vary}} \equiv f_{\mathrm{vary}}(q_T/Q)$ governs the strength of those variations that must turn off as $q_T/Q \to 1$, $f_{\mathrm{vary}} \to 1$, where we choose

$$f_{\mathrm{vary}}(x) = \begin{cases} 2(1 - x^2/x_3^2) \,, & 0 \le x < x_3/2 \,, \\ 1 + 2(1 - x/x_3)^2 \,, & x_3/2 \le x < x_3 \,, \\ 1 \,, & x_3 \le x \,. \end{cases} \tag{4.6}$$

For $q_T \ge x_3 Q$, the above variations thus all reduce to

$$\mu_B = \nu_B = \mu_S = \nu_S = \mu_{\mathrm{FO}}^{\mathrm{central}} \, 2^{w_{\mathrm{FO}}} \,, \qquad \mu_f = \mu_F^{\mathrm{central}} \, 2^{v_{\mu_f}} \,, \tag{4.7}$$

which exactly matches the variations we perform on the renormalization and factorization scale in the nonsingular cross section (and thus on the whole prediction in the far tail),

$$\mu_R = \mu_{\mathrm{FO}}^{\mathrm{central}} \, 2^{w_{\mathrm{FO}}} \,, \qquad \mu_F = \mu_F^{\mathrm{central}} \, 2^{v_{\mu_f}} \,. \tag{4.8}$$

We note the appearance of factors like $2^{w_{\rm FO}}$, $2^{v_{\mu_f}}$, or $f_{\rm vary}^{v_{\mu_X}}$ in the argument of the μ_* functions in eq. (4.4). These ensure that scale variations are also frozen out at long distances as $b_T \to 1/\Lambda_{\rm QCD}$, which in turns ensures that no scales $\lesssim 1\,{\rm GeV}$ are probed by the variations, see the bands in the left panel of figure 4. Like the addition of the minimum scales implemented through the μ_* functions themselves, this change compared to ref. [22] is necessary because unlike ref. [22] (which simply froze out the coupling and PDFs), we aim to maintain a straight-forward OPE interpretation of the nonperturbative functions we introduced in section 3.

We now describe how the above variation flags are grouped into subsets of joint and individual variations that each estimate a distinct source of uncertainty, as shown in the bottom rows of figure 5 and 6.

Resummation uncertainty $\Delta_{\rm res}$. A first set of variations concerns those independent scales that emerge in the canonical resummation region $q_T \ll Q$, and estimates the perturbative uncertainty on (mainly) the shape of the resummed Sudakov spectrum. In eq. (4.4), they are controlled by v_{μ_B}, v_{ν_B}, v_{μ_S}, v_{ν_S}, which we vary as

$$
\begin{aligned}
(v_{\mu_B}, v_{\nu_B}, v_{\mu_S}, v_{\nu_S}) \in V_{\rm res} = \{ & (\uparrow,-,-,-),(-,\uparrow,-,-),(-,-,\uparrow,-),(-,-,-,\uparrow), \\
& (-,-,-,\downarrow),(-,-,\downarrow,-),(-,\downarrow,-,-),(\downarrow,-,-,-), \\
& (\uparrow,\uparrow,-,-),(\uparrow,-,\uparrow,-),(\uparrow,-,-,\uparrow),(\uparrow,-,-,\downarrow),(\uparrow,\downarrow,-,-), \\
& (-,\uparrow,\uparrow,-),(-,\uparrow,-,\uparrow),(-,\uparrow,\downarrow,-),(-,-,\uparrow,\uparrow), \\
& (-,-,\downarrow,\downarrow),(-,\downarrow,\uparrow,-),(-,\downarrow,-,\downarrow),(-,\downarrow,\downarrow,-),(\downarrow,-,-,\uparrow), \\
& (\downarrow,-,\downarrow,-),(\downarrow,\downarrow,-,-),(\uparrow,\uparrow,\uparrow,-),(\uparrow,\uparrow,-,\uparrow),(\uparrow,-,\uparrow,\uparrow), \\
& (\uparrow,\downarrow,\uparrow,-),(\uparrow,\downarrow,-,\downarrow),(-,\uparrow,\uparrow,\uparrow),(-,\downarrow,\downarrow,\downarrow),(\downarrow,\uparrow,-,\uparrow), \\
& (\downarrow,\downarrow,-,\downarrow),(\downarrow,\downarrow,\downarrow,-),(\uparrow,\uparrow,\uparrow,\uparrow),(\downarrow,\downarrow,\downarrow,\downarrow) \},
\end{aligned}
\tag{4.9}
$$

where we write $\uparrow$ ($\downarrow$, $-$) for $v = +1$ ($v = -1$, $v = 0$) for brevity. The set of variations in eq. (4.9) is defined by considering all $3^4 - 1 = 80$ possible variations of the four v, and removing all the ones where the argument of a logarithm exponentiated by the renormalization group evolution between terms would be varied by a factor of four [175]. The final uncertainty estimate is obtained by taking the symmetrized envelope of all tuples $\vec{v}$ of variations above,

$$
\Delta_{\rm res} = \max_{\vec{v} \in V_{\rm res}} \left| {\rm d}\sigma_{\vec{v}} - {\rm d}\sigma_{\rm central} \right|.
\tag{4.10}
$$

It has been noted in refs. [22, 175] that while the set of variations in eq. (4.9) appears large, keeping all combinations under the envelope is often important to prevent accidental underestimates when several scale variations at once cross the central value at some point in q_T. For definiteness, we take each individual variation to be fully correlated between each bin and the total integral when normalizing the spectrum. This effect on the total integral is responsible for the nonzero (but subdominant) contribution of $\Delta_{\rm res}$ also at large $q_T \geq 60\,{\rm GeV}$ in figure 5 and 6 where the underlying variations are largely turned off already at the level of the unnormalized spectrum. We note at this point that while eq. (2.7a) with separately finite soft and beam functions can easily be translated into suitably evolved TMD PDFs for central scales, see eq. (3.8), the rapidity renormalization group does provide a larger set of possible nontrivial scale variations, which we here make use of for our estimate of the perturbative uncertainties.

Fixed-order uncertainty Δ_{FO}. A second set of variations, which affects the spectrum everywhere and can be thought of as (mainly) varying its normalization, concerns the overall choice of fixed-order renormalization scale entering in particular the strong coupling,

$$\mu_{\mathrm{FO}} = \mu_{\mathrm{FO}}^{\mathrm{central}}\, 2^{w_{\mathrm{FO}}}\,, \tag{4.11}$$

which we vary as follows, taking the uncertainty estimate to be the symmetrized envelope,

$$w_{\mathrm{FO}} \in V_{\mathrm{FO}} = \{+1, -1\}\,, \qquad \Delta_{\mathrm{FO}} = \max_{w_{\mathrm{FO}} \in V_{\mathrm{FO}}} \left|\mathrm{d}\sigma_{w_{\mathrm{FO}}} - \mathrm{d}\sigma_{\mathrm{central}}\right|. \tag{4.12}$$

Variations of w_{FO}, which we take to be fully correlated when normalizing the spectrum, are consistently propagated into the resummed and nonsingular cross sections through eqs. (4.4) and (4.8), which involve factors of $2^{w_{\mathrm{FO}}}$ in front of all renormalization-like scales. Compared to the most common approaches to estimate the total truncation uncertainty in fixed-order perturbation theory for hadronic processes, we yet have to include an uncertainty component from variations of the *factorization scale*, which we turn to next.

DGLAP (factorization scale) uncertainty Δ_{DGLAP}. While it is challenging in general to identify common underlying sources of uncertainty for different regions of the spectrum, one source can in fact be readily identified as the truncation uncertainty in the DGLAP evolution of the twist-2 collinear PDF that feature as a common ingredient everywhere. To estimate it, we perform a common variation of the scales entering the PDFs everywhere in the prediction as follows,

$$v_{\mu_f} \in V_{\mathrm{DGLAP}} = \{+1, -1\}\,, \qquad \Delta_{\mathrm{DGLAP}} = \max_{v_{\mu_f} \in V_{\mathrm{DGLAP}}} \left|\mathrm{d}\sigma_{v_{\mu_f}} - \mathrm{d}\sigma_{\mathrm{central}}\right|. \tag{4.13}$$

Variations of v_{μ_f}, which we take to be fully correlated when normalizing the spectrum, are again consistently propagated into the resummed and nonsingular cross sections through eqs. (4.4) and (4.8). We recall that in the resummed cross section, only the beam function matching coefficient is evaluated at μ_B, while the underlying PDF is evaluated (in general) at $\mu_f \neq \mu_B$ using our dedicated implementation of eq. (2.12), which precisely induces a set of compensating logarithmic terms in μ_f/μ_B whose difference to the central value probes the residual dependence on μ_f. Note that in contrast to μ_B, whose variations are damped by f_{vary} at large q_T in eq. (4.4), the variations of μ_f stay fully turned on all the way into the tail, as is required to recover a standard μ_F variation of the fixed-order result in that region. Compared to refs. [22, 175], having a dedicated uncertainty component Δ_{DGLAP} is new for a resummed and matched prediction; both references effectively only considered common diagonal variations of μ_{FO} and μ_F^{central}, which then were inherited by the respective $\mu_B = \mu_f$ in the resummed cross section when computing the total Δ_{FO} quoted in those references. We would also like to point out that in our present setup, μ_R and μ_F variations are effectively combined in quadrature in the final perturbative uncertainty estimate also in the fixed-order region, see eq. (4.18). In our case, this choice of separating out Δ_{DGLAP} (rather than moving it under a common envelope) is motivated by the special role of PDF evolution affecting the spectrum everywhere. We point out that the mildly oscillatory behavior of Δ_{DGLAP} in figure 5 and 6 is induced by the discontinuity of the PDF at the m_b threshold, which in turn spreads over the entire q_T range by the inverse b_T-integral with a period of $\Delta q_T \sim m_b$.

Matching uncertainty Δ_{match}. The profile scales that implement the transition from the canonical to the fixed-order region involve three transition points x_i that determine the onset, midpoint, and endpoint of the transition. While the values of these transition points are based on a quantitative assessment of the size of nonsingular terms [22], they are not uniquely determined by this criterion, and the associated uncertainty must be assessed. As in refs. [22, 175], we thus compute a matching uncertainty Δ_{match} as follows,

$$(x_1, x_2, x_3) \in V_{\text{match}} = \{(0.4, 0.75, 1.1), (0.2, 0.45, 0.7), (0.4, 0.55, 0.7), (0.2, 0.65, 1.1)\},$$
$$\Delta_{\text{match}} = \max_{\vec{x} \in V_{\text{match}}} |\sigma_{\vec{x}} - \sigma_{\text{central}}|, \tag{4.14}$$

where we take the variations to be fully correlated when normalizing the spectrum. At the level of the unnormalized spectrum, the matching uncertainty vanishes for $q_T \leq x_1^{\min} Q$ and $q_T \geq x_3^{\max} Q$, where $x_1^{\min}$ and $x_3^{\max}$ are the minimum or maximum value taken by x_1 and x_3, respectively. The 0.5% effect visible at small q_T in the normalized spectra in figure 5 and 6, on the other hand, is precisely due to the residual effect of the matching variations on the total integral, which is not guaranteed to be preserved by either the central x_i or their variations in eq. (4.14). We note that if a symmetric impact of variations entering the matching uncertainty is desired, an alternative scheme is to simply vary the midpoint x_2 of the profile up and down by a suitable amount [176].

Recoil uncertainty Δ_{recoil}. A final contribution to our total perturbative uncertainty estimate is not related to any specific scale choice, but — like the matching uncertainty — still concerns the split between resummed and fixed-order terms.

Specifically, when decomposing the fiducial q_T spectrum (or any observable sensitive to the differential lepton-antilepton distribution) as in eq. (2.6), a choice is made in which frame to decompose the hadronic tensor in terms of helicity cross sections, where subsequently the leading-power ones are resummed to all orders while dressing them with the exact lepton kinematics to ensure the exact treatment of linear or leptonic ("fiducial") power corrections. Making these choices explicit, we compute the resummed and fixed-order singular cross sections using the following formula,

$$\frac{1}{\pi q_T} \frac{d\sigma_X(\Theta)}{dq_T} = \frac{1}{2E_{\text{cm}}^2} \int dQ^2 \, dY \sum_{i=-1,4} \sum_{V,V'} L_{iVV'}^X(q, \Theta) \, W_{iVV'}^{\text{LP},X}(q, P_a, P_b), \tag{4.15}$$

where X, affecting both the leptonic prefactors and the structure functions, indicates the choice of frame, and $X = \text{CS}$ (the Collins-Soper frame) for our central prediction. While these frame choices are subject to the constraint that their z^μ axes coincide with the beam axis as $q_T \to 0$, this does not uniquely specify them, and different choices for the structure function decomposition (i.e., the choice of Z rest frame, i.e., the choice of a specific recoil prescription) differ by moving a set of terms of $\mathcal{O}(q_T^2/Q^2)$ [22] between the leading-power and subleading-power structure functions. This means that as soon as the leading-power resummation is performed, they will differ by whether these terms are resummed to all orders or evaluated at fixed order. In order to assess the potential presence of an ambiguity due to this choice, we here perform — to our knowledge, for the first time — an explicit variation

of the choice of structure function decomposition in a resummed and matched prediction.[16] Specifically, we consider the two extreme cases

$$X \in V_{\text{recoil}} = \{\text{GJ}, \overline{\text{GJ}}\}. \tag{4.16}$$

Here the decomposition is performed in either the Gottfried-Jackson ($X = \text{GJ}$) frame [177], where the z^μ axis is aligned with the hadron incoming along the positive z^μ_{lab} direction, or performed in the "anti-Gottfried Jackson" frame ($X = \overline{\text{GJ}}$) where the opposite hadron is chosen as reference; our default value $X = \text{CS}$ amounts to a certain symmetric choice between the two that has compact covariant expressions [22] and a particularly simple power expansion [171]. The associated uncertainty is then computed by taking the envelope,

$$\Delta_{\text{match}} = \max_{X \in V_{\text{recoil}}} \left| d\sigma_X - d\sigma_{\text{central}} \right|. \tag{4.17}$$

Like e.g. the matching uncertainty, Δ_{recoil} vanishes by construction at the level of the unnormalized spectrum since it amounts to reexpanding certain $\mathcal{O}(q_T^2/Q^2)$ terms. We nevertheless point out that for the normalized fiducial spectra shown in figure 6, its impact instead again tends to a constant as $q_T \to 0$ due to its residual effect on the total matched fiducial cross section. From this observation, we find it interesting to note that this uncertainty on the total fiducial cross section is in fact under excellent control, where we may read off its relative size from the uncertainty breakdown plots in figure 6 at $q_T \to 0$ as roughly a permille.

Combined perturbative uncertainty Δ_{pert}. The final perturbative uncertainty estimate Δ_{pert}, which provides the bands at different orders in the ratio plots in figure 5 and 6 and is indicated by a solid black line in the uncertainty breakdown plots, is computed by adding the uncertainties from all individual sources in quadrature,

$$\Delta_{\text{pert}} = \Delta_{\text{res}} \oplus \Delta_{\text{FO}} \oplus \Delta_{\text{DGLAP}} \oplus \Delta_{\text{match}} \oplus \Delta_{\text{recoil}}. \tag{4.18}$$

As can be seen from the top right panel in figure 5 and the center row of panels in figure 6, where we show ratios of predictions at different orders to the highest order, the resulting uncertainty estimate features excellent perturbative coverage, i.e., higher orders are well contained within the lower-order uncertainty estimates. We note that while the convergence at the level of the central value seems to be more rapid than the uncertainty estimates would allow for, we see no justification for reducing the estimate after the fact.

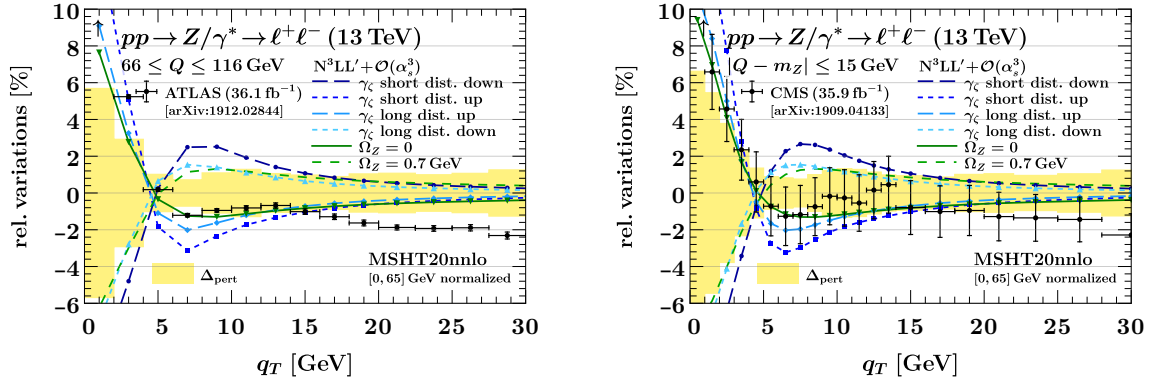## 4.2 Impact of nonperturbative TMD physics

We next consider the impact of the nonperturbative model functions introduced in section 3 on our predictions. We do so by performing illustrative variations of the model parameters to determine which regions in the spectrum are affected by nonperturbative physics, and to which extent. While this already helps to assess whether residual differences to the

---

[16]A distinct issue is how the choice of frame for computing the singular cross section affects the efficiency of differential q_T subtractions, see ref. [22]. The two issues are related because they both hinge on the size of the remaining fixed-order nonsingular, but our study here concerns the potential scheme dependence of fiducial resummation effects that remain present even after taking all technical cutoffs to zero.
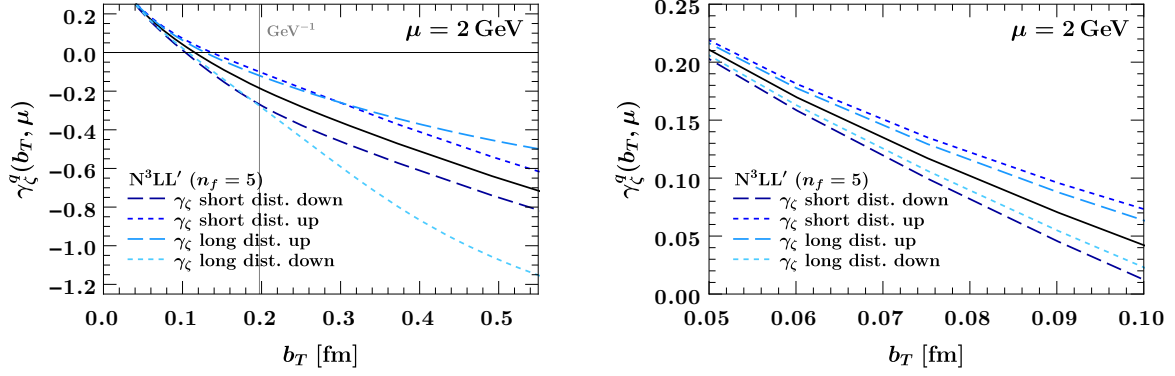
Figure 7. Illustration of the model parameter spread we consider for the Collins-Soper kernel, i.e., the rapidity anomalous dimension. The black solid line indicates our default choice of model parameters. The gray vertical line indicates a distance of $b_T = 1\,\mathrm{GeV}^{-1} \approx 0.197\,\mathrm{fm}$ for reference. The right panel shows a close-up in the small-b_T region.

Figure 8. Impact of parameter variations in the nonperturbative TMD models at $\mathrm{N^3LL'} + \mathcal{O}(\alpha_s^3)$ compared to ATLAS 13 TeV [5] (left) and CMS 13 TeV [11] (right) measurements. For illustration, we also compare to the estimated size Δ_{pert} of the perturbative uncertainty.

data may be of nonperturbative origin, we leave a dedicated fit of the nonperturbative contributions to future work.

We vary the parameters entering the model for the Collins-Soper kernel (i.e., the rapidity anomalous dimension) in eq. (3.9) as follows,

$$
(c_\nu^q, \omega_{\nu,q}) \in \{(-0.15, 0.433\,\mathrm{GeV}), (0.05, 0.25\,\mathrm{GeV}),
$$
$$
(0.5, 0.15\,\mathrm{GeV}), (-0.5, 0.37\,\mathrm{GeV})\}. \tag{4.19}
$$

The result for the total CS kernel at $\mathrm{N^3LL'}$ (i.e., retaining the complete three-loop boundary condition and four-loop cusp evolution) is shown in figure 7 with the default set of model parameters $(c_\nu^q, \omega_{\nu,q}) = (-0.05, 0.25\,\mathrm{GeV})$ shown as a solid black line. The first two variations (indicated by long and short-dashed dark blue lines) are chosen such that they predominantly affect the CS kernel at short transverse distances $b_T \lesssim 0.197\,\mathrm{fm} \sim 1\,\mathrm{GeV}^{-1}$ by varying the quadratic coefficient in the OPE down or up, as illustrated in the right panel of figure 7. Since we expect the impact of the quadratic coefficient to be linear at $q_T \gtrsim 5\,\mathrm{GeV}$, we choose

the magnitude of $\omega_{\nu,q}$ and the sign of c_ν^q such that the variations they induce on the leading quadratic coefficient $\mathrm{sgn}(c_\nu^q)\,\omega_{\nu,q}^2 \in \{-0.1875\,\mathrm{GeV}^2, +0.0625\,\mathrm{GeV}^2\}$ are symmetric around the central value of $-0.0625\,\mathrm{GeV}^2$.

By contrast, the third and fourth variation in eq. (4.19) are chosen such that they only change the quadratic coefficient in the CS kernel by a smaller amount, and instead predominantly affect the behavior of the CS kernel at long distances by varying the sign $\mathrm{sgn}(c_\nu^q)$ and height $|c_\nu^q|$ of the plateau in the model function, as illustrated in the left panel of figure 7. Here we choose the magnitude of the variation such that it covers the spread of available lattice results as reviewed in ref. [178].[17]

For the effective nonperturbative one-parameter model for the TMD boundary conditions in eq. (3.28) we choose the following illustrative variations,

$$\Omega_Z \in \{0, 0.707\,\mathrm{GeV}\}\,. \tag{4.20}$$

Compared to our default central value of $\Omega_Z = 0.5\,\mathrm{GeV}$, these again amount to a symmetric variation of the leading quadratic coefficient $\Omega_Z^2 \in \{0, 0.5\,\mathrm{GeV}^2\}$ around the central value of $0.25\,\mathrm{GeV}^2$. We thus again expect the impact of these variations to be linear for $q_T \gtrsim 5\,\mathrm{GeV}$ [152].

Our results for the impact of the above nonperturbative parameter variations on the fiducial p_T^Z spectrum $\mathrm{N^3LL'} + \mathcal{O}(\alpha_s^3)$ are shown in figure 8. We indeed observe the expected symmetric opposite-sign impact of the short-distance down/up variations in the CS kernel and the variations of Ω_Z, respectively, at $q_T \gtrsim 5\,\mathrm{GeV}$. We furthermore observe that the impact of the short-distance variations of the CS kernel dominates over the long-distance variation for all bins at the LHC (including the very first one, which we clipped for readability), suggesting that the strong Sudakov suppression of the b_T-space cross section for resonant Drell-Yan makes it challenging to access the genuine long-distance behavior. We also note that the impact of the nonperturbative parameter variations, which we chose for illustration, is comparable to the estimated total perturbative uncertainty Δ_{pert}, which is shown as the yellow band in figure 8 for reference. It is interesting to note that the corresponding variations in the underlying model functions, see e.g. figure 7, exceed the typical uncertainties obtained in TMD global fits [45, 51], which however do not account for perturbative uncertainties in the fit.

Comparing to the experimental data, it seems likely — based on the first few bins — that the data in fact prefer weaker nonperturbative effects than our default choices (e.g. $\Omega_Z = 0$, solid green). However, the fact that the prediction for our default PDF set overshoots the data at $q_T \gtrsim 20\,\mathrm{GeV}$ cannot be addressed by the nonperturbative model since this region lies well outside of its effective range, i.e., because of the fact that the leading nonperturbative effects in the OPE have to fall off as $1/q_T^2$ upon Fourier transform [152].
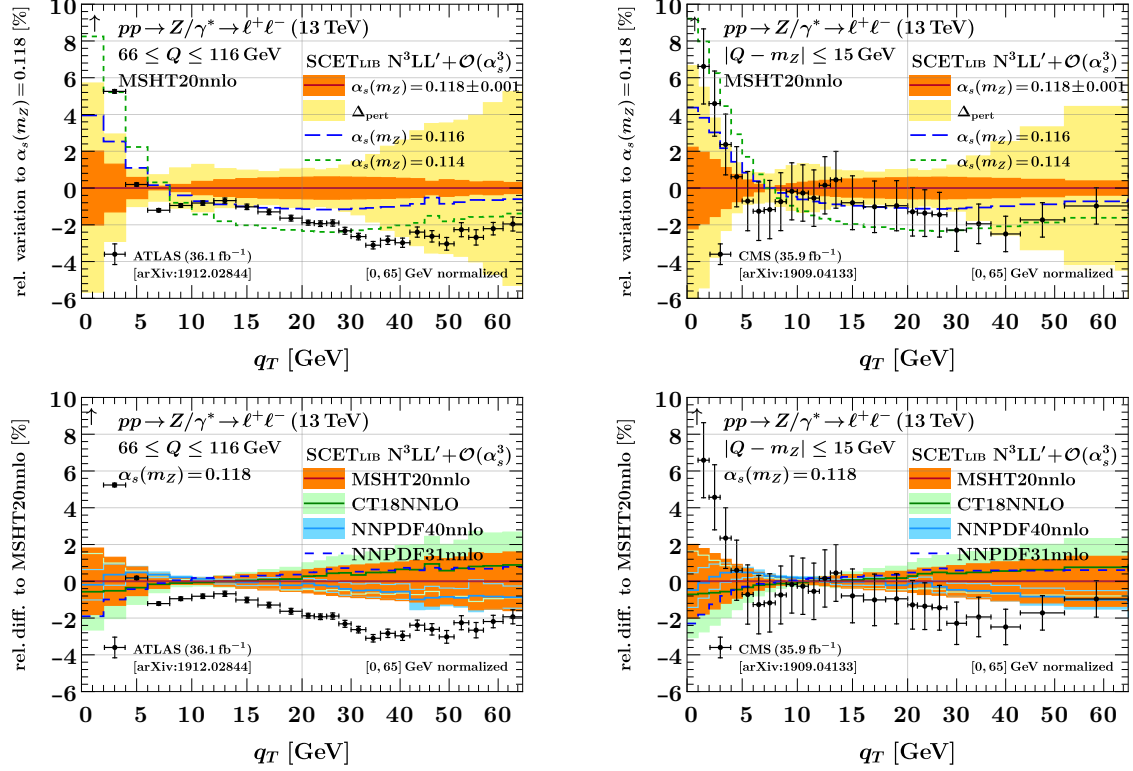
Figure 9. Impact of parametric strong coupling variations (top) and parametric PDF variations (bottom), as well as alternate PDF sets, on the normalized p_T^Z spectrum at $N^3LL' + \mathcal{O}(\alpha_s^3)$ compared to the ATLAS 13 TeV [5] (left) and CMS 13 TeV [11] (right) measurements.

		CT18NNLO	NNPDF31nnlo	NNPDF40nnlo
σ_{65} [pb]	ATLAS cuts [5]	659.2	678.1	691.3
	CMS cuts [11]	650.1	669.9	682.9

Table 3. Normalization factors for the central $N^3LL' + \mathcal{O}(\alpha_s^3)$ fiducial p_T^Z spectra shown in figure 9. The corresponding one for `MSHT20nnlo` is given in table 2.

4.3 Parametric α_s and PDF uncertainties

We next estimate the parametric uncertainties related to the strong coupling constant and the collinear PDFs on our prediction using standard methods, closely following those described in ref. [180]. In practical terms, both variations are performed only in the resummed singular cross section and the $\mathcal{O}(\alpha_s)$ nonsingular coefficient while keeping the $\mathcal{O}(\alpha_s^2)$ and $\mathcal{O}(\alpha_s^3)$ nonsingular coefficients at central values and at the reference PDF set, as already discussed in section 2.4. This strategy for the uncertainty estimation avoids performing CPU-intensive

---

[17]While high-precision lattice results at physical pion masses have recently become available [167], we leave it to future work to incorporate them directly in our prediction. Doing so in particular requires one to include and smoothly match the known perturbative bottom quark mass effects in the CS kernel [179] in order to correctly transition from the $n_f = 5$ massless limit to the precision results of ref. [167], which feature three light and one massive (charm) flavor.

runs for the FO nonsingular coefficients and is justified by the smallness of the $\mathcal{O}(\alpha_s^2)$ and the $\mathcal{O}(\alpha_s^3)$ nonsingular coefficients for $q_T \lesssim 65\,\mathrm{GeV}$.

For the uncertainty related to α_s, we perform variations of

$$\alpha_s(m_Z) = 0.118 \pm 0.001\,, \tag{4.21}$$

properly taking into account its effect on the DGLAP running and on PDF determinations by using the PDF set that consistently employs the corresponding value of $\alpha_s(m_Z)$. Eq. (4.21) roughly corresponds to the currently quoted PDG 2023 uncertainty [181]. The associated parametric α_s uncertainty is computed as

$$\Delta_{\alpha_s} = \frac{1}{\sqrt{2}}\Big[\left(\mathrm{d}\sigma_{\alpha_s,\mathrm{up}} - \mathrm{d}\sigma_{\mathrm{central}}\right)^2 + \left(\mathrm{d}\sigma_{\alpha_s,\mathrm{down}} - \mathrm{d}\sigma_{\mathrm{central}}\right)^2\Big]^{1/2}\,. \tag{4.22}$$

The resulting uncertainty on the normalized fiducial p_T^Z spectrum is shown in the top row of figure 9 (orange band). On the range $5 \leq q_T \leq 30\,\mathrm{GeV}$, the uncertainty is on par with Δ_{pert} (light yellow band) at this order. Neither of them is able to remedy the overshoot of the prediction compared to the data at ($q_T \gtrsim 15\,\mathrm{GeV}$). Curiously, we find that a lower value of the strong coupling, $\alpha_s(m_Z) = 0.114$ (short-dashed green), captures the data trend much more closely over a wide range of q_T, including in particular the region $q_T \geq 20\,\mathrm{GeV}$ where nonperturbative effects are already negligible, see section 4.2. While this observation did *not* result from an α_s fit, it is interesting to note since similarly low α_s values have been extracted in the past [182, 183] from other resummation-sensitive observables, specifically e^+e^- event shapes. We stress, however, that a complete fit of α_s to hadron-collider p_T^Z data must include profiling over the PDF set, as done e.g. in refs. [15, 16], and in section 4.4 we will indeed confirm that the inclusion of approximate N³LO effects in the PDF set in fact yields much closer agreement with the data for $\alpha_s(m_Z) = 0.118$ from the start.

For the uncertainty related to the collinear PDFs, we show results for CT18NNLO [157], NNPDF31nnlo [148], NNPDF40nnlo [148], and for our default set MSHT20nnlo [147]. Since these collaborations in general employ different methodologies in estimating an uncertainty from the fit, we follow the respective collaboration's nominal formula for calculating the corresponding uncertainty on our prediction. For Hessian sets such as CT18NNLO and MSHT20nnlo we use

$$\Delta_{\mathrm{PDF}}^{\mathrm{Hessian}} = \frac{1}{\sqrt{2}}\left[\sum_i^{n_{\mathrm{rep}}}(\mathrm{d}\sigma_i - \mathrm{d}\sigma_{\mathrm{central}})^2\right]^{1/2}\,. \tag{4.23}$$

The index i runs over the set of n_{rep} different replicas provided by each collaboration and $\mathrm{d}\sigma_{\mathrm{central}}$ ($\mathrm{d}\sigma_i$) denotes the prediction evaluated using the central member (i^{th} member) of the PDF set. Compared to eq. (20) of ref. [180], the relative factor of $1/\sqrt{2}$ in eq. (4.23) avoids the possible double counting induced by replicas of opposite eigenvectors in the symmetric limit. We note that we in addition rescale the resulting uncertainty for the CT18NNLO set to account for the difference in their quoted confidence level (CL, 90%) to our common target CL of 68% for all PDF sets. For Monte-Carlo (MC) sets such as NNPDF31nnlo and NNPD40nnlo, we use

$$\Delta_{\mathrm{PDF}}^{\mathrm{MC}} = \frac{1}{\sqrt{n_{\mathrm{rep}} - 1}}\left[\sum_i^{n_{\mathrm{rep}}}(\mathrm{d}\sigma_i - \mathrm{d}\sigma_{\mathrm{central}})^2\right]^{1/2}\,, \tag{4.24}$$

where for $\mathrm{d}\sigma_{\mathrm{central}}$ we use the averaged PDF replica provided by each set.
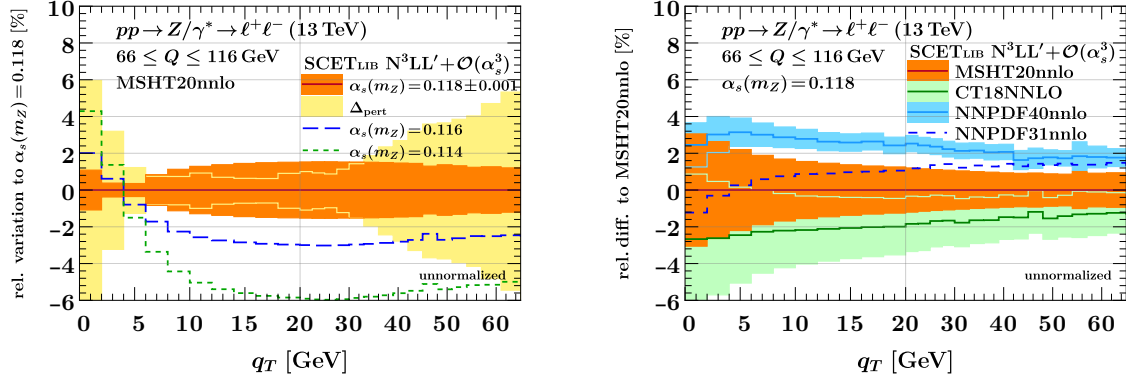
Figure 10. Impact of parametric strong coupling variations (left) and parametric PDF variations (right), as well as alternate PDF sets, on the *unnormalized p_T^Z* spectrum at $N^3LL' + \mathcal{O}(\alpha_s^3)$.

Turning to the bottom row of figure 9, we show the respective central values and parametric PDF uncertainties for `CT18NNLO` [157] (solid green), `NNPDF31nnlo` [156] (dashed blue) and `NNPDF40nnlo` [148] (solid blue) for the normalized p_T^Z spectrum, with the associated normalization factors given in table 3. Specifically, we show relative deviations from our default choice, `MSHT20nnlo` [147] (red). It is worth noting that all sets agree at the level of the normalized p_T^Z spectrum well within the uncertainties of the `CT18NNLO` and `MSHT20nnlo` predictions, while the `MSHT20nnlo` and `CT18NNLO` central values fall on the upper edge or outside of the `NNPDF40nnlo`, respectively. In particular, none of the PDF parametric uncertainties, and no alternate choice of central set at this PDF order (NNLO), is able to capture the discrepancy to the data at $q_T \geq 15\,\text{GeV}$. We have checked that this behavior of NNLO PDF sets, with a characteristic overshoot above the data at $q_T \geq 15\,\text{GeV}$, in fact persists for the p_T^Z spectrum as measured in bins of the Z boson rapidity at $8\,\text{TeV}$ by the ATLAS collaboration [4].

Concerning the nonperturbative region of $q_T \leq 5\,\text{GeV}$, it has been pointed out in ref. [168] that fits of nonperturbative TMD physics are subject to a sizable bias due to the choice of reference collinear PDF set. We find this surprising in light of the small ($\leq 1\%$) relative differences between modern PDF sets that we observe in this region for common nonperturbative inputs at the level of the self-consistently normalized p_T^Z spectrum. We hasten to add, however, that while the TMD fit of ref. [168] like other fits heavily relies on LHC data for resonant Drell-Yan, the latter are, of course, not the only data set entering the fit, and by our own universality arguments in section 3.4 insufficient to determine the individual TMDs or, indeed, fully assess the presence of bias due to the collinear PDFs.

We find it interesting to also consider the impact of the parametric uncertainties on the *unnormalized p_T^Z* spectrum, which we show in figure 10 for reference. Since the data sets for unnormalized spectra are more limited, we simply show our predictions on their own here, using the ATLAS cuts for definiteness; in section 5 we will perform direct comparisons to available data at the level of the unnormalized cumulative cross section, i.e., the piece of information orthogonal to the normalized spectrum. Interestingly, while the various PDF sets were in close agreement on the shape of the normalized spectrum, the agreement worsens at the level of the unnormalized spectrum, see the right panel of figure 10. Together with
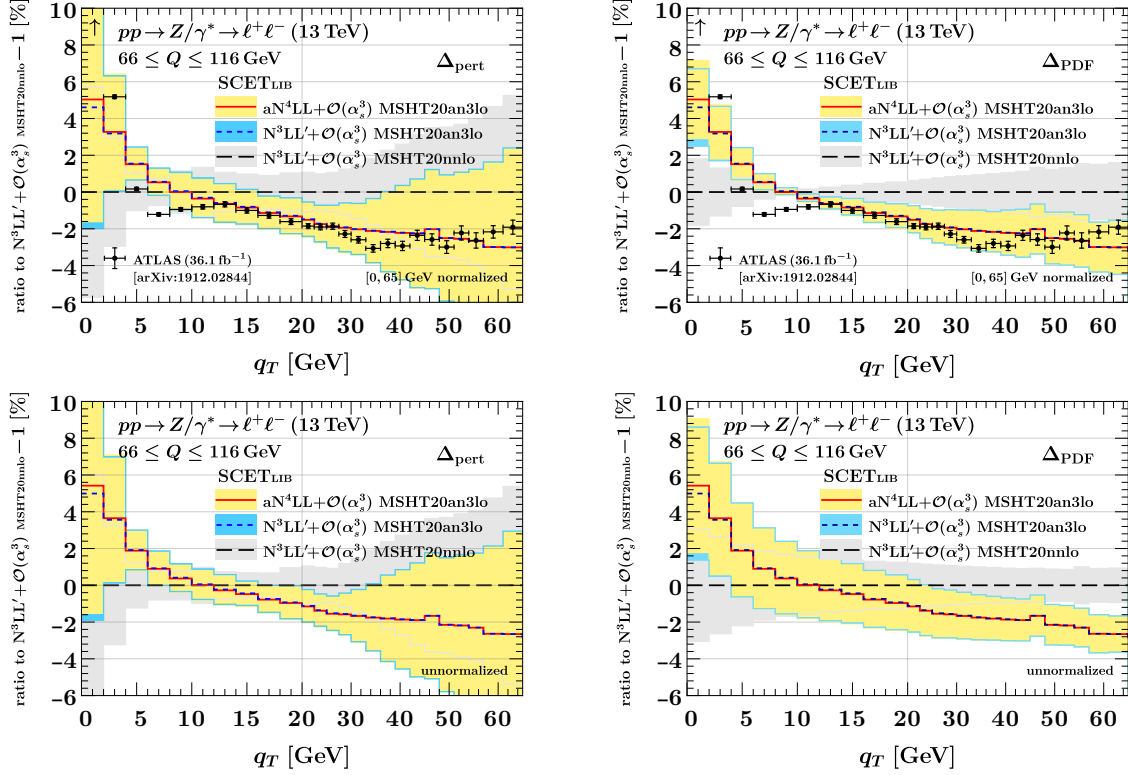
Figure 11. Impact of aN^{3}LO PDFs (blue) and of N^{4}LL Sudakov effects (red/yellow, with overall aN^{4}LL+$\mathcal{O}(\alpha_s^3)$ accuracy) on the fiducial p_T^Z spectrum relative to our baseline prediction (black/gray) using an NNLO PDF set at N^{3}LL'+$\mathcal{O}(\alpha_s^3)$ compared to the ATLAS 13 TeV measurement [5]. Here we compare the `MSHT20nnlo` and `MSHT20an3lo` PDF sets produced by the `MSHT` collaboration [27, 147]. Predictions on the left (right) are dressed with the perturbative (parametric PDF) uncertainty. The top (bottom) row shows the impact on the normalized (unnormalized) p_T^Z spectrum.

		MSHT20an3lo	NNPDF40an3lo
σ_{65} [pb]	aN^{4}LL+$\mathcal{O}(\alpha_s^3)$	675.975	691.963
	N^{3}LL' + $\mathcal{O}(\alpha_s^3)$	675.979	691.969

Table 4. Normalization factors for the additional fiducial p_T^Z spectra shown in figure 11 and 12. Normalization factors for the respective baseline NNLO PDF sets are given in tables 2 and 3.

our findings on the impact of nonperturbative physics and the size of the nonsingular cross section, this suggests an attractive strategy to distinguish between PDF sets at complete three-loop accuracy using the cumulative cross section, see section 5, which precisely retain the PDF sensitivity that usually cancels to a large extent in normalized spectra.

4.4 Impact of N^{4}LL Sudakov effects and approximate N^{3}LO PDFs

While all of our highest-order predictions so far involved partonic cross sections at complete three-loop accuracy, they employed NNLO PDFs determined using NNLO (three-loop) DGLAP evolution and NNLO theory predictions in the fit, which until recently constituted
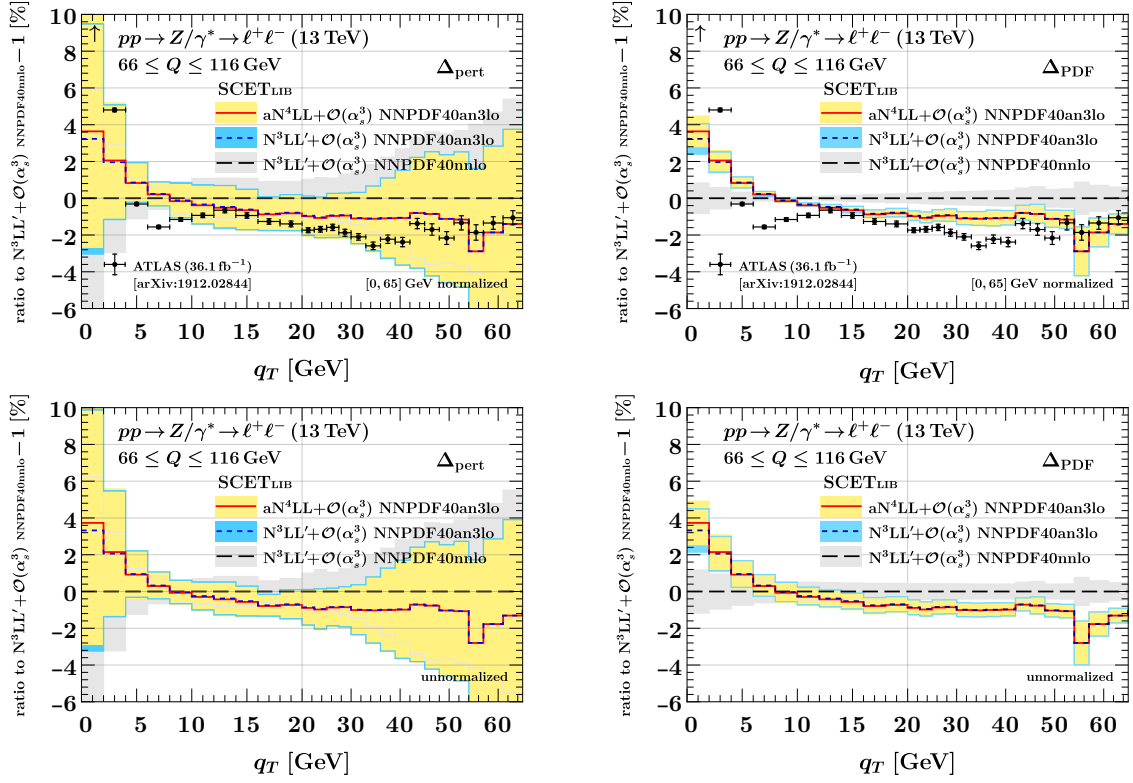
Figure 12. Same as figure 11, but comparing the `NNPDF40nnlo` and `NNPDF40an3lo` PDF sets produced by the `NNPDF` collaboration [28, 148].
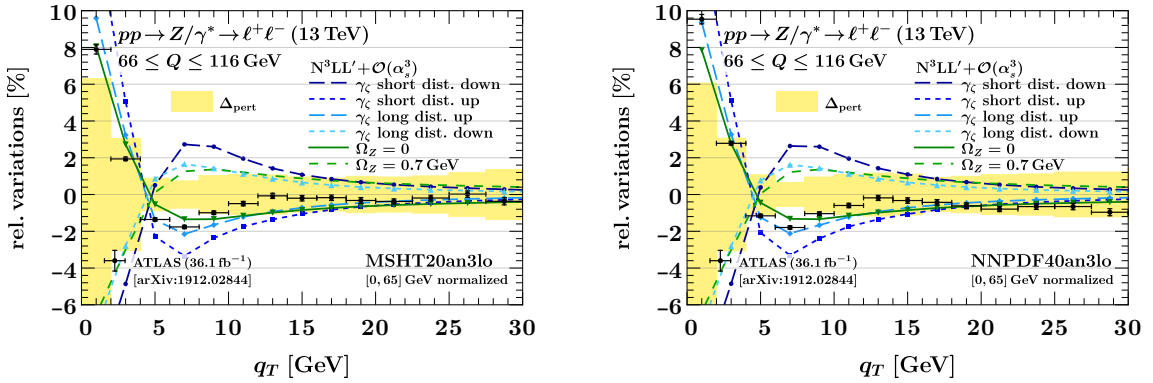
Figure 13. Impact of parameter variations in the nonperturbative TMD models at $N^3LL' + \mathcal{O}(\alpha_s^3)$ for the `MSHT20an3lo` PDF set [27] (left) and for the `NNPDF40an3lo` PDF set [28] (right) compared to the ATLAS 13 TeV measurement [5]. For illustration, we also compare to the estimated size Δ_{pert} of the perturbative uncertainty.

the state-of-the-art. Lately, both the `MSHT` and the `NNPDF` collaboration exploited the rapidly growing body of knowledge [184–188] on the N^3LO DGLAP and mass decoupling kernels in order to produce approximate N^3LO (aN^3LO) PDF sets [27–31]. Notably, in ref. [27] both the set of unknown N^3LO K factors for the relevant physical processes and the few remaining unknown N^3LO DGLAP ingredients are promoted to nuisance parameters [173, 174]. In addition, this allows for an improved uncertainty estimation of the PDF set, in principle also addressing common obstacles such as correlations between missing higher-order uncertainties in the fit and in predictions that use the PDF set.

Importantly, the DGLAP kernels also enter as a key set of noncusp anomalous dimensions in resummed predictions for the q_T spectrum, since they govern the evolution of the collinear PDFs from their input scale to the beam function scale $\mu_B \sim q_T \sim 1/b_T$. Specifically, since the input scale is effectively set by the weak scale $m_{W,Z} \sim Q$ in modern PDF sets due to the wealth of LHC data entering the fits, this evolution indeed resums a large single logarithm and cannot be bypassed when attempting to achieve N^4LL accuracy in any TMD or resummed prediction that uses collinear PDFs as input. Therefore, achieving (approximate) N^3LO DGLAP evolution provides the last missing ingredients for achieving (approximate) N^4LL accuracy at the level of the resummed spectrum. This is thanks to dedicated previous efforts to calculate (or numerically estimate) the five-loop β function [120], the five-loop cusp anomalous dimension [121], the four-loop rapidity anomalous dimension [131, 132], and the four-loop virtuality anomalous dimensions [115, 126], all of which are also necessary ingredients at this order. We collectively refer to these as "N^4LL Sudakov effects", as opposed to the purely single-logarithmic DGLAP evolution. Conversely, since all of these contributions are known either fully analytically or, in the case of the five-loop cusp anomalous dimension, estimated to sufficient precision given its small overall impact a resulting approximate N^4LL (aN^4LL) resummed prediction will be "approximate" precisely in the sense that the underlying PDF set is aN^3LO.

It is clearly of key interest to determine the size of the effect that N^3LO evolution and N^3LO fixed-order contributions in PDF fits have on the extremely precisely measured p_T^Z spectrum at the LHC, and similarly for N^4LL Sudakov effects. To do so, we have performed a complete implementation of the additional N^4LL Sudakov effects in `SCETlib` and interfaced them with the recent aN^3LO PDF sets to achieve aN^4LL accuracy. Numerical results produced with this further upgraded setup are shown in figure 11 and 12, with normalization factors reported in table 4. Specifically, beginning with the `MSHT` sets, we show predictions at $N^4LL+\mathcal{O}(\alpha_s^3)$ (red) and $N^3LL' + \mathcal{O}(\alpha_s^3)$ (dashed blue) with the `MSHT20an3lo` set, normalized to the $N^3LL' + \mathcal{O}(\alpha_s^3)$ results with the `MSHT20nnlo` set (dotted black) in figure 11. All predictions consistently employ the approximate unexpanded analytic RGE solutions [61] at the corresponding order, which are summarized in appendix A.

The effect of the approximate N^3LO PDF set is quite significant, leading to differences of up to $\sim 5\%$ to the corresponding NNLO PDF set in the low-q_T region and, crucially, a decrease of the prediction by $1 - 2\%$ in the region at $q_T \geq 15\,\text{GeV}$ where we previously observed an irreconcilable disagreement with the data. This implies that the three-loop ingredients that were included during the fitting procedure have a nontrivial impact, even at this high perturbative order. The much improved agreement in the region $q_T \geq 15\,\text{GeV}$ is

particularly remarkable in light of the fact that the shape of the p_T^Z spectrum at values of $q_T \leq 30\,\text{GeV}$ has never been used as an input for any PDF fits, cf. ref. [189] for its uses in the large p_T^Z fixed-order region. These findings are confirmed almost entirely by performing the analogous comparison between the two relevant NNPDF sets, as shown in figure 12, with only a slightly reduced change going from NNLO to aN^{3}LO in the region $q_T \geq 15\,\text{GeV}$ compared to MSHT. A similarly striking change from including aN^{3}LO PDF information into the prediction for the q_T spectrum has previously been reported in ref. [40], and the MSHT20an3lo has in the meantime also been adopted as the reference set for the $\alpha_s(m_Z)$ determination in ref. [16].

Turning to the N^{4}LL Sudakov effects, we find that their additional effect on top of the aN^{3}LO PDFs at aN^{4}LL is completely marginal in comparison. Specifically, in figure 11 the resummed and matched N^{4}LL prediction (red) only exhibits marginal differences to N^{3}LL$'$ (dashed blue) for the same PDF set (MSHT20an3lo). As expected, the uncertainty band of the former is contained within that of the latter, while their central values mildly differ ($\lesssim 0.5\%$) only in the first bin, indicating that the impact of the four-loop rapidity boundary term is not large.

Returning to the comparison to the data in the region $q_T \lesssim 10\,\text{GeV}$ we find that the agreement of even the aN^{3}LO PDF results (or, equivalently, the predictions at overall aN^{4}LL) with the data in this region is not optimal for our default nonperturbative model parameters. Since our nonperturbative parameters were chosen mainly for illustration, it is interesting to ask whether varying them further improves the agreement with the data and allows one to resolve the residual differences in the region where the nonperturbative model is effective. In figure 13 we thus show the same nonperturbative variations as in section 4.2, again at N^{3}LL$' + \mathcal{O}(\alpha_s^3)$, but in this case using the MSHT20an3lo (left) and NNPDF40an3lo sets (right). Taken at face value, no single parameter variation follows the entire data trend, but the typical size of the effect of short-distance variations in the Collins-Soper kernel and the TMD PDF effective model easily accounts for the remaining differences.

## 5 Results for cumulative fiducial p_T^Z cross sections

Our earlier observation of differences between PDF sets at the level of the unnormalized spectrum leads us to consider the cumulative p_T^Z cross section, defined in terms of the fiducial p_T^Z spectrum as follows,

$$\sigma(q_T^{\max}) = \int^{q_T^{\max}} \mathrm{d}q_T \, \frac{\mathrm{d}\sigma}{\mathrm{d}q_T} \,, \tag{5.1}$$

which can readily be computed in our framework by accumulating over bins in our previous predictions. To estimate perturbative uncertainties in this case, we perform the envelopes defined in section 4.1 after accumulating over bins, i.e., we treat the individual variations entering the envelope as fully correlated across bins. We stress that while this amounts to an ad-hoc assumption on the profile scale variations of section 4.1, it is, of course, a well-defined procedure for the parametric nonperturbative, α_s, and collinear PDF variations described in sections 4.2 and 4.3. The correct correlations of the perturbative uncertainties in q_T can be fully accounted for using the approach of refs. [173, 174].
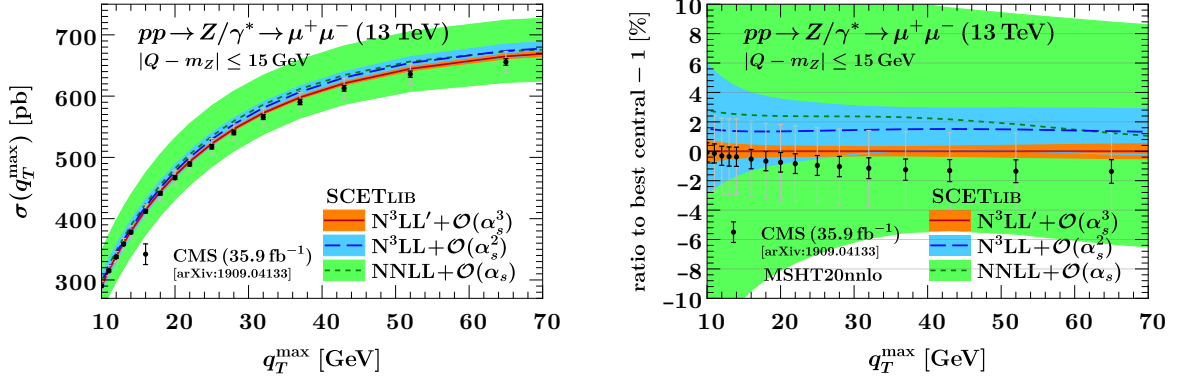
Figure 14. Predictions for the unnormalized cumulative fiducial cross section (left) and the relative difference to our prediction at the highest order (right) compared to the CMS 13 TeV measurement [11]. The black (gray) bars indicate the experimental uncertainty excluding (including) the luminosity uncertainty.
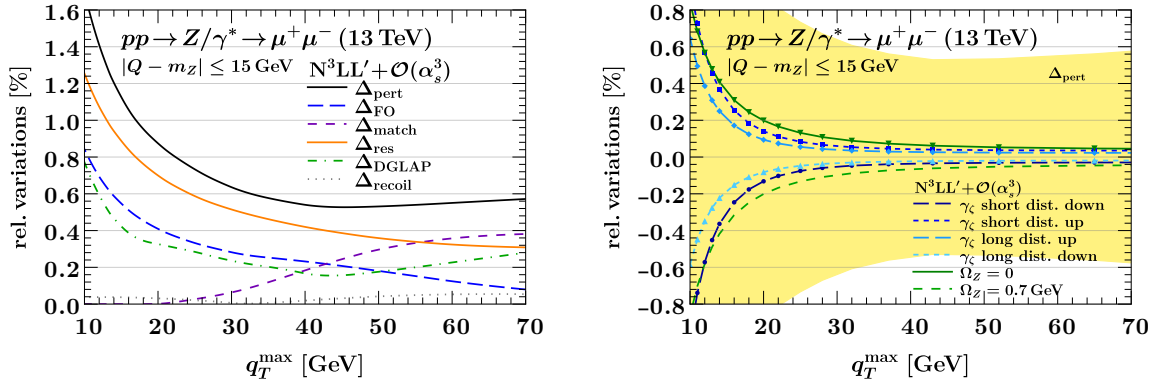
Figure 15. Left: breakdown of perturbative uncertainties contributing to the cumulative fiducial cross section at $N^3LL' + \mathcal{O}(\alpha_s^3)$. Right: impact of parameter variations in the nonperturbative TMD models on the cumulative fiducial cross section at $N^3LL' + \mathcal{O}(\alpha_s^3)$. For illustration, we also compare to the estimated size Δ_{pert} of the total perturbative uncertainty.

We compare our predictions to the CMS 13 TeV measurement in the $\mu^+\mu^-$ channel [11] using dressed muons. Both the unnormalized fiducial spectrum and its complete experimental covariance matrix were reported for this channel, allowing us to fully reconstruct the experimental uncertainty on the cumulative cross section as a function of q_T^{max}. Our results are shown in figure 14. We again observe excellent perturbative coverage and convergence, this time at the level of the cumulative cross section, with the total perturbative uncertainty estimate below the percent level at $N^3LL' + \mathcal{O}(\alpha_s^3)$, on par with the experimental uncertainty if one excludes the common overall luminosity uncertainty. The prediction for our default `MSHT20nnlo` PDF set overshoots the data, but the difference can easily be accounted for, as we will see below, by the spread between NNLO PDF sets.

To substantiate the percent-level perturbative precision of the $N^3LL' + \mathcal{O}(\alpha_s^3)$ result, we consider the breakdown of the perturbative uncertainty in the left panel of figure 15. We find that the matching uncertainty, which increases with q_T^{max}, plays a crucial role in
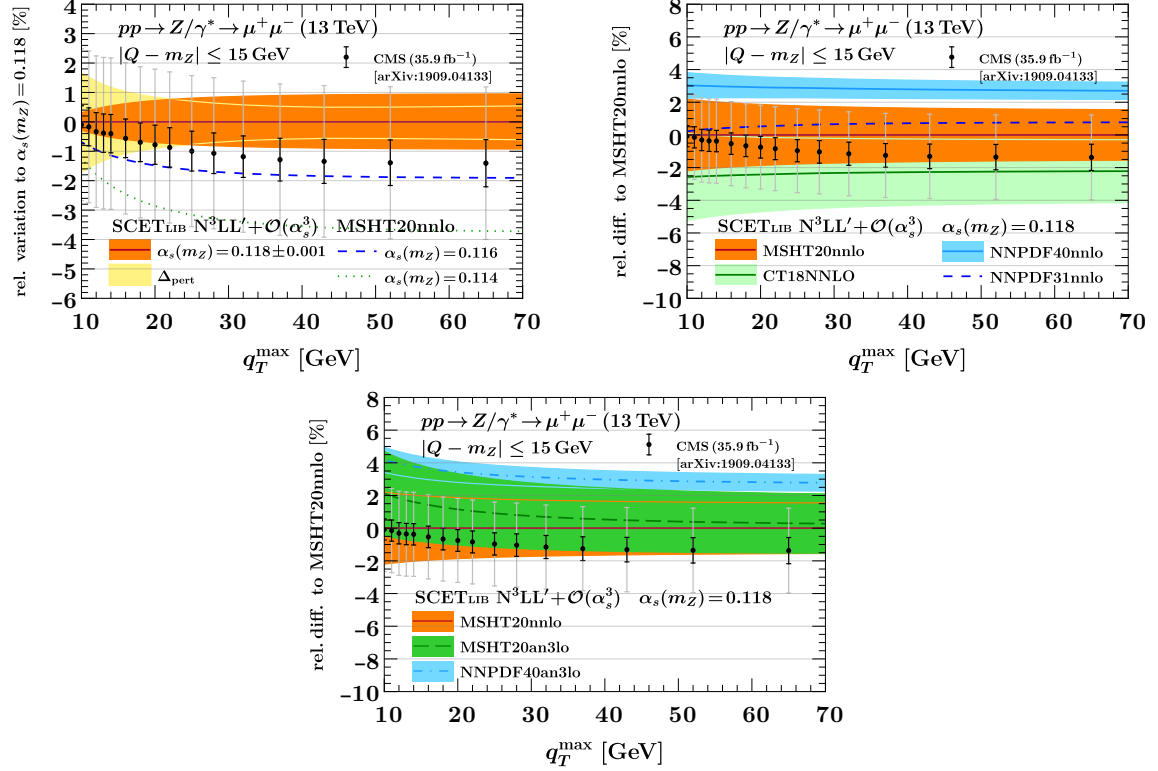
Figure 16. Impact of parametric strong coupling variations (top left) and parametric PDF variations for alternate NNLO PDF sets (top right), as well as for aN³LO PDF sets (bottom), on the cumulative fiducial cross section at N³LL′ + $\mathcal{O}(\alpha_s^3)$, compared to the CMS 13 TeV measurement [11]. The black (gray) bars indicate the experimental uncertainty excluding (including) the luminosity uncertainty.

stabilizing the uncertainty estimate towards the fixed-order region. While an uncertainty of $\leq 0.6\%$ at $q_T^{\max} \geq 30\,\text{GeV}$ may seem aggressive even for a three-loop prediction, we believe that our careful estimate derived from a large number of sources is reliable (and indeed could be considered conservative at the level of the spectrum). In the right panel of figure 15 we consider the impact of the same model parameter variations encoding nonperturbative TMD that we previously introduced in section 4.2. We find that the relative impact of any reasonably sized variations is at the permille level already for $q_T^{\max} \geq 25\,\text{GeV}$, as expected from their $(1/q_T^{\max})^2$ falloff. This suggests that while the cumulative cross section in this region is still sensitive to the effects of *perturbative* resummation, it is essentially unaffected by genuinely nonperturbative physics, implying that it is fully predicted in terms of the strong coupling and the collinear PDFs.

Turning now to the top left panel of figure 16, we see that the impact of strong coupling variations of 0.118 ± 0.001 on the cumulative cross section is small and roughly of $\mathcal{O}(1\%)$, which should be contrasted with the much stronger impact of α_s on the shape of the spectrum, see the top left panel of figure 9. The most interesting observation of this section is found in the top right and bottom panels of figure 16, where we compare the impact of alternate PDF choices and PDF parametric uncertainties on the prediction for NNLO PDFs and aN³LO PDFs, respectively. Keeping in mind the $\leq 1\%$ perturbative accuracy of our predictions,

		NNLL+$\mathcal{O}(\alpha_s)$	N^{3}LL+$\mathcal{O}(\alpha_s^2)$	N^{3}LL$'$ + $\mathcal{O}(\alpha_s^3)$
σ_{60} [pb]	W^+	4294.6	4277.6	4230.3
	W^-	3281.5	3257.8	3220.1

Table 5. Normalization factors for the fiducial p_T^W spectra shown in figure 17.

we find that our prediction together with the similarly precise experimental data can easily distinguish between both NNLO and aN^{3}LO PDF sets, and also constrain them further to a fraction of their currently quoted uncertainties.

Discussion. Our findings for the cumulative cross section suggest an appealing strategy to perform PDF fits at complete three-loop accuracy using our predictions here. Specifically, one could envision a scheme where the nonsingular cross sections at $\mathcal{O}(\alpha_s^2)$ and $\mathcal{O}(\alpha_s^3)$, which are numerically extremely expensive but small, are computed only once at a reference PDF set and then treated as a fixed bias correction while propagating the PDF through the orders of magnitude cheaper resummed cross section during the fit. The latter has complete three-loop accuracy, but much more beneficial scaling of computational cost with the loop order. Such a scheme is particularly attractive given that PDF fit templates at complete N^{3}LO accuracy, as required to further improve on the existing aN^{3}LO PDF fits [27–31], are still lacking beyond total inclusive cross sections [190], and have to be extrapolated to fiducial quantities using K factors. By contrast, the scheme we propose here could even be extended easily to the cumulative cross section differential in rapidity at negligible additional cost (mainly due to the more differential reference nonsingular). Importantly, our findings for the impact of nonperturbative TMD physics confirm that while resummation sensitive, the cumulative cross section for the $q_T^{\max}$ values of interest is in fact nearly free of nonperturbative effects and well suited for a perturbative QCD fit at leading twist.

6   Results for the fiducial $p_T^{W^\pm}$ spectrum

We finally use our setup to provide predictions for the transverse momentum spectrum of W^+ and W^- bosons at the LHC. We apply the following set of reference fiducial cuts,

$$p_T^\ell > 25\,\text{GeV}\,, \qquad |\eta_\ell| < 2.5\,, \qquad p_T^\nu > 25\,\text{GeV}\,, \qquad m_{T,W} > 50\,\text{GeV} \tag{6.1}$$

where the definition of a "transverse mass" often used in W analyses reads

$$m_{T,W}^2 \equiv \left(p_T^\ell + p_T^\nu\right)^2 - \left(\vec{p}_T^{\,\ell} + \vec{p}_T^{\,\nu}\right)^2\,, \tag{6.2}$$

and it is understood that the magnitude and direction of $\vec{p}_T^{\,\nu}$ are reconstructed from the missing transverse energy and transverse momentum in the event. Our results for the normalized p_T^W spectrum, its perturbative uncertainty, and the perturbative uncertainty breakdown, are shown in figure 17. To account for the slightly larger nonsingular cross section due to the lower effective value of Q, we here choose to normalize our predictions to a reference range of $0 \le q_T \le 60\,\text{GeV}$, with normalization factors given in table 5. We find that most features of the prediction, notably including the perturbative convergence and coverage, closely resemble those we found for the p_T^Z spectrum. An interesting difference between the two is found when
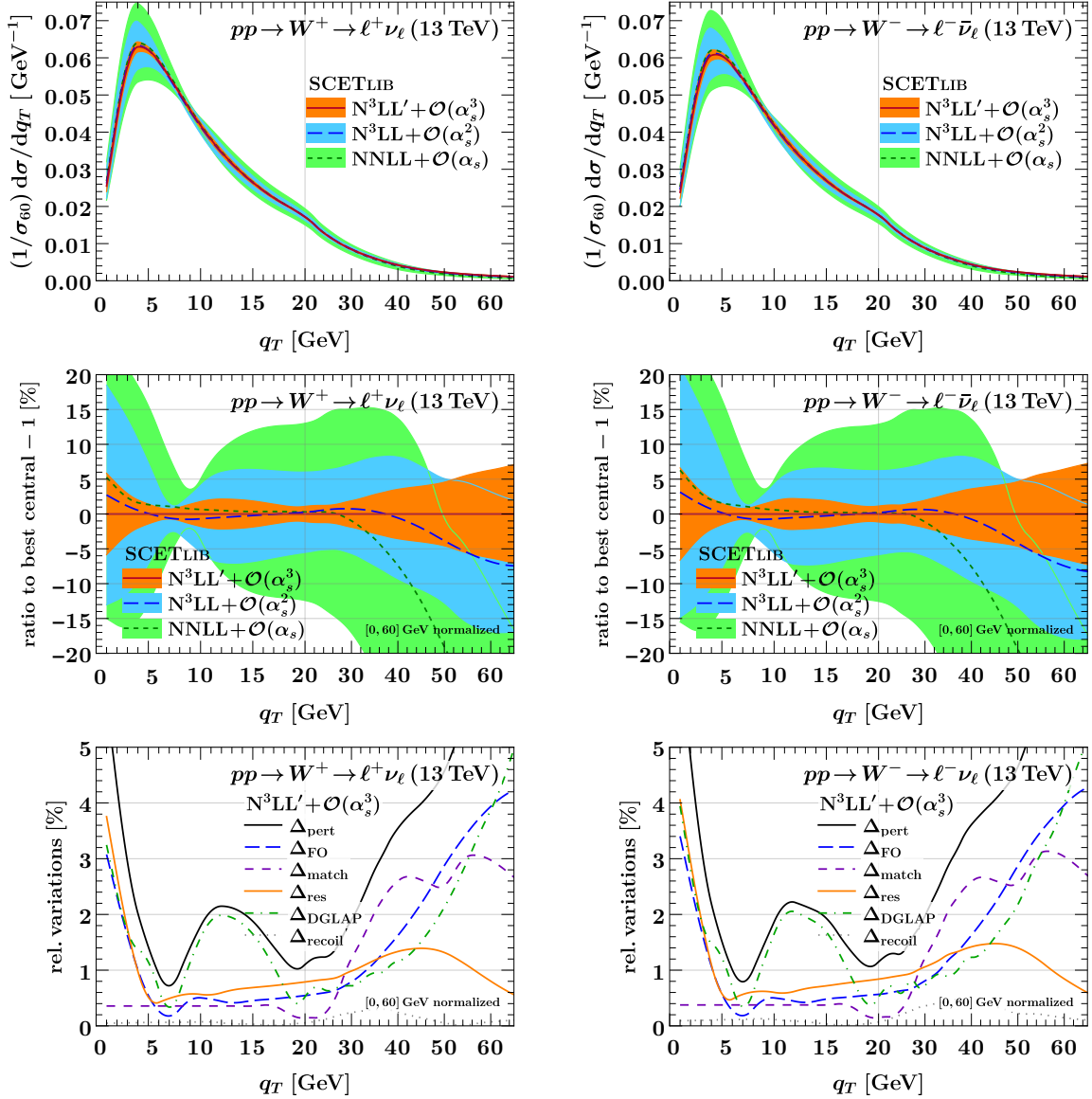
Figure 17. The normalized transverse momentum spectrum (top), its relative difference to the highest-order prediction (middle), and the complete perturbative uncertainty decomposition in terms of each contributing source (bottom) for W^+ (left) and W^- (right) production.

considering the "factorization scale" uncertainty Δ_{DGLAP}, see eq. (4.13), which has a much more pronounced peak at $q_T \sim 12\,\mathrm{GeV}$ in this case, reaching a peak height of about 2%. As previously found for the Z, these oscillations are due to the discontinuity of the PDF μ dependence at the bottom quark threshold, and in this case — to our understanding — are more pronounced because the sea and heavy quark channels (strange and charm) relevant here are more susceptible than valence quarks to the discontinuous change in the gluon PDF. We note that an alternate, more direct way of assessing these kinds of secondary heavy-quark effects would consist of performing variations of the bottom-quark decoupling scale μ_b away from the canonical $\mu_b = m_b$.
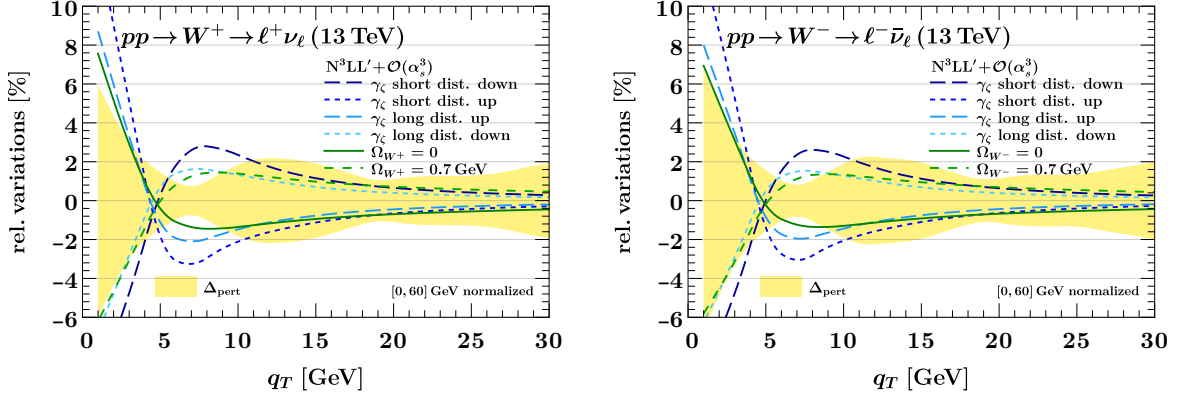
Figure 18. Impact of parameter variations in the nonperturbative TMD models on the normalized W^+ (left) and W^- (right) p_T spectrum at $\mathrm{N^3LL'} + \mathcal{O}(\alpha_s^3)$. For illustration, we also compare to the estimated size Δ_{pert} of the perturbative uncertainty.

Finally, the impact of the nonperturbative parameter variations described in section 4.2 on the p_T^W spectra is shown in figure 18. While the W^+ and W^- cases closely resemble each other and the Z results in figure 8, we remind the reader that the interpretation and value of the effective parameter Ω_V encoding the TMD PDF boundary conditions is in principle different for each of $V = Z, W^+, W^-$, and correlations between them must necessarily be predicted from a full TMD flavor model. By contrast, for an analysis as in ref. [21] involving *only* W bosons, but no tuning to the Z, effective (rapidity-dependent) nonperturbative functions are fully sufficient, as we proved in sections 3.3 and 3.4.

7 Summary and conclusions

In this paper, we have provided state-of-the-art QCD precision predictions for the transverse momentum (q_T) spectra of electroweak bosons at the LHC up to $\mathrm{N^3LL'}$ and approximate $\mathrm{N^4LL}$ in resummation-improved perturbation theory, matched to available $\mathcal{O}(\alpha_s^3)$ fixed-order results. Our predictions fully account for the effect of realistic fiducial selection cuts on the decay leptons, incorporate the entire relevant and available perturbative information at three, four, and five-loop order in QCD, and feature a rigorously defined field-theoretic description of the nonperturbative TMD physics at small $q_T \gtrsim \Lambda_{\mathrm{QCD}}$. We have placed particular emphasis on careful estimates of the magnitude of residual perturbative uncertainties on our predictions, also assessing in detail the impact of scheme choices made to perform the matching between nonperturbative, resummed perturbative, and fixed-order contributions to the spectrum. This makes our predictions the first of their kind to consistently incorporate all information from the nonperturbative region of $q_T \gtrsim \Lambda_{\mathrm{QCD}}$ all the way up to the fixed-order tail $q_T \sim m_Z, m_W$ with a complete assessment of the associated matching uncertainties. In addition, we have studied the parametric strong coupling and PDF uncertainties in detail, finding that NNLO PDF sets consistently overshoot the data at intermediate q_T, a mismatch that is successfully resolved *a priori* by the recent $\mathrm{aN^3LO}$ PDF determinations. By contrast, the additional $\mathrm{N^4LL}$ Sudakov resummation ingredients at overall $\mathrm{aN^4LL}$ accuracy only have a negligible impact beyond the baseline $\mathrm{N^3LL'}$ prediction. Our predictions are made possible by a fast, modular,

and well-tested implementation of N^4LL resummation with fiducial cuts in the `SCETlib` numerical C++ library. This `scetlib-qT` module, for which a public release is foreseen, has in the meantime already found several applications [21, 26, 78, 174], in particular as a key ingredient of the recent CMS m_W measurement [21].

Regarding the treatment of nonperturbative TMD physics, our analysis for the first time clarifies in detail under what conditions the — in general very complicated — flavor and Bjorken-x dependence of the nonperturbative quark TMD PDFs can be captured by a much simpler effective nonperturbative function for a given process. Indeed, we are able to formally derive the intuitive notion that all nonperturbative effects in the p_T^V transverse momentum and rapidity spectrum of a given resonantly produced electroweak boson V at a given collider configuration can be captured by a *single effective one-dimensional function* of the transverse distance b_T. We also showed simple pocket formulas to convert back to general flavor-dependent TMD models. A similar result holds for the effective two-dimensional function if the rapidity of V (or the pseudorapidity of a decay lepton) is measured in addition. The complexity reduces further to a single nonperturbative number (or a one-dimensional function of the rapidity) if only the leading quadratic correction of $\mathcal{O}(\Lambda_{QCD}^2 b_T^2)$ is considered, generalizing the approach of ref. [152]. While at face value this may seem like a step backward from the desired goal of TMD universality as assessed by global TMD fits, our insights in fact have two important uses:

(a) If a self-contained analysis of a single process is performed, e.g. when extracting the strong coupling from resonant Z production or the W mass from W boson data *alone*, our analysis clarifies the most general form of the nonperturbative physics that must be included in this case. In fact, all of our predictions in this paper for single-differential resonant p_T^Z and p_T^W spectra make heavy use of this, since it allows us to illustrate the most general effect of TMD physics (beyond that of the Collins-Soper kernel) by varying a single parameter Ω_V in each case.

(b) Conversely, our statements about the validity of effective models can be read as precisely specifying the maximum information on nonperturbative TMD physics that can be extracted from a given p_T^V spectrum in the context of a global fit. Specifically, in the idealized limit where the spectrum is measured and perturbatively predicted to perfect precision, it reduces the most general TMD nonperturbative parameter space by exactly one dimension at each order in $(\Lambda_{QCD} b_T)^{2n}$.

As an exciting immediate application of our predictions, we have identified a strong sensitivity of the unnormalized *cumulative* p_T^Z cross section to the physics of collinear PDFs, with differences between recent PDF sets easily resolved within our three-loop perturbative and the typical experimental uncertainties. Our framework also allows us to fully assess the impact of nonperturbative physics on the cumulative cross section, indicating that it is at the permille level already for a cumulative cut at $q_T^{max} = 20\,\text{GeV}$. Making use of the power expansion in $(p_T^Z/m_Z)^2$ valid in this region, we furthermore expect that the small — but numerically extremely expensive — nonsingular cross section can be treated as a fixed bias correction in future PDF fits to this observable, while the PDF can easily be propagated exactly through the much cheaper three-loop resummed cross section during the fit, also differential

in rapidity. Fits to the cumulative fiducial p_T^Z cross section at a value of $q_T^{\max} = 20 - 30\,\text{GeV}$ thus provide a very promising avenue for a numerically inexpensive, but nevertheless fully three-loop accurate theory template for future improvements to approximate N^{3}LO PDF sets.

In summary, the predictions and conceptual advances in this paper constitute another important step towards a rigorous and comprehensive study of transverse momentum spectra at hadron colliders. We look forward to future applications of our results to precision QCD and electroweak physics at the LHC.

Acknowledgments

A Renormalization group solutions at N^{4}LL

The four-loop boundary condition for the rapidity anomalous dimension at a general scale $\mu \sim 1/b_T$ is easily derived from eq. (2.18) in terms of the cusp anomalous dimension and the recently calculated four-loop constant term $\tilde{\gamma}_{\nu\,3}^i$ at $\mu = b_0/b_T$ [132, 133]. Using the conventions and notation of ref. [127], it reads

$$
\begin{aligned}
\tilde{\gamma}_\nu^{i\,(3)}(b_T,\mu) = {} & -L_b^4 \frac{1}{2}\beta_0^3 \Gamma_0^i + L_b^3\big(\beta_0^3 \tilde{\gamma}_{\nu\,0}^i - \frac{5}{3}\beta_0 \beta_1 \Gamma_0^i - 2\beta_0^2 \Gamma_1^i\big) \\
& + L_b^2\Big(\frac{5}{2}\beta_0 \beta_1 \tilde{\gamma}_{\nu\,0}^i + 3\beta_0^2 \tilde{\gamma}_{\nu\,1}^i - \beta_2 \Gamma_0^i - 2\beta_1 \Gamma_1^i - 3\beta_0 \Gamma_2^i\Big) \\
& + L_b\big(\beta_2 \tilde{\gamma}_{\nu\,0}^i + 2\beta_1 \tilde{\gamma}_{\nu\,1}^i + 3\beta_0 \tilde{\gamma}_{\nu\,2}^i - 2\Gamma_3^i\big) + \tilde{\gamma}_{\nu\,3}^i\,,
\end{aligned}
\tag{A.1}
$$

where $L_b = \ln\big(b_T^2 \mu^2/b_0^2\big)$.

Next, using the conventions and nomenclature of ref. [61], the N^{4}LL iterative solution for the running of the strong coupling reads

$$\frac{\alpha(\mu_0)}{\alpha(\mu)} = X + \epsilon \frac{\alpha(\mu_0)}{4\pi} b_1 \ln X + \epsilon^2 \frac{\alpha(\mu_0)^2}{(4\pi)^2}\left(b_2 \frac{X-1}{X} + b_1^2 \frac{1-X+\ln X}{X}\right)$$

$$+ \epsilon^3 \frac{\alpha(\mu_0)^3}{(4\pi)^3}\left[b_3 \frac{X^2-1}{2X^2} + b_2 b_1\left(\frac{1-X}{X} + \frac{\ln X}{X^2}\right) + b_1^3 \frac{(1-X)^2 - \ln^2 X}{2X^2}\right]$$

$$+ \epsilon^4 \frac{\alpha(\mu_0)^4}{(4\pi)^4} \frac{1}{6X^3}\Big[(1-X)\big((2X^2-X-1)b_1^4 - 6(X^2-1)b_1^2 b_2 + 2(X^2+X-2)b_2^2$$

$$+ (4X^2+X+1)b_1 b_3 - 2(X^2+X+1)b_4\big) + 6b_1\big((X-1)b_1^3 + (1-X)b_1 b_2 + b_3\big)\ln X$$

$$- 3(b_1^4 + 2b_1^2 b_2)\ln^2 X + 2b_1^4 \ln^3 X\Big], \tag{A.2}$$

where $b_n = \beta_n/\beta_0$, $X = 1 + \frac{\alpha_s(\mu_0)}{2\pi}\beta_0 \ln(\mu/\mu_0)$, and $\epsilon = 1$ is a bookkeeping parameter for the order of the expansion. Finally, using again the techniques and notation of ref. [61], the N^{4}LL iterative solutions for the building blocks of the Sudakov evolution kernels are given by

$$K_\Gamma(\mu_0,\mu) = -\frac{\Gamma_0}{4\beta_0^2}\Bigg\{\frac{4\pi}{\alpha(\mu_0)}\left(1 - \frac{1}{r} - \ln r\right) + \epsilon\left[(\hat{\Gamma}_1 - b_1)(1-r+\ln r) + \frac{b_1}{2}\ln^2 r\right]$$

$$+ \epsilon^2 \frac{\alpha(\mu_0)}{4\pi}\left[(b_1^2 - b_2)\left(\frac{1-r^2}{2} + \ln r\right) + (b_1\hat{\Gamma}_1 - b_1^2)(1-r+r\ln r)\right.$$

$$\left. - (\hat{\Gamma}_2 - b_1\hat{\Gamma}_1)\frac{(1-r)^2}{2}\right] + \epsilon^3 \frac{\alpha(\mu_0)^2}{(4\pi)^2}\left[(b_2 - b_1^2)(\hat{\Gamma}_1 - b_1)\frac{(1-r)^2(2+r)}{3}\right.$$

$$+ (\hat{\Gamma}_3 - b_3 - b_1(\hat{\Gamma}_2 - b_2))\left(\frac{1-r^3}{3} - \frac{1-r^2}{2}\right)$$

$$+ b_1(\hat{\Gamma}_2 - b_2 - b_1(\hat{\Gamma}_1 - b_1))\left(\frac{1-r^2}{4} + \frac{r^2\ln r}{2}\right)$$

$$+ (-b_3 + 2b_1 b_2 - b_1^3)\left(\frac{1-r^2}{4} + \frac{\ln r}{2}\right)\Bigg]$$

$$+ \epsilon^4 \frac{\alpha(\mu_0)^3}{(4\pi)^3}\left[\frac{b_3\hat{\Gamma}_1}{12}(5 - 6r - 2r^3 + 3r^4) + \frac{b_2\hat{\Gamma}_2}{4}(1 - 2r^2 + r^4) - \frac{\hat{\Gamma}_4}{12}(1 - 4r^3 + 3r^4)\right.$$

$$- \frac{b_4}{36}(1 + 8r^3 - 9r^4 + 12\ln r) - \frac{b_2^2}{36}(5 - 18r^2 + 4r^3 + 9r^4 - 12\ln r)$$

$$- \frac{b_1^4}{12}(7 - 6r(1+r) + 2r^3 + 3r^4 - 4\ln r + 4r^3\ln r)$$

$$+ \frac{b_1^3\hat{\Gamma}_1}{36}(25 - 18r(1+r) + 2r^3 + 9r^4 + 12r^3\ln r)$$

$$- \frac{b_1^2\hat{\Gamma}_2}{36}(13 - 18r^2 - 4r^3 + 9r^4 + 12r^3\ln r)$$

$$+ \frac{b_2 b_1^2}{36}(41 - 36r(1+r) + 4r^3 + 27r^4 - 36\ln r + 24r^3\ln r)$$

$$- \frac{b_3 b_1}{18}(7 - 9r - 7r^3 + 9r^4 - 12\ln r + 6r^3\ln r) + \frac{b_1\hat{\Gamma}_3}{36}(7 - 16r^3 + 9r^4 + 12r^3\ln r)$$

$$- \frac{b_2 b_1\hat{\Gamma}_1}{18}(20 - 18r - 9r^2 - 2r^3 + 9r^4 + 6r^3\ln r)\Bigg]\Bigg\}, \tag{A.3}$$
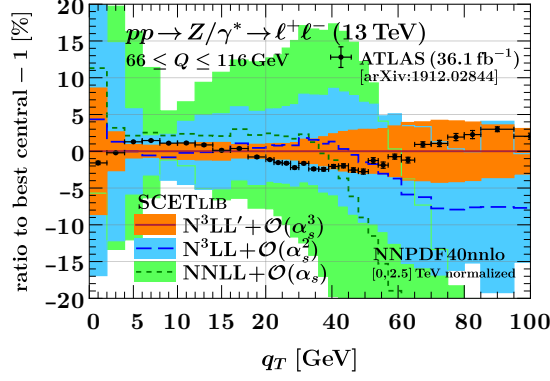
Figure 19. Same as the center left panel of figure 6, but normalizing to the whole kinematic range of $0 \leq q_T \leq 2.5$ TeV instead. For the purposes of this plot, we in addition switched to the `NNPDF40nnlo` PDF set as baseline, cf. figure 9, and turned off the nonperturbative model for use as a reference. Further modifications are described in the text. The prediction at the highest order still visibly overshoots the data for $q_T \geq 20$ GeV with these settings, and is not compatible with it within uncertainty.

	NNLL$+\mathcal{O}(\alpha_s)$	N^{3}LL$+\mathcal{O}(\alpha_s^2)$	N^{3}LL$' + \mathcal{O}(\alpha_s^3)$
σ [pb]	724.01	728.9	722.1

Table 6. Normalization factors for the fiducial p_T^Z spectrum shown in figure 19.

$$K_\gamma(\mu_0,\mu) = -\frac{\gamma_0}{2\beta_0}\left[\epsilon \ln r + \epsilon^2 \frac{\alpha(\mu_0)}{4\pi}(\hat{\gamma}_1 - b_1)(r-1) + \epsilon^3 \frac{\alpha(\mu_0)^2}{(4\pi)^2}(\hat{\gamma}_2 - b_1\hat{\gamma}_1 + b_1^2 - b_2)\frac{r^2-1}{2}\right.$$
$$\left. + \epsilon^4 \frac{\alpha(\mu_0)^3}{(4\pi)^3}\left[\hat{\gamma}_3 - b_3 - b_1(\hat{\gamma}_2 - b_2) + (b_1^2 - b_2)(\hat{\gamma}_1 - b_1)\right]\frac{r^3-1}{3}\right], \tag{A.4}$$

$$\eta_\Gamma(\mu_0,\mu) = -\frac{\Gamma_0}{2\beta_0}\left[\ln r + \epsilon \frac{\alpha(\mu_0)}{4\pi}(\hat{\Gamma}_1 - b_1)(r-1) + \epsilon^2 \frac{\alpha(\mu_0)^2}{(4\pi)^2}(\hat{\Gamma}_2 - b_1\hat{\Gamma}_1 + b_1^2 - b_2)\frac{r^2-1}{2}\right.$$
$$+ \epsilon^3 \frac{\alpha(\mu_0)^3}{(4\pi)^3}\left[\hat{\Gamma}_3 - b_3 - b_1(\hat{\Gamma}_2 - b_2) + (b_1^2 - b_2)(\hat{\Gamma}_1 - b_1)\right]\frac{r^3-1}{3}$$
$$+ \epsilon^4 \frac{\alpha(\mu_0)^4}{(4\pi)^4}\left[b_1^4 + b_2^2 - b_4 - b_1^3\hat{\Gamma}_1 - b_3\hat{\Gamma}_1 - b_2\hat{\Gamma}_2\right.$$
$$\left.\left. + b_1^2(\hat{\Gamma}_2 - 3b_2) + b_1(2b_3 + 2b_2\hat{\Gamma}_1 - \hat{\Gamma}_3) + \hat{\Gamma}_4\right]\frac{r^4-1}{4}\right], \tag{A.5}$$

where in addition $\hat{\Gamma}_n = \Gamma_n/\Gamma_0$, $\hat{\gamma}_n = \gamma_n/\gamma_0$, and $r = \alpha_s(\mu)/\alpha_s(\mu_0)$.

B Reference results for spectra normalized to the full q_T range

In this appendix we provide reference results for the fiducial p_T^Z spectrum normalized on the whole kinematic range, i.e., extending all the way into the far fixed-order tail. To do so, we directly use the fixed-order data from ref. [43] to perform the matching without additional modification, also adopting the original slicing cut of $q_T^{\rm cut} = 0.447$ GeV used in that reference, and switch to `NNPDF40nnlo` as the baseline PDF set. For consistency and ease of comparison with the resummed component of ref. [43] (and the integrated counterterm, i.e., the fixed-order

singular cross section, in the N³LO results of ref. [43]), we furthermore switch off all singlet terms in the hard function and switch off the nonperturbative model by setting

$$\omega_{\nu,q} = \Omega_Z = 0. \tag{B.1}$$

Our results with these settings are shown in figure 19, with normalization factors (i.e., total fiducial Drell-Yan cross sections) reported in table 6. As further consistency checks against the fixed-order results reported in ref. [43], we have verified that the LO cross section agrees in all significant digits, and that the $\mathcal{O}(\alpha_s^3)$ increment to the fixed-order cross section, reported as $-18.7(1.1)$ pb in ref. [43], is in numerical agreement with our result of $-19.0(1.1)$ pb within numerical uncertainty.[18]

Data Availability Statement. This article has no associated data or the data will not be deposited.

Code Availability Statement. This article has no associated code or the code will not be deposited.

References

[1] ATLAS collaboration, *Measurement of the transverse momentum distribution of W bosons in pp collisions at $\sqrt{s} = 7$ TeV with the ATLAS detector*, *Phys. Rev. D* **85** (2012) 012005 [arXiv:1108.6308] [INSPIRE].

[2] ATLAS collaboration, *Measurement of the Z/γ^* boson transverse momentum distribution in pp collisions at $\sqrt{s} = 7$ TeV with the ATLAS detector*, *JHEP* **09** (2014) 145 [arXiv:1406.3660] [INSPIRE].

[3] ATLAS collaboration, *Measurement of the transverse momentum and ϕ_η^* distributions of Drell-Yan lepton pairs in proton-proton collisions at $\sqrt{s} = 8$ TeV with the ATLAS detector*, *Eur. Phys. J. C* **76** (2016) 291 [arXiv:1512.02192] [INSPIRE].

[4] ATLAS collaboration, *Measurement of the Drell-Yan triple-differential cross section in pp collisions at $\sqrt{s} = 8$ TeV*, *JHEP* **12** (2017) 059 [arXiv:1710.05167] [INSPIRE].

[5] ATLAS collaboration, *Measurement of the transverse momentum distribution of Drell-Yan lepton pairs in proton-proton collisions at $\sqrt{s} = 13$ TeV with the ATLAS detector*, *Eur. Phys. J. C* **80** (2020) 616 [arXiv:1912.02844] [INSPIRE].

[6] ATLAS collaboration, *A precise measurement of the Z-boson double-differential transverse momentum and rapidity distributions in the full phase space of the decay leptons with the ATLAS experiment at $\sqrt{s} = 8$ TeV*, *Eur. Phys. J. C* **84** (2024) 315 [arXiv:2309.09318] [INSPIRE].

---

[18]We note that the bulk of the numerical uncertainty here is due to the common NNLOjet nonsingular contribution, and thus is fully correlated between the two results. The relevant uncertainties instead are the integration uncertainties on the respective fixed-order singular components, which for the RadISH calculation in ref. [43] come out to ± 0.4 pb (and are negligible on the SCETlib side). We would like to thank Luca Rottoli and Pier Monni for their help with this comparison.

[7] CMS collaboration, *Measurement of the rapidity and transverse momentum distributions of Z bosons in pp collisions at $\sqrt{s} = 7\,TeV$*, *Phys. Rev. D* **85** (2012) 032002 [arXiv:1110.4973] [InSPIRE].

[8] CMS collaboration, *Measurement of the Z boson differential cross section in transverse momentum and rapidity in proton-proton collisions at 8 TeV*, *Phys. Lett. B* **749** (2015) 187 [arXiv:1504.03511] [InSPIRE].

[9] CMS collaboration, *Measurement of the transverse momentum spectra of weak vector bosons produced in proton-proton collisions at $\sqrt{s} = 8\,TeV$*, *JHEP* **02** (2017) 096 [arXiv:1606.05864] [InSPIRE].

[10] CMS collaboration, *Measurement of differential cross sections in the kinematic angular variable ϕ^* for inclusive Z boson production in pp collisions at $\sqrt{s} = 8\,TeV$*, *JHEP* **03** (2018) 172 [arXiv:1710.07955] [InSPIRE].

[11] CMS collaboration, *Measurements of differential Z boson production cross sections in proton-proton collisions at $\sqrt{s} = 13\,TeV$*, *JHEP* **12** (2019) 061 [arXiv:1909.04133] [InSPIRE].

[12] LHCb collaboration, *Measurement of forward W and Z boson production in pp collisions at $\sqrt{s} = 8\,TeV$*, *JHEP* **01** (2016) 155 [arXiv:1511.08039] [InSPIRE].

[13] LHCb collaboration, *Measurement of the forward Z boson production cross-section in pp collisions at $\sqrt{s} = 13\,TeV$*, *JHEP* **09** (2016) 136 [arXiv:1607.06495] [InSPIRE].

[14] J.M. Lindert et al., *Precise predictions for V+jets dark matter backgrounds*, *Eur. Phys. J. C* **77** (2017) 829 [arXiv:1705.04664] [InSPIRE].

[15] S. Camarda, G. Ferrera and M. Schott, *Determination of the strong-coupling constant from the Z-boson transverse-momentum distribution*, *Eur. Phys. J. C* **84** (2024) 39 [arXiv:2203.05394] [InSPIRE].

[16] ATLAS collaboration, *A precise determination of the strong-coupling constant from the recoil of Z bosons with the ATLAS experiment at $\sqrt{s} = 8\,TeV$*, arXiv:2309.12986 [InSPIRE].

[17] ATLAS collaboration, *Measurement of the W-boson mass in pp collisions at $\sqrt{s} = 7\,TeV$ with the ATLAS detector*, *Eur. Phys. J. C* **78** (2018) 110 [*Erratum ibid.* **78** (2018) 898] [arXiv:1701.07240] [InSPIRE].

[18] LHCb collaboration, *Measurement of the W boson mass*, *JHEP* **01** (2022) 036 [arXiv:2109.01113] [InSPIRE].

[19] CDF collaboration, *High-precision measurement of the W boson mass with the CDF II detector*, *Science* **376** (2022) 170 [InSPIRE].

[20] ATLAS collaboration, *Measurement of the W-boson mass and width with the ATLAS detector using proton-proton collisions at $\sqrt{s} = 7\,TeV$*, *Eur. Phys. J. C* **84** (2024) 1309 [arXiv:2403.15085] [InSPIRE].

[21] CMS collaboration, *High-precision measurement of the W boson mass with the CMS experiment at the LHC*, arXiv:2412.13872 [InSPIRE].

[22] M.A. Ebert, J.K.L. Michel, I.W. Stewart and F.J. Tackmann, *Drell-Yan q_T resummation of fiducial power corrections at N^3LL*, *JHEP* **04** (2021) 102 [arXiv:2006.11382] [InSPIRE].

[23] G. Billis et al., *Higgs p_T spectrum and total cross section with fiducial cuts at third resummed and fixed order in QCD*, *Phys. Rev. Lett.* **127** (2021) 072001 [arXiv:2102.08039] [InSPIRE].

[24] G.P. Salam and E. Slade, *Cuts for two-body decays at colliders*, *JHEP* **11** (2021) 220 [arXiv:2106.08329] [InSPIRE].

[25] S. Amoroso et al., *Drell-Yan cross-sections with fiducial cuts: impact of linear power corrections and q_T-resummation in PDF determination*, `arXiv:2209.13535` [INSPIRE].

[26] S. Alekhin et al., *Status of QCD precision predictions for Drell-Yan processes*, `arXiv:2405.19714` [INSPIRE].

[27] J. McGowan, T. Cridge, L.A. Harland-Lang and R.S. Thorne, *Approximate N^3LO parton distribution functions with theoretical uncertainties: MSHT20aN^{3}LO PDFs*, *Eur. Phys. J. C* **83** (2023) 185 [*Erratum ibid.* **83** (2023) 302] [`arXiv:2207.04739`] [INSPIRE].

[28] NNPDF collaboration, *The path to N^3LO parton distributions*, *Eur. Phys. J. C* **84** (2024) 659 [`arXiv:2402.18635`] [INSPIRE].

[29] T. Cridge, L.A. Harland-Lang and R.S. Thorne, *A first determination of the strong coupling α_S at approximate N^3LO order in a global PDF fit*, *Eur. Phys. J. C* **84** (2024) 1009 [`arXiv:2404.02964`] [INSPIRE].

[30] A. Cooper-Sarkar et al., *A benchmarking of QCD evolution at approximate N^3LO*, `arXiv:2406.16188` [INSPIRE].

[31] MSHT and NNPDF collaborations, *Combination of aN^{3}LO PDFs and implications for Higgs production cross-sections at the LHC*, `arXiv:2411.05373` [INSPIRE].

[32] A. Gehrmann-De Ridder et al., *Precise QCD predictions for the production of a Z boson in association with a hadronic jet*, *Phys. Rev. Lett.* **117** (2016) 022001 [`arXiv:1507.02850`] [INSPIRE].

[33] A. Gehrmann-De Ridder et al., *The NNLO QCD corrections to Z boson production at large transverse momentum*, *JHEP* **07** (2016) 133 [`arXiv:1605.04295`] [INSPIRE].

[34] R. Boughezal, C. Focke, X. Liu and F. Petriello, *W-boson production in association with a jet at next-to-next-to-leading order in perturbative QCD*, *Phys. Rev. Lett.* **115** (2015) 062002 [`arXiv:1504.02131`] [INSPIRE].

[35] R. Boughezal et al., *Z-boson production in association with a jet at next-to-next-to-leading order in perturbative QCD*, *Phys. Rev. Lett.* **116** (2016) 152001 [`arXiv:1512.01291`] [INSPIRE].

[36] R. Boughezal, X. Liu and F. Petriello, *Phenomenology of the Z-boson plus jet process at NNLO*, *Phys. Rev. D* **94** (2016) 074015 [`arXiv:1602.08140`] [INSPIRE].

[37] R. Boughezal, X. Liu and F. Petriello, *W-boson plus jet differential distributions at NNLO in QCD*, *Phys. Rev. D* **94** (2016) 113009 [`arXiv:1602.06965`] [INSPIRE].

[38] A. Gehrmann-De Ridder et al., *Next-to-next-to-leading-order QCD corrections to the transverse momentum distribution of weak gauge bosons*, *Phys. Rev. Lett.* **120** (2018) 122001 [`arXiv:1712.07543`] [INSPIRE].

[39] J.M. Campbell, R.K. Ellis and S. Seth, *H+1 jet production revisited*, *JHEP* **10** (2019) 136 [`arXiv:1906.01020`] [INSPIRE].

[40] T. Neumann and J. Campbell, *Fiducial Drell-Yan production at the LHC improved by transverse-momentum resummation at $N^4LL'+N^3LO$*, *Phys. Rev. D* **107** (2023) L011506 [`arXiv:2207.07056`] [INSPIRE].

[41] W.-L. Ju and M. Schönherr, *The q_T and $\Delta\phi$ spectra in W and Z production at the LHC at $N^3LL'+N^2LO$*, *JHEP* **10** (2021) 088 [`arXiv:2106.11260`] [INSPIRE].

[42] E. Re, L. Rottoli and P. Torrielli, *Fiducial Higgs and Drell-Yan distributions at $N^3LL'+NNLO$ with RadISH*, *JHEP* **09** (2021) 108 [`arXiv:2104.07509`] [INSPIRE].

[43] X. Chen et al., *Third-order fiducial predictions for Drell-Yan production at the LHC*, *Phys. Rev. Lett.* **128** (2022) 252001 [arXiv:2203.01565] [InSPIRE].

[44] S. Camarda, L. Cieri and G. Ferrera, *Drell-Yan lepton-pair production: q_T resummation at N^4LL accuracy*, *Phys. Lett. B* **845** (2023) 138125 [arXiv:2303.12781] [InSPIRE].

[45] V. Moos, I. Scimemi, A. Vladimirov and P. Zurita, *Extraction of unpolarized transverse momentum distributions from the fit of Drell-Yan data at N^4LL*, *JHEP* **05** (2024) 036 [arXiv:2305.07473] [InSPIRE].

[46] S. Piloneta and A. Vladimirov, *Angular distributions of Drell-Yan leptons in the TMD factorization approach*, *JHEP* **12** (2024) 059 [arXiv:2407.06277] [InSPIRE].

[47] S. Alioli et al., *Drell-Yan production at NNLL'+NNLO matched to parton showers*, *Phys. Rev. D* **92** (2015) 094020 [arXiv:1508.01475] [InSPIRE].

[48] S. Alioli et al., *Matching NNLO predictions to parton showers using N^3LL color-singlet transverse momentum resummation in Geneva*, *Phys. Rev. D* **104** (2021) 094020 [arXiv:2102.08390] [InSPIRE].

[49] S. Alioli et al., *N^3LL resummation of one-jettiness for Z-boson plus jet production at hadron colliders*, *Phys. Rev. D* **109** (2024) 094009 [arXiv:2312.06496] [InSPIRE].

[50] MAP (Multi-dimensional Analyses of Partonic distributions) collaboration, *Unpolarized transverse momentum distributions from a global fit of Drell-Yan and semi-inclusive deep-inelastic scattering data*, *JHEP* **10** (2022) 127 [arXiv:2206.07598] [InSPIRE].

[51] MAP (Multi-dimensional Analyses of Partonic distributions) collaboration, *Flavor dependence of unpolarized quark transverse momentum distributions from a global fit*, *JHEP* **08** (2024) 232 [arXiv:2405.13833] [InSPIRE].

[52] S. Dittmaier, A. Huss and C. Schwinn, *Mixed QCD-electroweak $\mathcal{O}(\alpha_s\alpha)$ corrections to Drell-Yan processes in the resonance region: pole approximation and non-factorizable corrections*, *Nucl. Phys. B* **885** (2014) 318 [arXiv:1403.3216] [InSPIRE].

[53] S. Dittmaier, A. Huss and C. Schwinn, *Dominant mixed QCD-electroweak $O(\alpha_s\alpha)$ corrections to Drell-Yan processes in the resonance region*, *Nucl. Phys. B* **904** (2016) 216 [arXiv:1511.08016] [InSPIRE].

[54] D. de Florian, M. Der and I. Fabre, *QCD⊕QED NNLO corrections to Drell Yan production*, *Phys. Rev. D* **98** (2018) 094008 [arXiv:1805.12214] [InSPIRE].

[55] M. Delto, M. Jaquier, K. Melnikov and R. Röntsch, *Mixed QCD⊗QED corrections to on-shell Z boson production at the LHC*, *JHEP* **01** (2020) 043 [arXiv:1909.08428] [InSPIRE].

[56] R. Bonciani et al., *NNLO QCD×EW corrections to Z production in the $q\bar{q}$ channel*, *Phys. Rev. D* **101** (2020) 031301 [arXiv:1911.06200] [InSPIRE].

[57] L. Cieri, D. de Florian, M. Der and J. Mazzitelli, *Mixed QCD⊗QED corrections to exclusive Drell Yan production using the q_T-subtraction method*, *JHEP* **09** (2020) 155 [arXiv:2005.01315] [InSPIRE].

[58] F. Buccioni et al., *Mixed QCD-electroweak corrections to on-shell Z production at the LHC*, *Phys. Lett. B* **811** (2020) 135969 [arXiv:2005.10221] [InSPIRE].

[59] L. Cieri, G. Ferrera and G.F.R. Sborlini, *Combining QED and QCD transverse-momentum resummation for Z boson production at hadron colliders*, *JHEP* **08** (2018) 165 [arXiv:1805.11948] [InSPIRE].

[60] A. Bacchetta and M.G. Echevarria, *QCD×QED evolution of TMDs*, *Phys. Lett. B* **788** (2019) 280 [arXiv:1810.02297] [InSPIRE].

[61] G. Billis, F.J. Tackmann and J. Talbert, *Higher-order Sudakov resummation in coupled gauge theories*, *JHEP* **03** (2020) 182 [arXiv:1907.02971] [InSPIRE].

[62] L. Buonocore, L. Rottoli and P. Torrielli, *Resummation of combined QCD-electroweak effects in Drell Yan lepton-pair production*, *JHEP* **07** (2024) 193 [arXiv:2404.15112] [InSPIRE].

[63] M.A. Ebert et al., *SCETlib: a C++ package for numerical calculations in QCD and soft-collinear effective theory*, DESY-17-099 (2018).

[64] J.C. Collins and D.E. Soper, *Angular distribution of dileptons in high-energy hadron collisions*, *Phys. Rev. D* **16** (1977) 2219 [InSPIRE].

[65] J.C. Collins and D.E. Soper, *Back-to-back jets in QCD*, *Nucl. Phys. B* **193** (1981) 381 [*Erratum ibid.* **213** (1983) 545] [InSPIRE].

[66] J.C. Collins and D.E. Soper, *Back-to-back jets: Fourier transform from B to K-transverse*, *Nucl. Phys. B* **197** (1982) 446 [InSPIRE].

[67] J.C. Collins, D.E. Soper and G.F. Sterman, *Transverse momentum distribution in Drell-Yan pair and W and Z boson production*, *Nucl. Phys. B* **250** (1985) 199 [InSPIRE].

[68] J. Collins, *Foundations of perturbative QCD*, Cambridge University Press, Cambridge, U.K. (2011) [DOI:10.1017/9781009401845] [InSPIRE].

[69] C.W. Bauer, S. Fleming and M.E. Luke, *Summing Sudakov logarithms in $B \to X_s\gamma$ in effective field theory*, *Phys. Rev. D* **63** (2000) 014006 [hep-ph/0005275] [InSPIRE].

[70] C.W. Bauer, S. Fleming, D. Pirjol and I.W. Stewart, *An effective field theory for collinear and soft gluons: heavy to light decays*, *Phys. Rev. D* **63** (2001) 114020 [hep-ph/0011336] [InSPIRE].

[71] C.W. Bauer, D. Pirjol and I.W. Stewart, *Soft collinear factorization in effective field theory*, *Phys. Rev. D* **65** (2002) 054022 [hep-ph/0109045] [InSPIRE].

[72] C.W. Bauer et al., *Hard scattering factorization from effective field theory*, *Phys. Rev. D* **66** (2002) 014017 [hep-ph/0202088] [InSPIRE].

[73] T. Becher and M. Neubert, *Drell-Yan production at small q_T, transverse parton distributions and the collinear anomaly*, *Eur. Phys. J. C* **71** (2011) 1665 [arXiv:1007.4005] [InSPIRE].

[74] M.G. Echevarria, A. Idilbi and I. Scimemi, *Factorization theorem for Drell-Yan at low q_T and transverse momentum distributions on-the-light-cone*, *JHEP* **07** (2012) 002 [arXiv:1111.4996] [InSPIRE].

[75] J.-Y. Chiu, A. Jain, D. Neill and I.Z. Rothstein, *A formalism for the systematic treatment of rapidity logarithms in quantum field theory*, *JHEP* **05** (2012) 084 [arXiv:1202.0814] [InSPIRE].

[76] Y. Li, D. Neill and H.X. Zhu, *An exponential regulator for rapidity divergences*, *Nucl. Phys. B* **960** (2020) 115193 [arXiv:1604.00392] [InSPIRE].

[77] A. Bacchetta, D. Boer, M. Diehl and P.J. Mulders, *Matches and mismatches in the descriptions of semi-inclusive processes at low and high transverse momentum*, *JHEP* **08** (2008) 023 [arXiv:0803.0227] [InSPIRE].

[78] R. von Kuk, J.K.L. Michel and Z. Sun, *Transverse momentum distributions of heavy hadrons and polarized heavy quarks*, *JHEP* **09** (2023) 205 [arXiv:2305.15461] [InSPIRE].

[79] T. Gehrmann et al., *Calculation of the quark and gluon form factors to three loops in QCD*, *JHEP* **06** (2010) 094 [arXiv:1004.3653] [InSPIRE].

[80] P.A. Baikov et al., *Quark and gluon form factors to three loops*, *Phys. Rev. Lett.* **102** (2009) 212002 [arXiv:0902.3519] [InSPIRE].

[81] D.A. Dicus and S.S.D. Willenbrock, *Radiative corrections to the ratio of Z and W boson production*, *Phys. Rev. D* **34** (1986) 148 [InSPIRE].

[82] B.A. Kniehl and J.H. Kuhn, *QCD corrections to the Z decay rate*, *Nucl. Phys. B* **329** (1990) 547 [InSPIRE].

[83] W. Bernreuther et al., *Two-loop QCD corrections to the heavy quark form-factors: anomaly contributions*, *Nucl. Phys. B* **723** (2005) 91 [hep-ph/0504190] [InSPIRE].

[84] T. Gehrmann and A. Primo, *The three-loop singlet contribution to the massless axial-vector quark form factor*, *Phys. Lett. B* **816** (2021) 136223 [arXiv:2102.12880] [InSPIRE].

[85] L. Chen, M. Czakon and M. Niggetiedt, *The complete singlet contribution to the massless quark form factor at three loops in QCD*, *JHEP* **12** (2021) 095 [arXiv:2109.01917] [InSPIRE].

[86] J.C. Collins and F.V. Tkachov, *Breakdown of dimensional regularization in the Sudakov problem*, *Phys. Lett. B* **294** (1992) 403 [hep-ph/9208209] [InSPIRE].

[87] J. Collins, *Rapidity divergences and valid definitions of parton densities*, *PoS* **LC2008** (2008) 028 [arXiv:0808.2665] [InSPIRE].

[88] J.-Y. Chiu, A. Jain, D. Neill and I.Z. Rothstein, *The rapidity renormalization group*, *Phys. Rev. Lett.* **108** (2012) 151601 [arXiv:1104.0881] [InSPIRE].

[89] J.C. Collins and D.E. Soper, *Parton distribution and decay functions*, *Nucl. Phys. B* **194** (1982) 445 [InSPIRE].

[90] S. Catani and M. Grazzini, *Higgs boson production at hadron colliders: hard-collinear coefficients at the NNLO*, *Eur. Phys. J. C* **72** (2012) 2013 [*Erratum ibid.* **72** (2012) 2132] [arXiv:1106.4652] [InSPIRE].

[91] S. Catani et al., *Vector boson production at hadron colliders: hard-collinear coefficients at the NNLO*, *Eur. Phys. J. C* **72** (2012) 2195 [arXiv:1209.0158] [InSPIRE].

[92] T. Gehrmann, T. Lübbert and L.L. Yang, *Calculation of the transverse parton distribution functions at next-to-next-to-leading order*, *JHEP* **06** (2014) 155 [arXiv:1403.6451] [InSPIRE].

[93] T. Lübbert, J. Oredsson and M. Stahlhofen, *Rapidity renormalized TMD soft and beam functions at two loops*, *JHEP* **03** (2016) 168 [arXiv:1602.01829] [InSPIRE].

[94] M.G. Echevarria, I. Scimemi and A. Vladimirov, *Universal transverse momentum dependent soft function at NNLO*, *Phys. Rev. D* **93** (2016) 054004 [arXiv:1511.05590] [InSPIRE].

[95] M.G. Echevarria, I. Scimemi and A. Vladimirov, *Unpolarized transverse momentum dependent parton distribution and fragmentation functions at next-to-next-to-leading order*, *JHEP* **09** (2016) 004 [arXiv:1604.07869] [InSPIRE].

[96] Y. Li and H.X. Zhu, *Bootstrapping rapidity anomalous dimensions for transverse-momentum resummation*, *Phys. Rev. Lett.* **118** (2017) 022004 [arXiv:1604.01404] [InSPIRE].

[97] M.-X. Luo et al., *Transverse parton distribution and fragmentation functions at NNLO: the quark case*, *JHEP* **10** (2019) 083 [arXiv:1908.03831] [InSPIRE].

[98] M.-X. Luo, T.-Z. Yang, H.X. Zhu and Y.J. Zhu, *Quark transverse parton distribution at the next-to-next-to-next-to-leading order*, *Phys. Rev. Lett.* **124** (2020) 092001 [arXiv:1912.05778] [InSPIRE].

[99] M.A. Ebert, B. Mistlberger and G. Vita, *Transverse momentum dependent PDFs at N^3LO*, *JHEP* **09** (2020) 146 [arXiv:2006.05329] [INSPIRE].

[100] T. Lübbert, J. Oredsson and M. Stahlhofen, *Rapidity renormalized TMD soft and beam functions at two loops*, *JHEP* **03** (2016) 168 [arXiv:1602.01829] [INSPIRE].

[101] S. Frixione, P. Nason and G. Ridolfi, *Problems in the resummation of soft gluon effects in the transverse momentum distributions of massive vector bosons in hadronic collisions*, *Nucl. Phys. B* **542** (1999) 311 [hep-ph/9809367] [INSPIRE].

[102] P.F. Monni, E. Re and P. Torrielli, *Higgs transverse-momentum resummation in direct space*, *Phys. Rev. Lett.* **116** (2016) 242001 [arXiv:1604.02191] [INSPIRE].

[103] M.A. Ebert and F.J. Tackmann, *Resummation of transverse momentum distributions in distribution space*, *JHEP* **02** (2017) 110 [arXiv:1611.08610] [INSPIRE].

[104] A. Bhattacharya, M.D. Schwartz and X. Zhang, *Sudakov shoulder resummation for thrust and heavy jet mass*, *Phys. Rev. D* **106** (2022) 074011 [arXiv:2205.05702] [INSPIRE].

[105] A. Bhattacharya et al., *NNLL resummation of Sudakov shoulder logarithms in the heavy jet mass distribution*, *JHEP* **11** (2023) 080 [arXiv:2306.08033] [INSPIRE].

[106] G.P. Korchemsky and A.V. Radyushkin, *Renormalization of the Wilson loops beyond the leading order*, *Nucl. Phys. B* **283** (1987) 342 [INSPIRE].

[107] S. Moch, J.A.M. Vermaseren and A. Vogt, *The three loop splitting functions in QCD: the nonsinglet case*, *Nucl. Phys. B* **688** (2004) 101 [hep-ph/0403192] [INSPIRE].

[108] A. Vogt, S. Moch and J.A.M. Vermaseren, *The three-loop splitting functions in QCD: the singlet case*, *Nucl. Phys. B* **691** (2004) 129 [hep-ph/0404111] [INSPIRE].

[109] J. Henn et al., *Four-loop photon quark form factor and cusp anomalous dimension in the large-N_c limit of QCD*, *JHEP* **03** (2017) 139 [arXiv:1612.04389] [INSPIRE].

[110] S. Moch et al., *Four-loop non-singlet splitting functions in the planar limit and beyond*, *JHEP* **10** (2017) 041 [arXiv:1707.08315] [INSPIRE].

[111] R.N. Lee, A.V. Smirnov, V.A. Smirnov and M. Steinhauser, *Four-loop quark form factor with quartic fundamental colour factor*, *JHEP* **02** (2019) 172 [arXiv:1901.02898] [INSPIRE].

[112] J.M. Henn, T. Peraro, M. Stahlhofen and P. Wasser, *Matter dependence of the four-loop cusp anomalous dimension*, *Phys. Rev. Lett.* **122** (2019) 201602 [arXiv:1901.03693] [INSPIRE].

[113] R. Brüser, A. Grozin, J.M. Henn and M. Stahlhofen, *Matter dependence of the four-loop QCD cusp anomalous dimension: from small angles to all angles*, *JHEP* **05** (2019) 186 [arXiv:1902.05076] [INSPIRE].

[114] J.M. Henn, G.P. Korchemsky and B. Mistlberger, *The full four-loop cusp anomalous dimension in $N = 4$ super Yang-Mills and QCD*, *JHEP* **04** (2020) 018 [arXiv:1911.10174] [INSPIRE].

[115] A. von Manteuffel, E. Panzer and R.M. Schabinger, *Cusp and collinear anomalous dimensions in four-loop QCD from form factors*, *Phys. Rev. Lett.* **124** (2020) 162001 [arXiv:2002.04617] [INSPIRE].

[116] O.V. Tarasov, A.A. Vladimirov and A.Y. Zharkov, *The Gell-Mann-Low function of QCD in the three loop approximation*, *Phys. Lett. B* **93** (1980) 429 [INSPIRE].

[117] S.A. Larin and J.A.M. Vermaseren, *The three loop QCD beta function and anomalous dimensions*, *Phys. Lett. B* **303** (1993) 334 [hep-ph/9302208] [INSPIRE].

[118] T. van Ritbergen, J.A.M. Vermaseren and S.A. Larin, *The four loop beta function in quantum chromodynamics*, *Phys. Lett. B* **400** (1997) 379 [`hep-ph/9701390`] [InSPIRE].

[119] M. Czakon, *The four-loop QCD beta-function and anomalous dimensions*, *Nucl. Phys. B* **710** (2005) 485 [`hep-ph/0411261`] [InSPIRE].

[120] F. Herzog et al., *The five-loop beta function of Yang-Mills theory with fermions*, *JHEP* **02** (2017) 090 [`arXiv:1701.01404`] [InSPIRE].

[121] F. Herzog et al., *Five-loop contributions to low-N non-singlet anomalous dimensions in QCD*, *Phys. Lett. B* **790** (2019) 436 [`arXiv:1812.11818`] [InSPIRE].

[122] J. Davies et al., *Large-n_f contributions to the four-loop splitting functions in QCD*, *Nucl. Phys. B* **915** (2017) 335 [`arXiv:1610.07477`] [InSPIRE].

[123] S. Moch et al., *On quartic colour factors in splitting functions and the gluon cusp anomalous dimension*, *Phys. Lett. B* **782** (2018) 627 [`arXiv:1805.09638`] [InSPIRE].

[124] G. Das, S.-O. Moch and A. Vogt, *Soft corrections to inclusive deep-inelastic scattering at four loops and beyond*, *JHEP* **03** (2020) 116 [`arXiv:1912.12920`] [InSPIRE].

[125] G. Das, S. Moch and A. Vogt, *Approximate four-loop QCD corrections to the Higgs-boson production cross section*, *Phys. Lett. B* **807** (2020) 135546 [`arXiv:2004.00563`] [InSPIRE].

[126] B. Agarwal, A. von Manteuffel, E. Panzer and R.M. Schabinger, *Four-loop collinear anomalous dimensions in QCD and N=4 super Yang-Mills*, *Phys. Lett. B* **820** (2021) 136503 [`arXiv:2102.09725`] [InSPIRE].

[127] G. Billis, M.A. Ebert, J.K.L. Michel and F.J. Tackmann, *A toolbox for q_T and 0-jettiness subtractions at N^3LO*, *Eur. Phys. J. Plus* **136** (2021) 214 [`arXiv:1909.00811`] [InSPIRE].

[128] R. Brüser, Z.L. Liu and M. Stahlhofen, *Three-loop quark jet function*, *Phys. Rev. Lett.* **121** (2018) 072003 [`arXiv:1804.09722`] [InSPIRE].

[129] M.A. Ebert, B. Mistlberger and G. Vita, *N-jettiness beam functions at N^3LO*, *JHEP* **09** (2020) 143 [`arXiv:2006.03056`] [InSPIRE].

[130] A.A. Vladimirov, *Correspondence between soft and rapidity anomalous dimensions*, *Phys. Rev. Lett.* **118** (2017) 062001 [`arXiv:1610.05791`] [InSPIRE].

[131] C. Duhr, B. Mistlberger and G. Vita, *Four-loop rapidity anomalous dimension and event shapes to fourth logarithmic order*, *Phys. Rev. Lett.* **129** (2022) 162001 [`arXiv:2205.02242`] [InSPIRE].

[132] I. Moult, H.X. Zhu and Y.J. Zhu, *The four loop QCD rapidity anomalous dimension*, *JHEP* **08** (2022) 280 [`arXiv:2205.02249`] [InSPIRE].

[133] C. Duhr, B. Mistlberger and G. Vita, *Soft integrals and soft anomalous dimensions at N^3LO and beyond*, *JHEP* **09** (2022) 155 [`arXiv:2205.04493`] [InSPIRE].

[134] M.A. Ebert, J.K.L. Michel and F.J. Tackmann, *Resummation improved rapidity spectrum for gluon fusion Higgs production*, *JHEP* **05** (2017) 088 [`arXiv:1702.00794`] [InSPIRE].

[135] M.-X. Luo, T.-Z. Yang, H.X. Zhu and Y.J. Zhu, *Unpolarized quark and gluon TMD PDFs and FFs at N^3LO*, *JHEP* **06** (2021) 115 [`arXiv:2012.03256`] [InSPIRE].

[136] R.N. Lee, A.V. Smirnov and V.A. Smirnov, *Analytic results for massless three-loop form factors*, *JHEP* **04** (2010) 020 [`arXiv:1001.2887`] [InSPIRE].

[137] V. Bertone, G. Bozzi and F. Hautmann, *Perturbative hysteresis and emergent resummation scales*, *Phys. Rev. D* **105** (2022) 096003 [`arXiv:2202.03380`] [InSPIRE].

[138] V. Bertone, G. Bozzi and F. Hautmann, *Perturbative RGE systematics in precision observables*, arXiv:2407.20842 [INSPIRE].

[139] M.A. Ebert, *Analytic results for Sudakov form factors in QCD*, *JHEP* **02** (2022) 136 [arXiv:2110.11360] [INSPIRE].

[140] S. Catani and M. Grazzini, *An NNLO subtraction formalism in hadron collisions and its application to Higgs boson production at the LHC*, *Phys. Rev. Lett.* **98** (2007) 222002 [hep-ph/0703012] [INSPIRE].

[141] J. Gaunt, M. Stahlhofen, F.J. Tackmann and J.R. Walsh, *N-jettiness subtractions for NNLO QCD calculations*, *JHEP* **09** (2015) 058 [arXiv:1505.04794] [INSPIRE].

[142] J. Cleymans and M. Kuroda, *Angular distribution of dileptons in hadronic collisions*, *Nucl. Phys. B* **155** (1979) 480 [*Erratum ibid.* **160** (1979) 510] [INSPIRE].

[143] M. Chaichian, M. Hayashi and K. Yamagishi, *Angular distributions of high mass dileptons with finite transverse momentum in high-energy hadronic collisions*, *Phys. Rev. D* **25** (1982) 130 [*Erratum ibid.* **26** (1982) 2534] [INSPIRE].

[144] E. Mirkes, *Angular decay distribution of leptons from W bosons at NLO in hadronic collisions*, *Nucl. Phys. B* **387** (1992) 3 [INSPIRE].

[145] J.M. Campbell, R.K. Ellis and W.T. Giele, *A multi-threaded version of MCFM*, *Eur. Phys. J. C* **75** (2015) 246 [arXiv:1503.06182] [INSPIRE].

[146] R. Boughezal et al., *Color singlet production at NNLO in MCFM*, *Eur. Phys. J. C* **77** (2017) 7 [arXiv:1605.08011] [INSPIRE].

[147] S. Bailey et al., *Parton distributions from LHC, HERA, Tevatron and fixed target data: MSHT20 PDFs*, *Eur. Phys. J. C* **81** (2021) 341 [arXiv:2012.04684] [INSPIRE].

[148] NNPDF collaboration, *The path to proton structure at 1% accuracy*, *Eur. Phys. J. C* **82** (2022) 428 [arXiv:2109.02653] [INSPIRE].

[149] I. Moult et al., *Subleading power corrections for N-jettiness subtractions*, *Phys. Rev. D* **95** (2017) 074023 [arXiv:1612.00450] [INSPIRE].

[150] I. Moult et al., *N-jettiness subtractions for $gg \to H$ at subleading power*, *Phys. Rev. D* **97** (2018) 014013 [arXiv:1710.03227] [INSPIRE].

[151] W. Bizon et al., *The transverse momentum spectrum of weak gauge bosons at $N^3LL+NNLO$*, *Eur. Phys. J. C* **79** (2019) 868 [arXiv:1905.05171] [INSPIRE].

[152] M.A. Ebert, J.K.L. Michel, I.W. Stewart and Z. Sun, *Disentangling long and short distances in momentum-space TMDs*, *JHEP* **07** (2022) 129 [arXiv:2201.07237] [INSPIRE].

[153] G. Lustermans, J.K.L. Michel, F.J. Tackmann and W.J. Waalewijn, *Joint two-dimensional resummation in q_T and 0-jettiness at NNLL*, *JHEP* **03** (2019) 124 [arXiv:1901.03331] [INSPIRE].

[154] D. Bertolini, M.P. Solon and J.R. Walsh, *Integrated and differential accuracy in resummed cross sections*, *Phys. Rev. D* **95** (2017) 054024 [arXiv:1701.07919] [INSPIRE].

[155] A. Bacchetta et al., *Extraction of partonic transverse momentum distributions from semi-inclusive deep-inelastic scattering, Drell-Yan and Z-boson production*, *JHEP* **06** (2017) 081 [*Erratum ibid.* **06** (2019) 051] [arXiv:1703.10157] [INSPIRE].

[156] NNPDF collaboration, *Parton distributions from high-precision collider data*, *Eur. Phys. J. C* **77** (2017) 663 [arXiv:1706.00428] [INSPIRE].

[157] T.-J. Hou et al., *New CTEQ global analysis of quantum chromodynamics with high-precision data from the LHC*, *Phys. Rev. D* **103** (2021) 014013 [`arXiv:1912.10053`] [InSPIRE].

[158] R. Boussarie et al., *TMD handbook*, `arXiv:2304.03302` [InSPIRE].

[159] I. Scimemi and A. Vladimirov, *Systematic analysis of double-scale evolution*, *JHEP* **08** (2018) 003 [`arXiv:1803.11089`] [InSPIRE].

[160] A.A. Vladimirov, *Self-contained definition of the Collins-Soper kernel*, *Phys. Rev. Lett.* **125** (2020) 192002 [`arXiv:2003.02288`] [InSPIRE].

[161] I. Scimemi and A. Vladimirov, *Power corrections and renormalons in transverse momentum distributions*, *JHEP* **03** (2017) 002 [`arXiv:1609.06047`] [InSPIRE].

[162] J. Collins and T. Rogers, *Understanding the large-distance behavior of transverse-momentum-dependent parton densities and the Collins-Soper evolution kernel*, *Phys. Rev. D* **91** (2015) 074020 [`arXiv:1412.3820`] [InSPIRE].

[163] M. Schlemmer et al., *Determination of the Collins-Soper kernel from lattice QCD*, *JHEP* **08** (2021) 004 [`arXiv:2103.16991`] [InSPIRE].

[164] Lattice Parton (LPC) collaboration, *Nonperturbative determination of the Collins-Soper kernel from quasitransverse-momentum-dependent wave functions*, *Phys. Rev. D* **106** (2022) 034509 [`arXiv:2204.00200`] [InSPIRE].

[165] H.-T. Shu et al., *Universality of the Collins-Soper kernel in lattice calculations*, *Phys. Rev. D* **108** (2023) 074519 [`arXiv:2302.06502`] [InSPIRE].

[166] Lattice Parton (LPC) collaboration, *Lattice calculation of the intrinsic soft function and the Collins-Soper kernel*, *JHEP* **08** (2023) 172 [`arXiv:2306.06488`] [InSPIRE].

[167] A. Avkhadiev, P.E. Shanahan, M.L. Wagman and Y. Zhao, *Determination of the Collins-Soper kernel from lattice QCD*, *Phys. Rev. Lett.* **132** (2024) 231901 [`arXiv:2402.06725`] [InSPIRE].

[168] M. Bury et al., *PDF bias and flavor dependence in TMD distributions*, *JHEP* **10** (2022) 118 [`arXiv:2201.07114`] [InSPIRE].

[169] I. Scimemi and A. Vladimirov, *Matching of transverse momentum dependent distributions at twist-3*, *Eur. Phys. J. C* **78** (2018) 802 [`arXiv:1804.08148`] [InSPIRE].

[170] D. Boer, *Investigating the origins of transverse spin asymmetries at RHIC*, *Phys. Rev. D* **60** (1999) 014012 [`hep-ph/9902255`] [InSPIRE].

[171] A. Gao, J.K.L. Michel and I.W. Stewart, *TMD factorization for Drell-Yan production and e^+e^- collisions at next-to-leading power*, to appear (2024).

[172] A. Gao, J.K.L. Michel, I.W. Stewart and Z. Sun, *Better angle on hadron transverse momentum distributions at the electron-ion collider*, *Phys. Rev. D* **107** (2023) L091504 [`arXiv:2209.11211`] [InSPIRE].

[173] F.J. Tackmann, *Theory uncertainties and correlations from theory nuisance parameters*, in *SCET 2024: XXIst annual workshop on Soft-Collinear Effective Theory*, 2024-02-26_TNPs_FT (2024).

[174] F.J. Tackmann, *Beyond scale variations: perturbative theory uncertainties from nuisance parameters*, `arXiv:2411.18606` [InSPIRE].

[175] I.W. Stewart, F.J. Tackmann, J.R. Walsh and S. Zuberi, *Jet p_T resummation in Higgs production at NNLL'+NNLO*, *Phys. Rev. D* **89** (2014) 054001 [`arXiv:1307.1808`] [InSPIRE].

[176] P. Cal, R. von Kuk, M.A. Lim and F.J. Tackmann, q_T spectrum for Higgs boson production via heavy quark annihilation at $N^3LL'+aN^3LO$, *Phys. Rev. D* **110** (2024) 076005 [arXiv:2306.16458] [INSPIRE].

[177] C.S. Lam and W.-K. Tung, *A systematic approach to inclusive lepton pair production in hadronic collisions*, *Phys. Rev. D* **18** (1978) 2447 [INSPIRE].

[178] P. Shanahan, M. Wagman and Y. Zhao, *Lattice QCD calculation of the Collins-Soper kernel from quasi-TMDPDFs*, *Phys. Rev. D* **104** (2021) 114502 [arXiv:2107.11930] [INSPIRE].

[179] P. Pietrulewicz, D. Samitz, A. Spiering and F.J. Tackmann, *Factorization and resummation for massive quark effects in exclusive Drell-Yan*, *JHEP* **08** (2017) 114 [arXiv:1703.09702] [INSPIRE].

[180] J. Butterworth et al., *PDF4LHC recommendations for LHC run II*, *J. Phys. G* **43** (2016) 023001 [arXiv:1510.03865] [INSPIRE].

[181] PARTICLE DATA GROUP collaboration, *Review of particle physics*, *Phys. Rev. D* **110** (2024) 030001 [INSPIRE].

[182] R. Abbate et al., *Thrust at N^3LL with power corrections and a precision global fit for $\alpha_s(mZ)$*, *Phys. Rev. D* **83** (2011) 074021 [arXiv:1006.3080] [INSPIRE].

[183] R. Abbate et al., *Precision thrust cumulant moments at N^3LL*, *Phys. Rev. D* **86** (2012) 094002 [arXiv:1204.5746] [INSPIRE].

[184] G. Falcioni, F. Herzog, S. Moch and A. Vogt, *Four-loop splitting functions in QCD — the quark-quark case*, *Phys. Lett. B* **842** (2023) 137944 [arXiv:2302.07593] [INSPIRE].

[185] G. Falcioni et al., *The double fermionic contribution to the four-loop quark-to-gluon splitting function*, *Phys. Lett. B* **848** (2024) 138351 [arXiv:2310.01245] [INSPIRE].

[186] S. Moch et al., *Additional moments and x-space approximations of four-loop splitting functions in QCD*, *Phys. Lett. B* **849** (2024) 138468 [arXiv:2310.05744] [INSPIRE].

[187] G. Falcioni et al., *Four-loop splitting functions in QCD — the quark-to-gluon case*, *Phys. Lett. B* **856** (2024) 138906 [arXiv:2404.09701] [INSPIRE].

[188] G. Falcioni et al., *Four-loop splitting functions in QCD — the gluon-gluon case*, *Phys. Lett. B* **860** (2025) 139194 [arXiv:2410.08089] [INSPIRE].

[189] R. Boughezal, A. Guffanti, F. Petriello and M. Ubiali, *The impact of the LHC Z-boson transverse momentum data on PDF determinations*, *JHEP* **07** (2017) 130 [arXiv:1705.00343] [INSPIRE].

[190] C. Duhr, F. Dulat and B. Mistlberger, *Drell-Yan cross section to third order in the strong coupling constant*, *Phys. Rev. Lett.* **125** (2020) 172001 [arXiv:2001.07717] [INSPIRE].